T-3933

Weldability and Hot Ductility of Iron Aluminides

By: Daniel I. Ash

T-3933

A thesis submitted to the Faculty and the Board of Trustees of the Colorado School of Mines in partial fulfillment of the requirements for the degree of Master of Science (Metallurgical Engineering).

Golden, Colorado
Date 4/5/91

Signed: Daniel I. Ash
Daniel I. Ash

Approved: Glen Edwards
Glen R. Edwards
Thesis Advisor

Golden, Colorado
Date 4/17/91

John J. Moore
Professor and Head,
Metallurgical and
Materials Engineering
Department

ABSTRACT

The weldability of iron aluminide alloys is discussed. Although readily welded with electron beam (EB) and gas-tungsten arc (GTA) techniques, iron aluminides are sometimes susceptible to cracking during cooling when welded with the GTA welding process. Taken into account are the effects of microstructural instability (grain growth), weld heat input (cooling rate) and environment on the hot ductility of an iron aluminide alloy designated FA-129.

TABLE OF CONTENTS

LIST OF FIGURES

Page

Page

Page

Page

Page

LIST OF TABLES

ACKNOWLEDGEMENTS

The author would like to thank the United States Department of Energy Fossil Energy Materials Program for funding this investigation. I am also thankful for the sponsorship of the Center for Welding and Joining Research at the Colorado School of Mines. I would like to thank my advisor, Dr. Glen R. Edwards for his help and useful discussions regarding the direction of this research project, and my co-advisor, Dr. Stan A. David of Oak Ridge National Laboratory, for his guidance while I was at ORNL in 1989. I would also like to thank my committee members, Dr. William D. Copeland and Dr. David L. Olson for their helpful advice.

At the Colorado School of Mines, the author would like to thank the following people in the Metallurgical and Materials Engineering Department: Dr. David K. Matlock, for taking time to listen, and the valuable discussions regarding my work and my future, and Mike Baldwin for his help with the administrative details of this project. Additionally, the author would like to thank Dr. John P. Hager for his interest and encouragement over the past years.

At ORNL, I would like to thank Dr. Mike Santella for

his help and knowledge, and for showing me there are things to do in Oak Ridge, Tennessee besides working at The Lab. I would also like to thank Dr. Claudette McKamey, whose valuable knowledge and experience with iron aluminide development was instrumental in developing an understanding of this unique alloy system.

At Sandia National Laboratory, I would like to thank Dr. Mike Maguire for his knowledge and help regarding how to approach researching aluminide weldability.

I would like to thank my family for their encouragement and support during my education. Also, I appreciate the support of my friends, especially Stan Dierking, for his philosophical approach to life and many fond discussions at The City Spirit Cafe.

I would especially like to thank my fiancee, Dianna, for her encouragement, support, and understanding for the past three years.

Finally, a historical note. The majority of this thesis was written during the Persian Gulf War (January 16 - February 27, 1991). It is not often one accomplishes a major goal in his life while others are risking their lives for the sake of freedom. This thesis is dedicated to the people who lost their lives fighting for this belief.

1. INTRODUCTION

Initially, interest in developing ordered alloys for high temperature structural applications began with γ' nickel aluminide (Ni_3Al), the main strengthening precipitate in nickel-base superalloys. Properties such as positive strength dependence with temperature and excellent creep resistance have made it attractive for these applications. However, poor hot ductility and limited weldability of Ni_3Al and other ordered alloys have hindered their development.

With the success of improved nickel aluminide weldability (1), an Fe_3Al-based iron aluminide alloy was studied to understand the factors controlling the weldability and hot ductility of the material. Alloys centered around the Fe_3Al composition form ordered structures based on either the simple cubic or face-centered cubic lattices, depending on temperature. These alloys have a positive dependence of strength with temperature (2) which is not as extensive as Ni_3Al. However, the ductility of iron aluminides behaves much differently than that of Ni_3Al. That is, there is no ductility minimum corresponding to the peak strength at an intermediate temperature, Fig. 1.1. This behavior is in contrast to Ni_3Al. Ni_3Al alloys are susceptible to sub-solidus weld cracking in this low

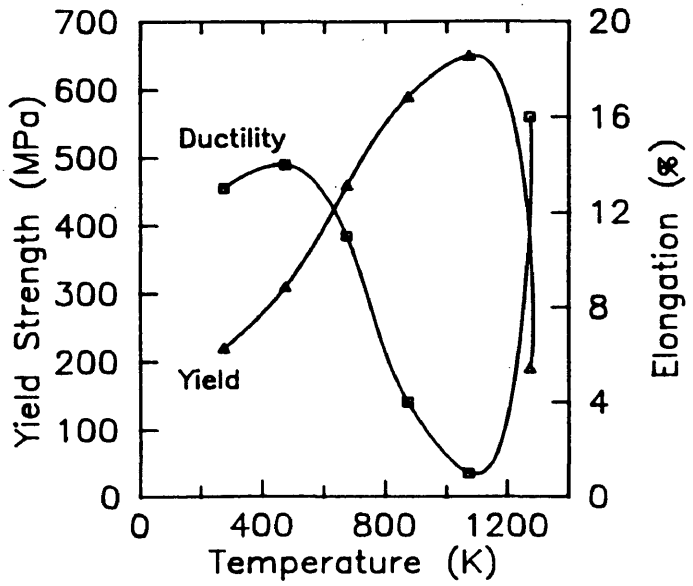

(a)

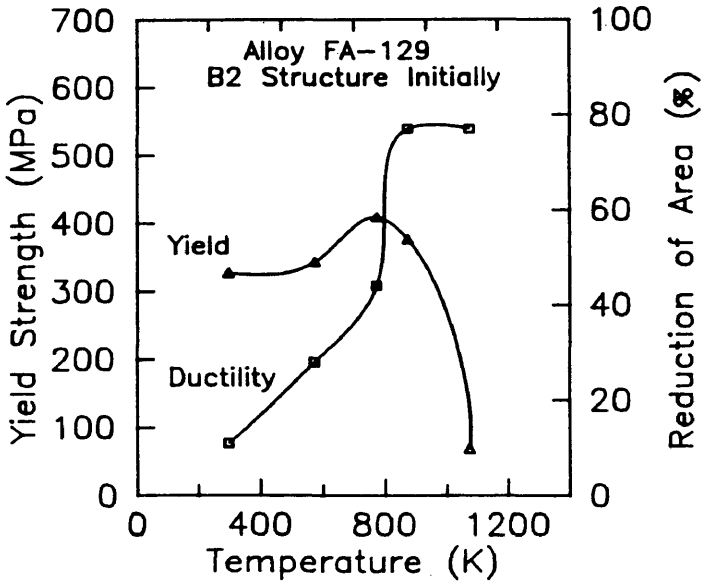

(b)

Figure 1.1 Deformation behavior of (a) nickel aluminide alloy, and (b) iron aluminide alloy.

ductility temperature regime. Even though iron aluminides are readily weldable using the electron beam process, they tend to suffer cracking under low heat input conditions (high welding speed and cooling rate) during gas-tungsten arc (GTA) welding (3). Some microcracking has also been observed for high heat input GTA welds on advanced alloys (4). Thus, the focus of this thesis is to reveal the factors controlling the high temperature deformation of iron aluminides in relation to weldability.

1.1 Relevance of Iron-Aluminum Alloys

Interest in developing iron-aluminum alloys began in the earlier part of this century, with emphasis on the excellent high temperature oxidation and sulfidation resistance, and high electrical resistance offered by these alloys (5). Thus, applications in corrosive environments and furnace windings were the focus of interest. These materials, ranging from 0-16 wt. pct aluminum (0-28.3 at. pct), were readily hot forged from ingots at high temperatures (1250°C). However, applications in the ambient temperature to 400°C range were limited by the low ductility and brittle fracture of alloys containing more than 5 wt. pct (9.8 at. pct) aluminum. It was thought that oxide inclusions resulting from air melting were the main cause of

this brittleness. Other detrimental properties were low thermal conductivity and high thermal expansivity, leading to low thermal shock resistance and subsequent cracking upon rapid cooling or heating. Also, no consideration of short range ordering or long range ordered structures was taken into account as a possible factor affecting the material properties in the iron-aluminum alloy system.

Interest in developing these materials resurfaced in the 1950's with the work of Morgan and Zackay (6), Justusson et al (7), and Kayser (8). The main concern was to improve room temperature ductility through alloying and processing.

Morgan and Zackay (6), looking to use iron-aluminum alloys as low-cost substitutes for heat resistant alloys such as stainless steels, improved ambient temperature ductilities through vacuum melting while improving high temperature properties with minor alloying additions. They developed binary alloys with better oxidation resistance than 316 stainless steel, and ternary alloys with creep resistance superior to 302 stainless steel. Yet, room temperature ductility remained low for alloys containing 10 wt. pct. Al (19 at. pct) and above. This low ambient temperature brittleness, along with ingot microcracking, continued to hamper the development of iron-aluminum alloys.

Justusson et al (7) compared room temperature

properties of alloys containing 8-16 wt. pct (15.2-28.3 at. pct) aluminum. They noticed a peak in both ambient temperature yield and ultimate strengths at approximately 14 wt. pct (25.2 at. pct) aluminum, which is near the stoichiometric composition of Fe_3Al. These strengths, however, decreased above this composition. Also, the ductile to brittle transition temperature increased with increasing amounts of carbon, which was added to deoxidize the melt before casting.

Kayser (8) reported an increase of both yield and ultimate strengths with temperature. The maximum occurred at approximately 552°C for alloys with 13.8-17.6 wt. pct (25-30.6 at. pct) aluminum. In addition, fracture appearances of the broad range of alloys were noted. For the 13.8-17.6 wt. pct alloys, ductile fracture was seen above 1000°F (538°C) with transgranular (cleavage) fracture below 1000°F. Also, ductility increased dramatically above this temperature. With the available data for the broad range of alloys studied, Kayser concluded that the maximum application temperature for iron-aluminum alloys with up to 16 wt pct aluminum (28.3 at. pct) was 1000°F (538°C) because of poor hot strength above this temperature.

1.2 Welding of Iron-Aluminum Alloys

Although weldability data for iron-aluminum alloys are not common, Sykes and Bampfylde (5) welded a 14 wt. pct. (25.2 at. pct) aluminum alloy sheet with a rod of the same composition after it had been fractured at room temperature. However, no welding process was described.

It was not until the late 1950s that the weldability of iron-aluminum alloys was again addressed for heat treatment and gas turbine engine applications (9). However, alloys with only 5.45 to 10.66 wt. pct Al (11-20 at. pct) were investigated. These studies revealed the low (11 at. pct) aluminum alloy to be readily weldable with wire of the same composition and the GTA process. This was also accomplished without a pre- or post-weld thermal treatment. However, weld cracking occurred for binary alloys with higher aluminum contents (20 at. pct) when welded in a similar fashion and cooled below 52°C (125°F) with either oil quenching or air cooling. Only when a preheat at 66°C (150°F) plus an immediate post-weld heat treatment at 649°C (1200°F) were performed could the weld cracking be alleviated.

Recent research on iron aluminide weldability has shown sensitivity to alloying and welding process. Preliminary tests on binary alloys containing 1.0 wt. pct. TiB_2 for

grain refinement (10) showed that increasing aluminum content from 24 at. pct. to 27 at. pct improved electron beam weldability. Later studies (3) showed that ternary additions of either chromium or niobium were also beneficial to both EB and GTA weld cracking resistance. These improvements were attributed to the beneficial effect of these elements on the ductility of these materials. However, binary alloys and most ternary alloys containing TiB_2, and welded by the GTA process, showed liquation or hot cracking in the fusion zone. This was attributed to the dissolution of TiB_2 in the fusion zone, and re-precipitation at dendrite boundaries. Furthermore, advanced alloys (4) which did not contain TiB_2 showed excellent EB and GTA weldability; however, microcracking occurred in both the HAZ and FZ upon cooling of GTA welds, even at low welding speeds (high heat inputs). This indicated either sub-solidus or cold cracking of the welds. Also, it was evident that excessive grain growth occurred in the heat-affected zone, which possibly compounded the cracking problem.

1.3 Phase Equilibria in the Iron-Aluminum System

The iron-aluminum phase diagram is shown in Figure 1.2 (a) (11). As can be seen from the iron-rich section of the diagram at low temperatures, a solid solution of iron and

aluminum, α, is stable to about 24 at. pct. At this point, the ordered DO_3 structure of Fe_3Al begins. This phase is present from 24 at. pct. to 36 at. pct aluminum, indicating a compositional range of stability. From 36 at. pct to 50 at. pct, the B2 structure of FeAl exists. A closer view of the ordered phases in the iron-rich portion of the phase diagram can be seen in Fig. 1.2 (b) (10). What is important to note is that alloys based on Fe_3Al can possess the B2 (FeAl) structure above 550°C. It should be stated that this B2 structure is not fully ordered for these Fe_3Al-based alloys.

1.3.1 Ordered Structures in the Iron-Aluminum System

As can be seen from the phase diagrams, some ordered structures can have a range of composition, unlike a true intermetallic compound which would appear as a vertical line at some specific composition. For the case of the iron-aluminum system, two ordered structures can form towards the iron-rich side of the phase diagram. These unique features of the iron-aluminum alloy system were first studied by Bradley and Jay (12). Using the Struckterbricht notation, these two structures are: (1) the B2 or CsCl structure, and (2) the DO_3 or BiF_3 structure.

The B2 superlattice consists of a simple cubic lattice,

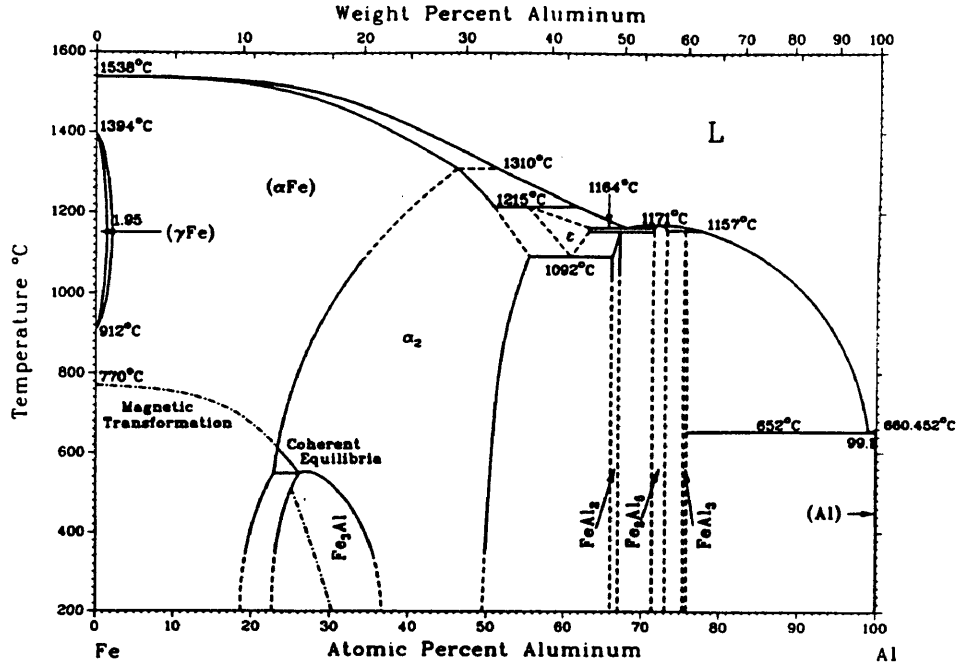

(a)

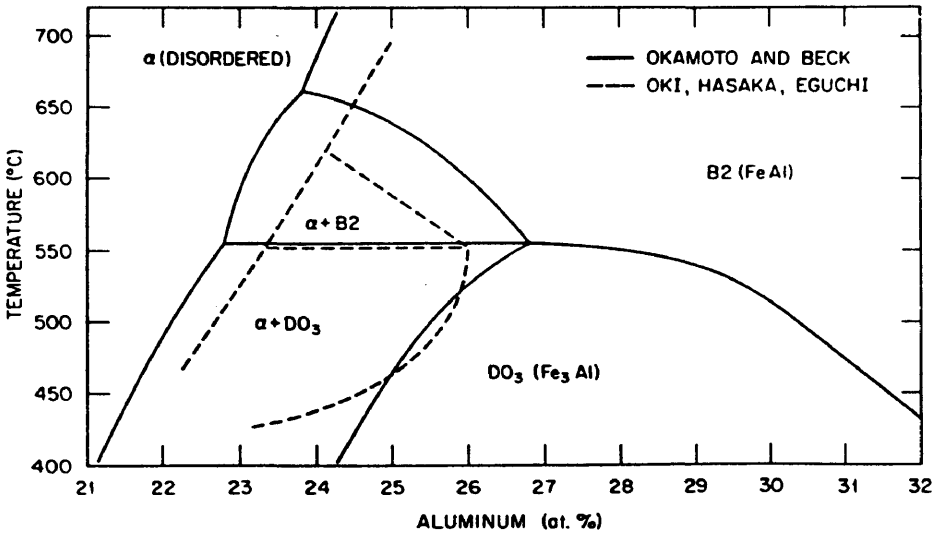

(b)

Figure 1.2 Iron-aluminum phase diagram (11) in (a), and closer view of ordered phase relationships in the iron-rich portion of the phase diagram (12) in (b).

with two atoms per lattice point, giving an AB stoichiometry with lattice parameter a_o, Figure 1.3 (a). The DO_3 superlattice, however, is face-centered cubic, with four atoms per lattice point. This gives an A_3B stoichiometry, with lattice parameter $a_o' = 2a_o$, Figure 1.3 (b).

1.3.2 Phase Transformations in the Iron-Aluminum System

Referring to Figures 1.2 (a) and (b), and taking a stoichiometric Fe_3Al alloy (25 at. pct Al) cooling from the freezing temperature, the material will solidify as disordered α. Continued cooling to 760°C results in the transformation to a partially ordered B2 structure, where iron atoms occupy the corner sites, with the remaining iron and aluminum atoms occupying the body centering sites at random. Cooling past 650°C leads to a coherent, two-phase equilibria between B2 and α (triangular region in Fig. 1.2 (a)). This basically results in a microstructure consisting of ordered B2 precipitates in a disordered (α) matrix. Below 550°C, the B2 precipitates transform into the DO_3 structure within the disordered matrix. Cooling below 500°C gives single phase DO_3-ordered Fe_3Al. Considering these transformations are based on the equilibrium diagrams, a wider variety of microstructures and transformation sequences can be developed when the material is in a

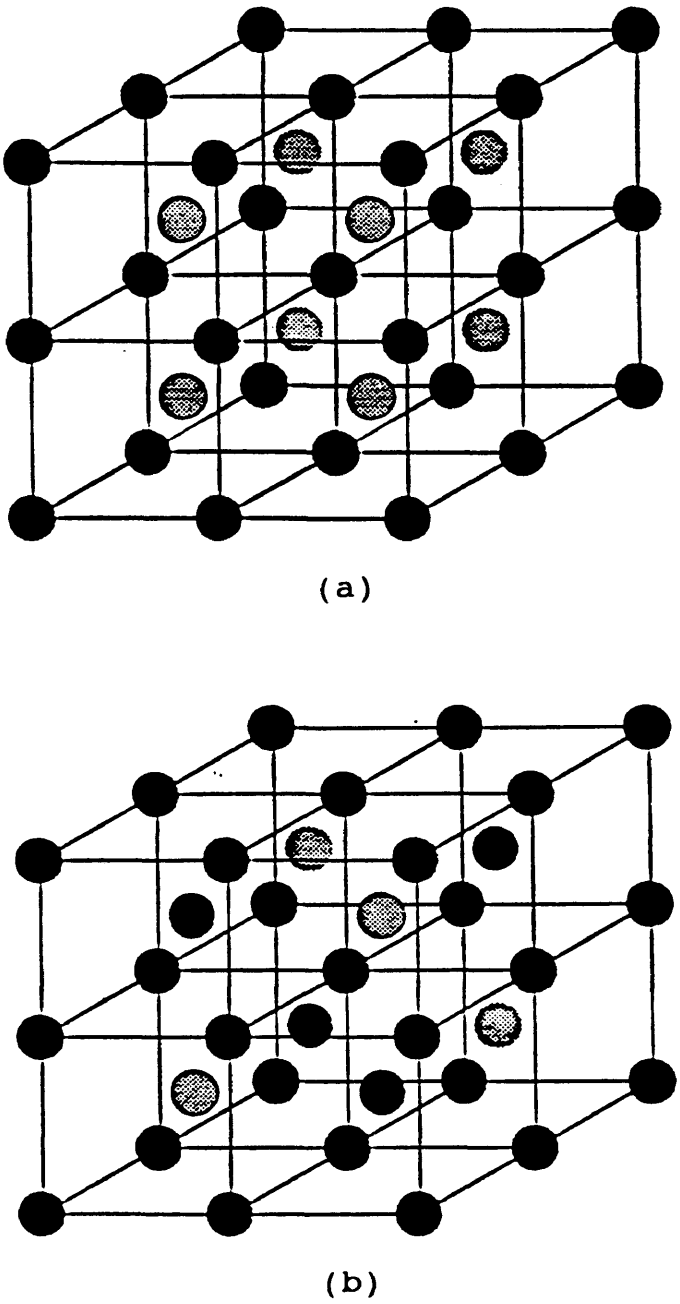

Figure 1.3 B2 superlattice structure in (a), and DO_3 superlattice structure in (b) for Fe_3Al-based alloys.

metastable state (13). This variety can develop through nucleation and growth or spinodal decomposition. However, since the author's base alloy is centered around Fe-28 at. pct Al, these transformation sequences will not be of significance.

For hyperstoichiometric compositions (ie. 27-36 at. pct Al), the phase transformation sequence is greatly simplified. Upon cooling from the freezing temperature, the only transformations occurring are: $\alpha \rightarrow$ B2 and B2 $\rightarrow DO_3$. These transformations are reported to be second-, or higher-order transformations, also known as continuous transformations. The word order used in this sense refers to the nature of the transformation in terms of the change in free energy with temperature. Second order transformations can be identified by a discontinuity in the second derivative of free energy with respect to temperature (hence "second order") as opposed to first order transformations, which show discontinuities in the first derivative of free energy with respect to temperature, Figure 1.4. Also, second order (continuous) transformations are ones which can not be suppressed during cooling, whereas first order transformations can. Thus, it is expected that upon cooling from high temperatures, the DO_3 ordered structure is expected to exist at room temperature.

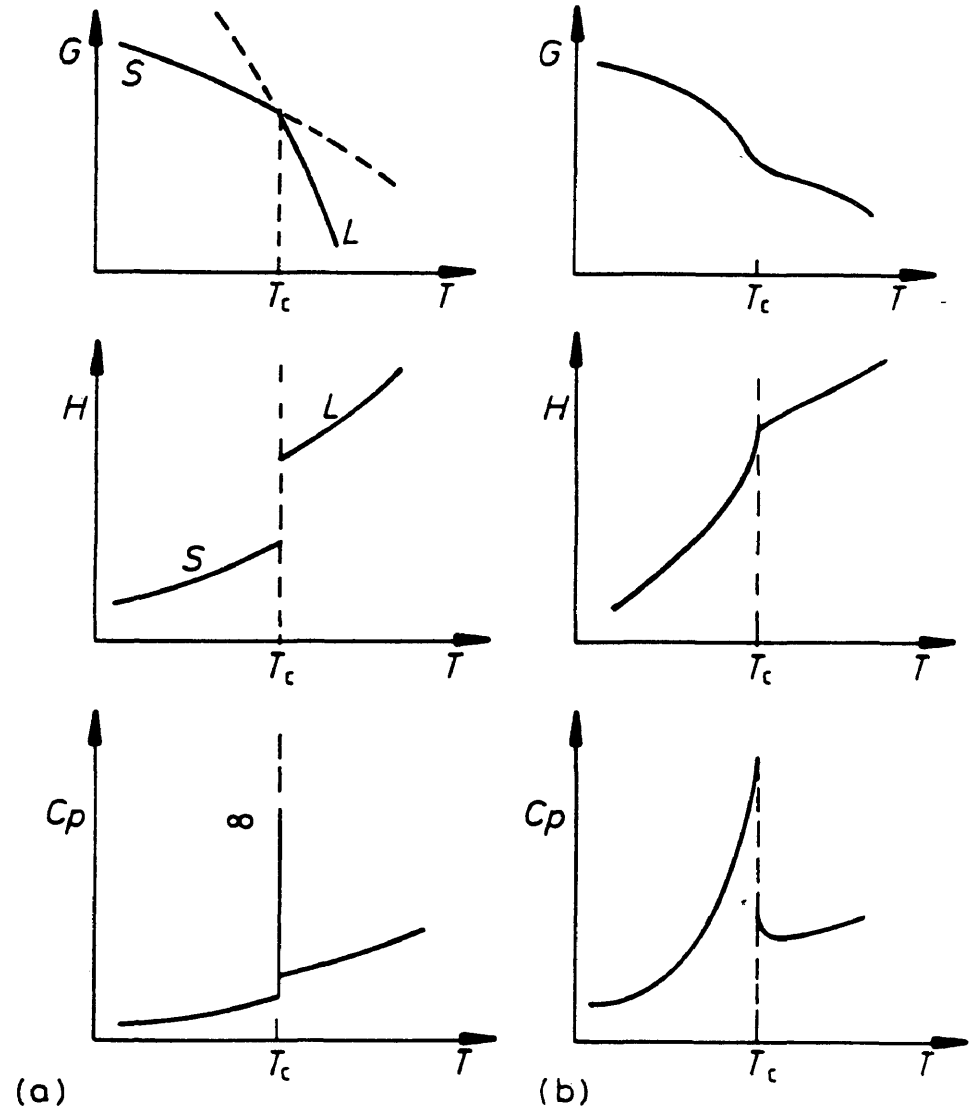

Figure 1.4 Thermodynamic determination of (a) first order, and (b) second order transformations.

The addition of chromium as a ternary alloying element appears to cause no drastic changes in the phase equilibria, as seen in a pseudobinary section of the Fe-Al-Cr ternary in Fig. 1.5 (14). The only significant changes are that both the $\alpha \rightarrow$ B2 and B2 $\rightarrow DO_3$ transition temperatures are decreased by approximately 5-10°C. This indicates a decrease in the ordering energies between unlike atoms.

1.4 Deformation Mechanisms in Fe_3Al

Because Fe_3Al-based alloys can possess either the B2 or DO_3 ordered structures, they show deformation behavior which is characteristic of most other ordered alloys. That is, a peak in flow stress occurs at some intermediate temperature as a result of either the unique restrictions on dislocations in long range ordered superlattices, or a change in slip system at higher temperatures (15). For the case of Fe_3Al, it will be shown that: (1) the $\{110\}\langle 111\rangle$ slip system dominates in both superlattices, and (2) the deformation behavior is dominated mainly by the motion of superlattice dislocations, consisting of dislocation pairs (B2 structure) or four-fold dislocations (DO_3 structure). Also, theories to explain deformation behavior in these ordered alloys will be presented.

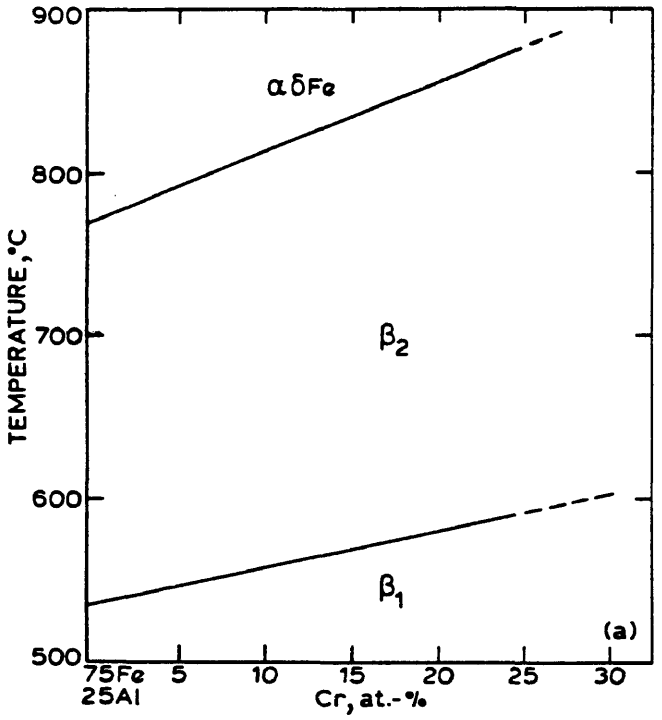

Figure 1.5 Pseudobinary section centering on ordered phases. After (14).

1.4.1 Dislocations in the DO_3 Superlattice

In the fully ordered DO_3 structure for stoichiometric Fe_3Al, the existence of four-fold superlattice dislocations was first theorized by Marcinkowski and Brown (16). The superlattice dislocation consists of four $a_o'/4\langle 111\rangle$-type dislocations, which are necessary to make a perfect lattice translation in the DO_3 structure. Between each individual dislocation is an antiphase boundary (APB), which indicates disordering of atomic bonds by the passage of each individual dislocation. The leading dislocation creates nearest neighbor antiphase boundary (NNAPB) as it passes along the slip plane. The second dislocation reorders the nearest neighbors, yet disorders the next-nearest neighbors, creating next-nearest neighbor APB (NNNAPB). Likewise, the third dislocation reorders the next-nearest neighbors, while disordering the nearest neighbors, creating another NNAPB. Finally, the fourth dislocation reorders the nearest neighbors, creating a perfect lattice in its wake. Thus, the four-fold dislocation will consist of NNAPB coupling dislocations 1 and 2, and dislocations 3 and 4, with NNNAPB coupling dislocations 2 and 3, Figure 1.6.

In addition, superlattice dislocations are not restricted to the {110} planes. Just as in bcc metals, any plane contained within the $\langle 111\rangle$ zone is a valid cross-slip

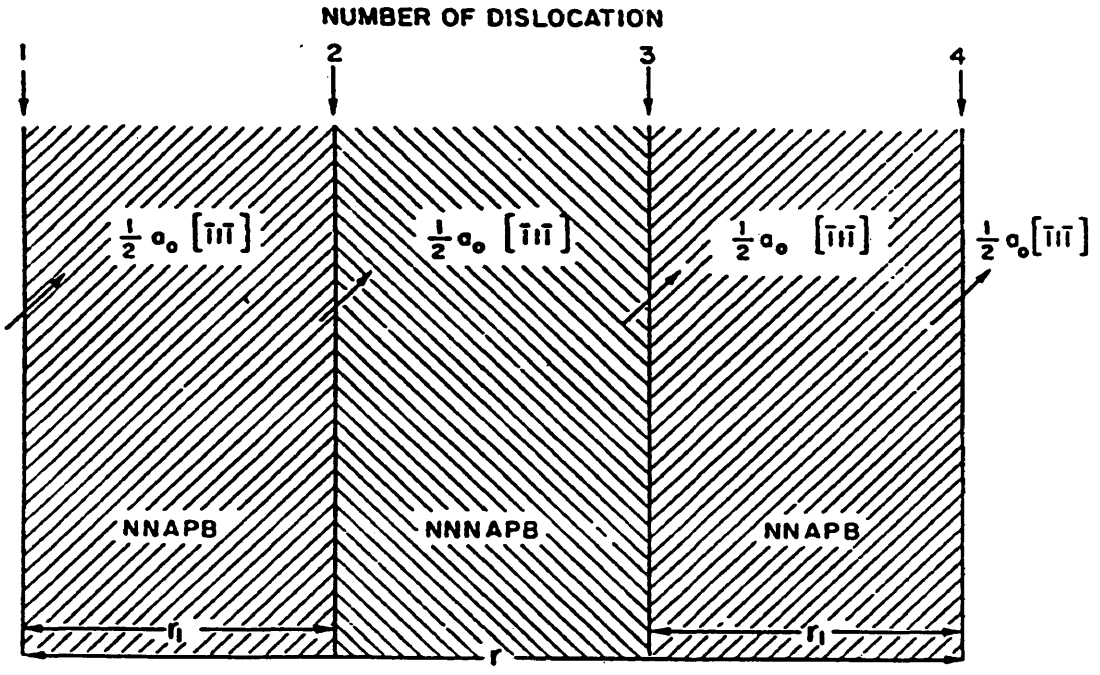

Figure 1.6 Four-fold superlattice dislocation in the DO_3 structure. For this designation, $a_o = a_o'/2$. After Marcinkowski and Brown (16).

plane. Thus, cross-slip is expected to occur on {112} and {321} planes in addition to the primary {110} slip planes. A plot of calculated APB energies between {110} planes and {112} planes is shown in Figure 1.7. There is only a 15 percent difference in APB energies between these two slip planes, which would indicate the potential for activating slip on other slip planes.

1.4.2 Deformation Behavior of DO_3-Ordered Fe_3Al

Transmission electron microscopy (TEM) observations (16) of a near stoichiometric (25.5 at. pct Al) alloy which was cold rolled, indicated the presence of ordinary $a_o'/4\langle 111\rangle$-type screw dislocations creating APB trails as they moved. Marcinkowski and Brown concluded that the APB energies in Fe_3Al were low enough to allow large extensions of individual dislocations. Also, indications of cross-slip of screw dislocations onto slip planes within the $\langle 111\rangle$ zone were evident in the near stoichiometric alloy.

In support of Marcinkowski and Brown's results, compression tests were conducted on polycrystalline (17) and single crystal alloys (18) containing up to 30 at. pct aluminum and possessing the DO_3 structure. The room temperature compression properties revealed that alloys containing less than 27 at. pct aluminum yielded at high

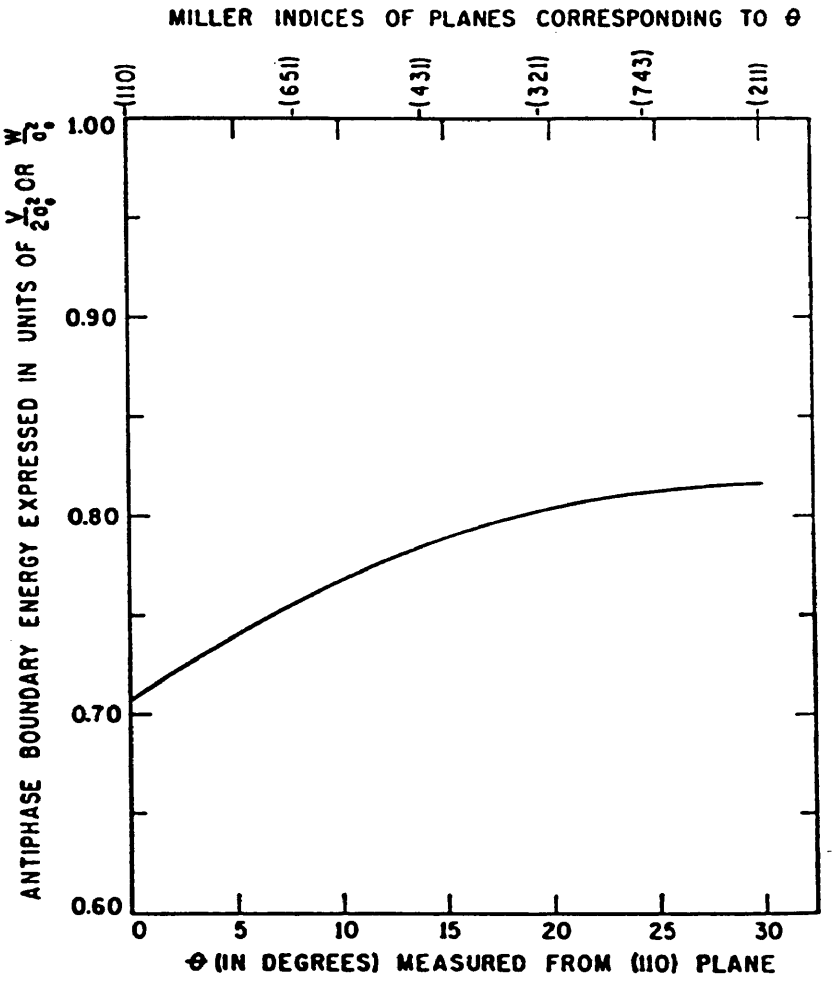

Figure 1.7 Variation of APB energy with orientation of slip plane. After Marcinkowski and Brown (16).

stresses, and plastically deformed via parabolic strain hardening. This behavior was attributed to the nucleation of individual dislocations upon yielding, and subsequent cross-slip with further plastic deformation. However, when tested at higher temperatures (573 K to 655 K), these alloys exhibited two linear stages of strain hardening before parabolic behavior commenced.

In contrast, alloys containing 27 or 30 at. pct aluminum yielded at low stresses, and plastically deformed with two linear work hardening stages before the onset of parabolic work hardening, Figure 1.8.

The first two linear stages were attributed to the nucleation, interaction, and pile-up of superlattice dislocations on slip planes after yielding. Each linear stage corresponded to the motion and interaction of different superlattice dislocation structures. The change from the first linear stage to the second signified the breakdown of the initial superlattice dislocations. Specifically, four-fold dislocations nucleated and continued to move and interact with each other until the resolved shear stress was great enough to overcome the NNNAPB energy coupling dislocations 2 and 3. This allowed the motion of

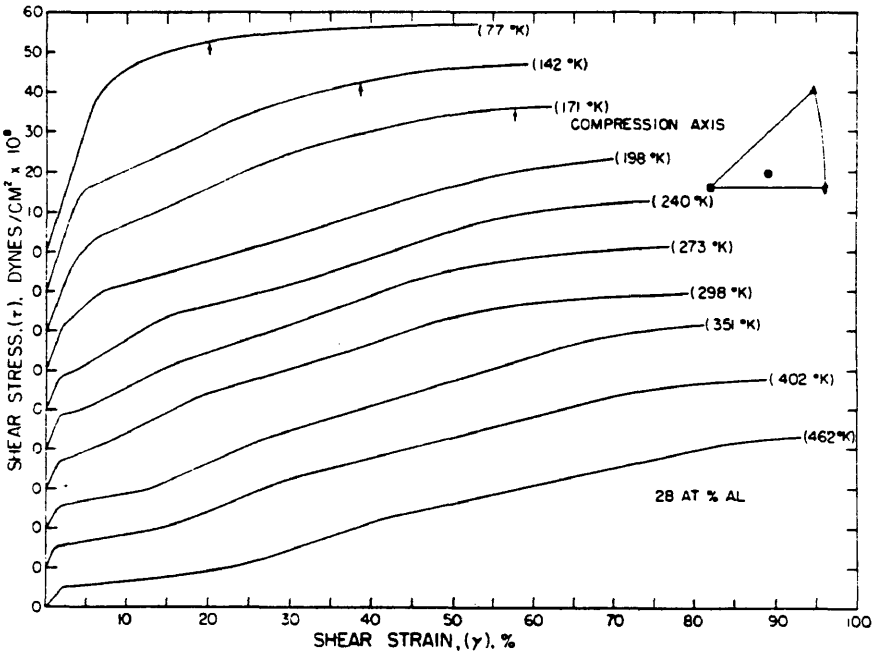

Figure 1.8 Compression curve of single crystal Fe-28 at. pct aluminum alloy. After Leamy and coworkers (18).

dislocation pairs trailing NNNAPB behind them, corresponding to a second linear work hardening stage. Once the resolved stress on the slip planes was great enough to overcome the back stress induced by the NNAPB energy, the dislocation pairs separated into individual dislocations trailing NNAPB. The cross-slip of these individual dislocations corresponded to the parabolic work hardening behavior as postulated by Leamy and coworkers (18). To support the cross-slip mechanism, 28 at. pct alloys were compressed at 77 K. Parabolic behavior was noted after yielding, indicating that thermal activation of superlattice dislocation nucleation was necessary in the DO_3 structure. Dislocations were wavy when observed during TEM. The dislocation configurations responsible for the various stages of work hardening in alloys containing greater than 27 at. pct aluminum are summarized in Figure 1.9.

TEM observations of foils (19) obtained from 28 at. pct aluminum single crystal compression specimens revealed that cross-slip of screw dislocations was not evident during the linear work hardening stages at 198 K. This indicated that there must be a high density of dislocations creating a uniform substructure on the slip plane. It suggested that when the motion of a superlattice dislocation through a dense primary array is difficult, it leads to uncoupling of

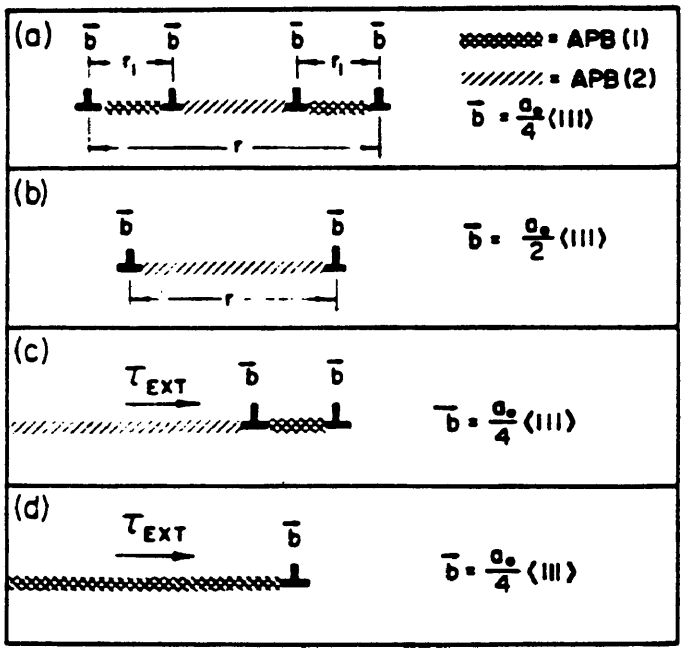

Figure 1.9 Possible dislocation configurations in the DO_3 superlattice. After Leamy and coworkers (18).

the individual dislocations. A dislocation pinning model was proposed to explain the compositional dependence of the strain hardening behavior. As superlattice dislocation loops expanded and interacted with increasing strain, segments of these loops became pinned and the obstacle spacing on the slip plane decreased. As the resolved shear stress increased past the point where it overcame the back stress induced by the NNNAPB energy, the pinned superlattice segments uncoupled to form imperfect superlattice dislocation loops with a far greater effective spacing. These loops could expand and interact in a fashion similar to that previously described. This uncoupling mechanism was proposed to continue as individual dislocation loops were created. Since the NNNAPB energy is a maximum at the stoichiometric composition (17), so too will be the incidence of pinning because the stress field around the superlattice dislocation increases with decreased spacing. This leads to a high stress necessary to break pinned dislocation segments at yielding.

Marcinkowski and Lasko (20, 21) developed a similar dislocation locking theory to explain the rapid work hardening in DO_3-ordered Fe_3Si. TEM observations revealed only parallel and straight screw dislocations on slip planes, indicating that cross-slip was not evident in these

alloys. Thus, the high work hardening rates could be attributed to this lack of cross-slip. The reasons behind this involved the locking of opposite-signed dislocations (2 and 3, Fig. 1.10) by attractive forces between closely spaced parallel slip planes. Once these dislocations locked, it required increasing the stress necessary to free the leading and trailing dislocations (1 and 4, Fig. 1.6) from the dislocation lock and APB.

Stoloff and Davies (2) postulated that the peak in flow stress of DO_3-ordered Fe_3Al is a consequence of a transition from the motion of perfect superlattice dislocations in a highly ordered lattice at lower temperatures to the motion of individual dislocations in a partially ordered (short range ordered) matrix at higher temperatures. Thus, a peak in the flow stress is expected to occur at some intermediate degree of long range order. Their experimental results are shown in Figure 1.11.

Stoloff and Davies took into account Marcinkowski and Miller's theory (22) that the dislocation spacing is dependent on the degree of long range order in the lattice. Thus for a material with a low degree of long range order (appreciable short range order), individual dislocations would be expected to control the deformation behavior in the partially ordered lattice. As the degree of long range

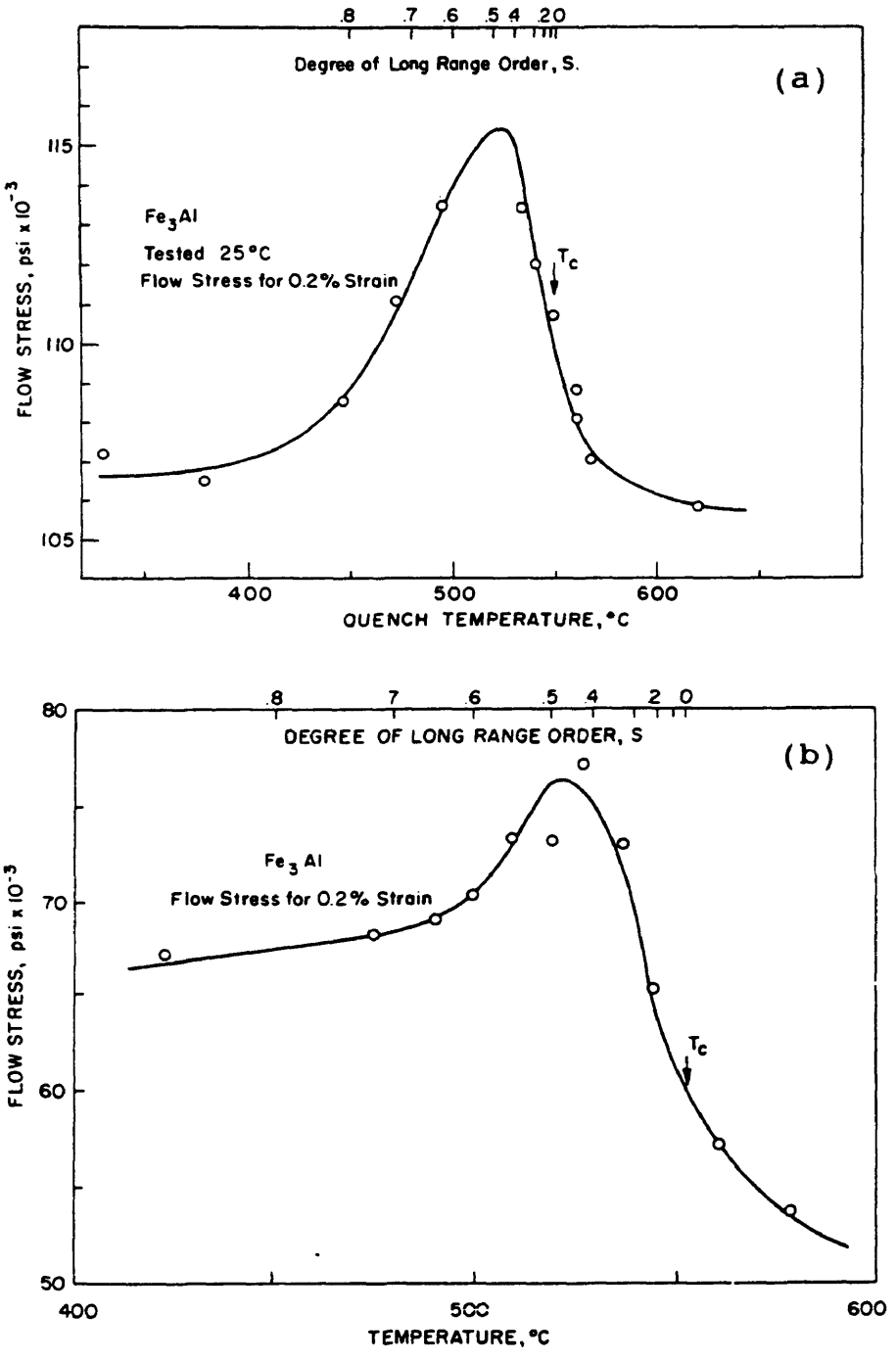

Figure 1.10 Flow stress values versus quench temperature (a) and test temperature (b) for DO_3-ordered iron-24.6 at. pct aluminum alloy. After Stoloff and Davies (2).

order increased, there would be restraining forces on the individual dislocations because of APB creation, leading to hardening of the matrix. Thus for deformation in the DO_3 lattice, the spacing of dislocations 2 and 3 will vary with temperature (LRO), Figure 1.12 (2).

1.4.3 Dislocations in the B2 Superlattice

Dislocations in the B2 superlattice will theoretically have two slip systems which will produce lattice translations, as described next.

1.4.3.1 Fully Ordered B2 Structures. Fully ordered stoichiometric B2 compounds are theoretically expected to deform via the $\{110\}\langle 100\rangle$ slip system since the $a_o\langle 100\rangle$ vector is the shortest lattice translation vector for this ordered structure. An example of this behavior is the deformation of CsCl. However, room temperature studies of dislocations in FeAl support the motion of $a_o\langle 111\rangle$ type dislocations on $\{110\}$ planes (23). This is because the NNAPB energy in FeAl (Al > 36 at. pct) is so high that dislocation pairs can not be resolved by TEM. High temperature studies of dislocations in B2 structures have revealed a transition temperature which increases with increasing deviation from stoichiometry towards the iron

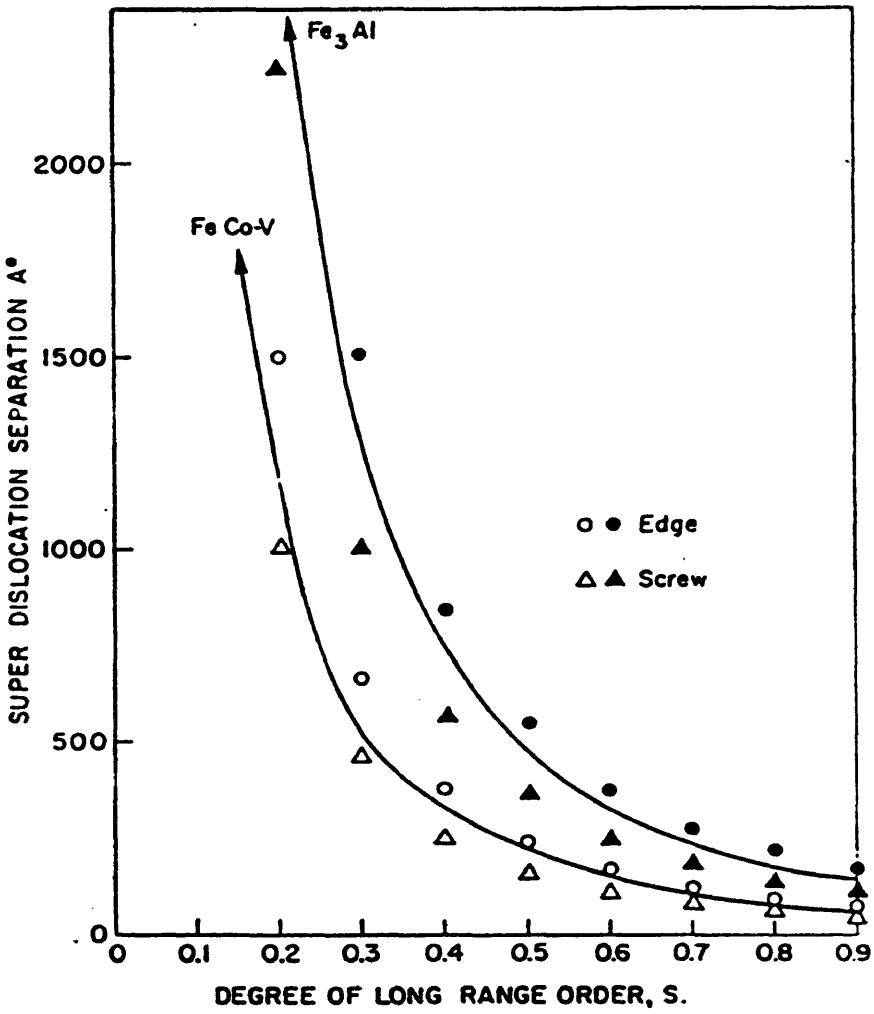

Figure 1.11 Superlattice dislocation spacing and long range order (temperature) for Fe_3Al (DO_3) and FeCo-V (B2). After Stoloff and Davies (2).

rich side (20, 21). This temperature defines the transition from {110}⟨111⟩ type slip to {110}⟨100⟩ type slip. This is similar to the change in slip systems for $L1_2$-ordered alloys such as Ni_3Al.

1.4.3.2 Partially Ordered B2 Structure. In the case of a partially ordered B2 superlattice structure, such as Fe_3Al quenched from above 550°C or deformed above this temperature, deformation is expected to occur by the movement of two $a_o/2\langle 111\rangle$ type dislocations bounded by NNAPB on {110} planes, as theorized by Marcinkowski and Brown (16), Figure 1.13. Since the temperature defining the transition to {110}⟨100⟩ type slip increases with increasing iron content for FeAl, this slip system is not expected to operate for alloys based on Fe_3Al with the B2 structure.

1.4.4 Deformation Behavior of B2-Ordered Fe_3Al

The deformation behavior of B2-ordered Fe_3Al has not been extensively studied, but Leamy and coworkers (18) compressed a 28 at. pct aluminum specimen at room temperature which was initially quenched from 1100°C, and expected to have the B2 structure. Using the analysis for the DO_3 ordered alloys, the specimen revealed only one linear work hardening stage after yielding, followed by

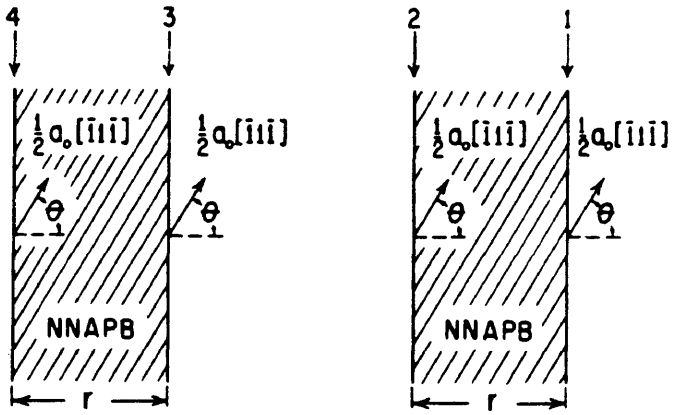

Figure 1.12 Superlattice dislocation in the B2 structure. After Marcinkowski and Brown (16).

parabolic work hardening. This behavior was attributed to the nucleation of superlattice dislocations (dislocation pairs) after yielding, with the uncoupling of the dislocations at the onset of parabolic behavior.

1.4.5 Antiphase Boundary Energies in Fe_3Al-based Alloys

Antiphase boundaries (APBs) are ordering faults created by movement of individual dislocations on slip planes. They also create back stresses on moving dislocations, similar to stacking faults in fcc alloys. Thus, the energy of the APB will have a large effect on the dislocation motion in the ordered material. The factors which affect APB energy will now be described.

1.4.5.1 Atomic Interactions and Order Effects.

The energy associated with APBs in DO_3-ordered Fe_3Al is dependent on both the nearest neighbor and next-nearest neighbor interaction energies, and on the degree of long range order (15). Thus, in the case of slip-produced APBs, the spacing between individual dislocations will be dependent not only on the degree of long range order, but also the strength of the interaction energy between unlike nearest neighbors and next-nearest neighbors. Since slip-produced APBs are similar to the stacking faults between

partial dislocations in fcc lattices, there will be an inverse relation between the APB energy and the individual dislocation spacing in DO_3 ordered Fe_3Al.

Leamy and Kayser (17), accounting for site occupation probabilities, determined the APB energies between nearest neighbors and next nearest neighbors in Fe_3Al is a function of the long range order parameter and interaction energies according to the following equations:

$$\gamma_1 = \frac{2\sqrt{2}}{a_0^2} \left[4\, E_{NN}\, S_{NN}^2 + E_{NNN}\, (S_{NNN}^2 - 4\, S_{NN}^2)\right] \qquad (1.1)$$

$$\gamma_2 = \frac{2\sqrt{2}}{a_0^2} \left[2\, E_{NNN}\, S_{NNN}^2\right] \qquad (1.2)$$

where γ_1 and γ_2 are NNAPB and NNNAPB energies, respectively, E_{NN} and E_{NNN} are the nearest and next-nearest neighbor interaction (ordering) energies, respectively, and S_{NN} and S_{NNN} are the long range order parameters for each interaction. Because the APB energy will vary with long range order, so will the dislocation spacing in Fe_3Al at different temperatures, as shown by Stoloff and Davies (2).

1.4.5.2 Effect of Binary Alloy Composition. In terms of stoichiometry, the highest interaction energy for any ordered compound will occur at the stoichiometric

composition. That is, the maximum next-nearest neighbor interaction energy will occur for a Fe-25 at. pct Al. alloy (Fe_3Al). This is also the composition where the maximum degree of long range order will occur since deviations from stoichiometry will disrupt the long range periodicity in the superlattice. Leamy and Kayser (17), Crawford (25), and Crawford and Ray (26) found the APB energies in the iron-aluminum alloy system varied with aluminum content. A maximum in next-nearest neighbor APB energy (NNNAPB) occurred at the stoichiometric composition, and decreased in an almost linear fashion for higher aluminum contents, Figure 1.14 (18). The decrease in NNNAPB energy with increasing aluminum content results in further separation of dislocations 2 and 3 which make up the four-fold DO_3 superlattice dislocation. For the case of NNAPB energy in DO_3, it did not change much with increasing aluminum content (25), also shown in Figure 1.14. From Crawford and Ray's research (26), the dislocation pairs (1 and 2, 3 and 4) are so closely spaced in alloys over 30 at. pct Al, that all that can be resolved is the NNNAPB between dislocations 2 and 3.

1.4.5.3 Effect of Chromium. McKamey and coworkers (27) studied the effect of chromium additions on the deformation behavior of Fe-28 at. pct aluminum Fe_3Al with

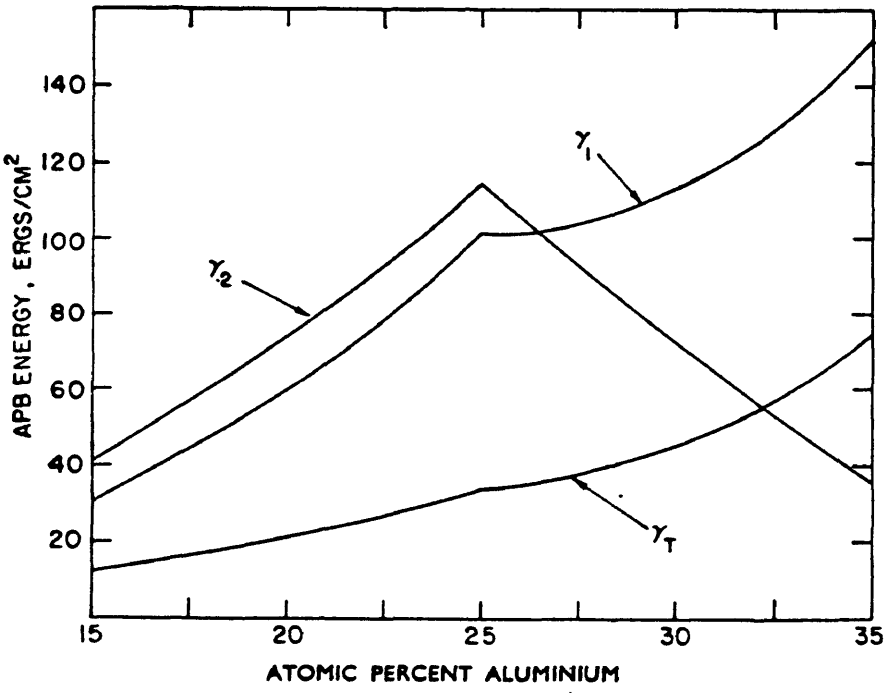

Figure 1.13 Antiphase boundary energy and aluminum content for DO_3-ordered Fe_3Al alloys. After Leamy and coworkers (18).

the DO_3 structure. Their results indicated that chromium significantly reduced the NNNAPB energy, leading to deformation essentially by motion of dislocation pairs with NNNAPB trails, compared to the binary alloy ($Fe_{72}Al_{28}$). NNAPB energy was also reduced, but to a smaller extent.

1.4.5.4 APB Energies in B2-Ordered Fe_3Al Alloys For the case of B2-ordered Fe_3Al alloys, the nearest neighbor APB energy (NNAPB) increased with increasing aluminum content, Figure 1.15 (25). This implies that the individual dislocation spacing for the B2 superlattice dislocation will be decreased for higher aluminum content alloys (> 36 at. pct).

1.5 Antiphase Domains in Fe_3Al-based Alloys

Antiphase domains (APDs) form below the ordering transition temperature upon cooling. Domains are ordered regions which nucleate homogeneously and grow on particular sublattices of the formerly disordered material. When neighboring domains nucleate on different sublattice sites and grow until they impinge, the interface separating them is a planar ordering fault. This ordering fault is a result of similar atomic bonds (A-A or B-B bonds) across the interface of the domains, and is known as an antiphase

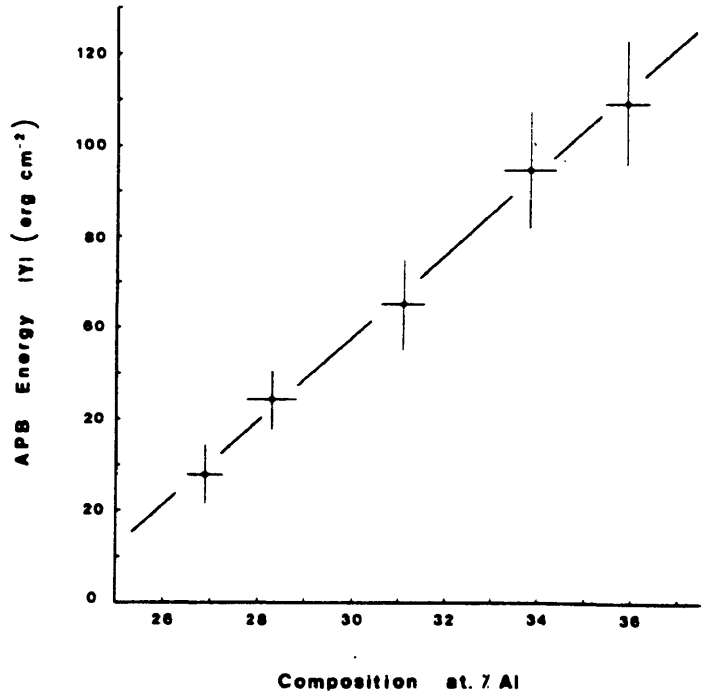

Figure 1.14 Nearest neighbor antiphase boundary energy and aluminum content for B2-ordered Fe_3Al alloys. After Crawford and Ray (26).

domain boundary (APDB). A schematic diagram is shown in Figure 1.16 (28). This fault is similar to the slip-produced antiphase boundary, and both nearest neighbor (NN) and next-nearest neighbor (NNN) domain boundaries exist in DO_3-ordered Fe_3Al. The stability of these domain structures depends heavily upon the number of ordering variants in the superlattice structure and composition. Growth variants relate to the number of sublattices upon which domains nucleate, grow, and intersect, while composition determines the relative growth rate of the APDB interface. According to Beeler (28) four variants are required to create a stable domain structure. Additionally, composition affects the morphology of the APDs.

Because of the ability to possess two ordered structures (B2 and DO_3), different APD networks can be achieved in Fe_3Al-based alloys.

1.5.1 Antiphase Domains in the B2 Superlattice

Upon cooling from above the $\alpha \rightarrow$ B2 transition temperature, B2 domains nucleate and grow on both sublattices (corner sites or body centering sites) in the disordered matrix until they impinge upon each other. This means that there are only two ordering variants in the B2 superlattice. Also, the fault consists of an $a_o/2\langle 111\rangle$

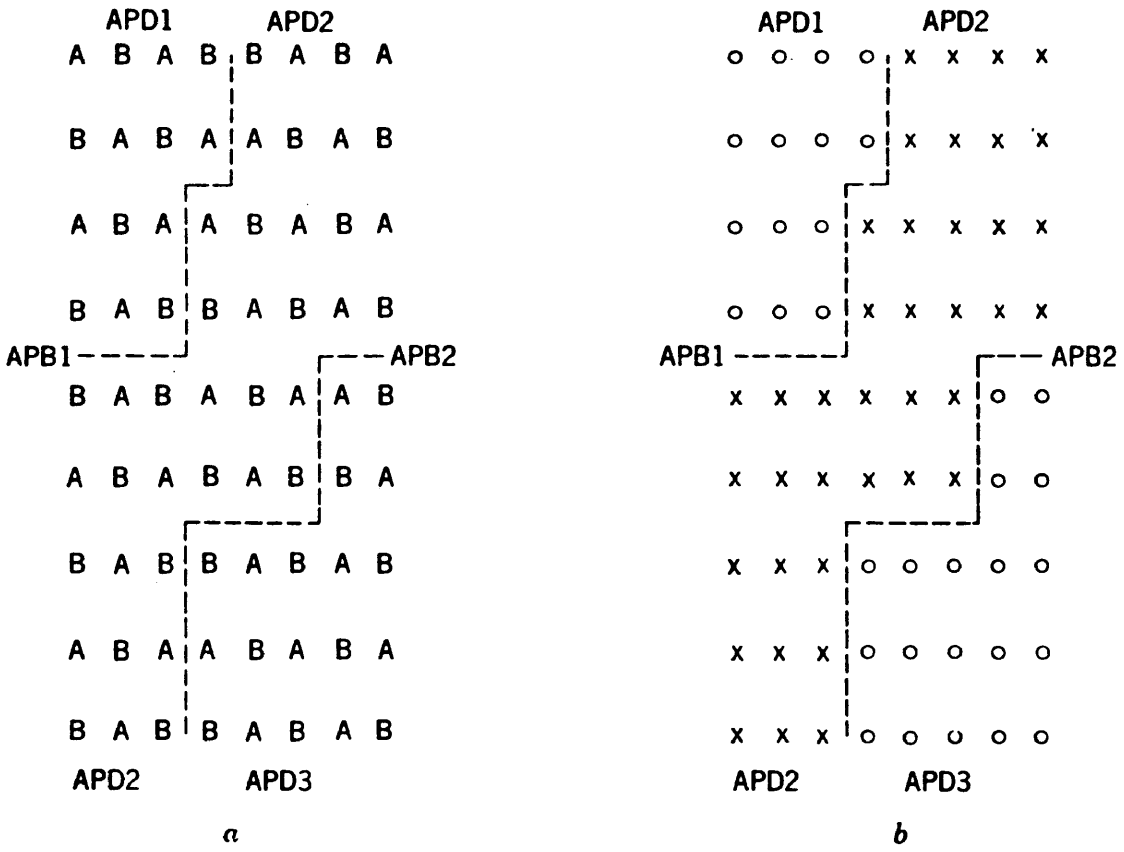

Figure 1.15 Schematic of antiphase domains (APDs) and associated antiphase domain boundaries (APDBs). After Beeler (28).

displacement on {110} planes, and is therefore not predicted to create a stable APD structure, Figure 1.17. Marcinkowski and Brown (29) confirmed the APDB fault vectors for B2 ordered Fe_3Al containing 25.5 at. pct aluminum, and revealed their thermal instability through transmission electron microscopy (TEM). They showed that quenching from 900°C (100°C above the $\alpha \rightarrow$ B2 transition temperature) did not suppress the transformation, and resulted in a relatively fine (25nm) B2 APD size. However, annealing at 600°C for one hour (50°C above the B2 $\rightarrow DO_3$ transition temperature) resulted in a B2 domain size of 900nm. These findings supported the predicted thermal instability of the B2 antiphase domain structure.

Additionally, the stability of the domain structure is dependent upon alloying, especially aluminum content. Krzanowski and Allen (30, 31) found that segregation of iron atoms to the APDBs in B2 ordered Fe_3Al had significant effects on the domain growth kinetics at temperatures where the alloys equilibrated within the α + FeAl miscibility gap (see Figure 1.2b). Iron-24 at. pct aluminum alloys annealed at 860 K (587°C) and quenched showed no APDB contrast in bright field TEM, indicating equilibration in a single phase B2 phase field. However, when annealed at 855 K (582°C), APDB contrast was obtained in bright field, indicating that

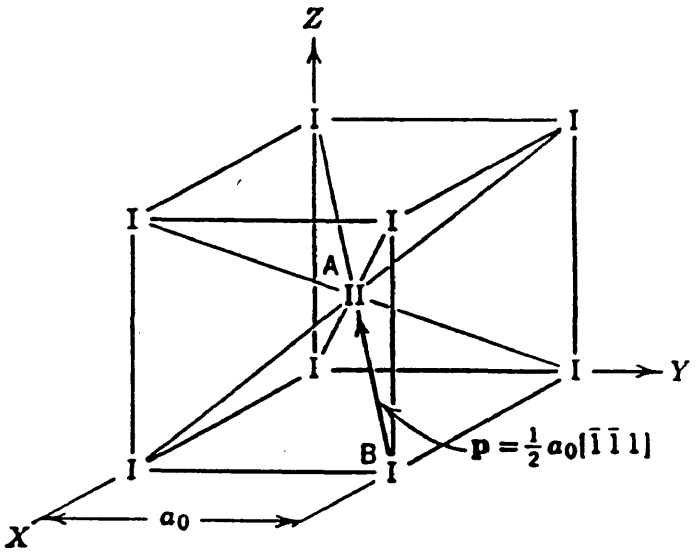

Figure 1.16 APDB fault vector in the B2 superlattice. After Beeler (28).

the anneal was performed in the two phase α + B2 field with a disordered film wetting the APDBs. The presence of the disordered film reduced the APDB migration velocity by a factor of two compared to the APDBs which had no disordered films.

Studies of rapidly solidified ordered iron alloys (32) revealed that changes in alloying and transition temperature were the main factors in determining B2 domain size. Increasing silicon content in Fe-Si alloys increased the $\alpha \rightarrow$ B2 transition temperature, but did not result in finer B2 domain sizes. Domain sizes were similar in Fe-12.1 and Fe-13.9 at. pct silicon alloys even though the transition temperature increased with alloying content. Also, a rapidly solidified Fe-26 at. pct Al alloy which had a similar transition temperature as the Fe-13.9 at. pct silicon alloy, had similar domain sizes as the Si-based alloys. These results indicated that even though the B2 structure was further stabilized by alloying, the kinetics of the order-disorder process were enhanced due to higher atomic mobility at the higher transition temperature.

1.5.2 Antiphase Domains in the DO_3 Superlattice

If the material continues to cool below the B2 $\rightarrow$ DO_3 transition temperature, DO_3 domains homogeneously form

within the former B2 domains, creating a finer domain structure, Figure 1.18. As with B2 domains, the DO_3 domains nucleate, grow and impinge upon each other, creating DO_3 APDBs. Since DO_3 structures depend upon both the nearest neighbor and next-nearest neighbor ordering, both types of APDBs exist in DO_3 APD structures. APDBs which have a $a_o'/4\langle 111\rangle$ type fault vector disrupt nearest neighbor bonds, which actually is the fault vector remaining from when the material was B2 (29). The other fault vector consists of a $a_o'/2\langle 100\rangle$-type displacement, which disrupts the next-nearest neighbor bonding (29). It is these types of faults which commence upon ordering in the DO_3 structure. The APDB fault vectors in the DO_3 structure are summarized in Figure 1.19. The DO_3 APD structure is more stable than the B2 APD structure since there are now four growth variants instead of two. Stability arises from the intersection of the different APDB fault vectors. Also, these boundaries do not have any preference to lie on particular lattice planes, which results in wavy, isotropic appearances.

1.5.3 Effects of Domains on Material Properties

Because APDs are possible barriers to dislocation motion, their effects on the deformation properties of ordered alloys is essential. This was particularly true for

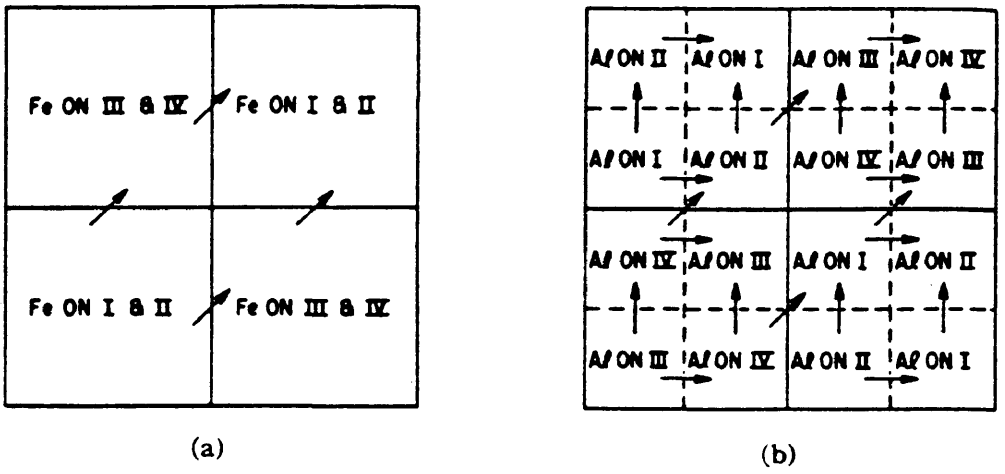

Figure 1.17 Schematic illustrating DO_3 APD structure within the B2 APDs. After Marcinkowski and Brown (29).

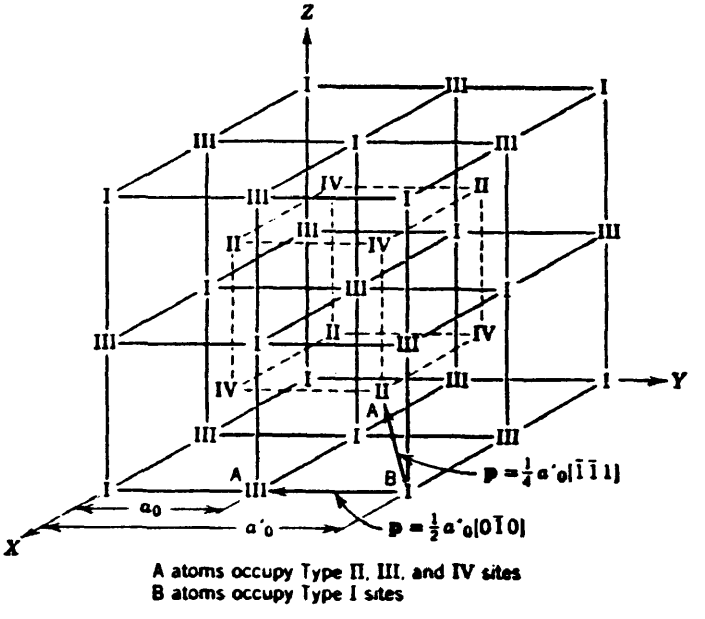

Figure 1.18 APDB fault vectors in the DO_3 superlattice. After Beeler (28).

the case of chromium-modified Ni_3Al (1).

1.5.3.1 Davies' Model for Fe_3Al. Davies' study (33) involved coarsening DO_3 domains by annealing a quenched Fe-24.6 at. pct aluminum alloy below the B2 → DO_3 transition temperature. This study revealed a maximum in hardness at a long range order parameter (S) equal to 0.4-0.5, which was in agreement with flow stress results of Stoloff and Davies (2). DO_3 domain sizes, however, were extremely fine (35Å) to be effective in hardening the matrix, as shown in Fig. 1.19. Also, annealing for 10 minutes at 290°C created the fine domain structures. Hardening of the alloy was attributed to the interaction of imperfect superlattice dislocations (pairs or individuals) with domain boundaries in a short range ordered matrix. This was a result of the short times at moderate temperatures which created a fine domain network, and corresponded to an intermediate degree of long range order.

1.5.3.2 Marcinkowski and Fisher's Model for Fe_3Al. Marcinkowski and Fisher (34) developed a theoretical analysis of plastic deformation in superlattices based on the bcc structure. The main interest was in the effects of antiphase domain structures on the physical properties of

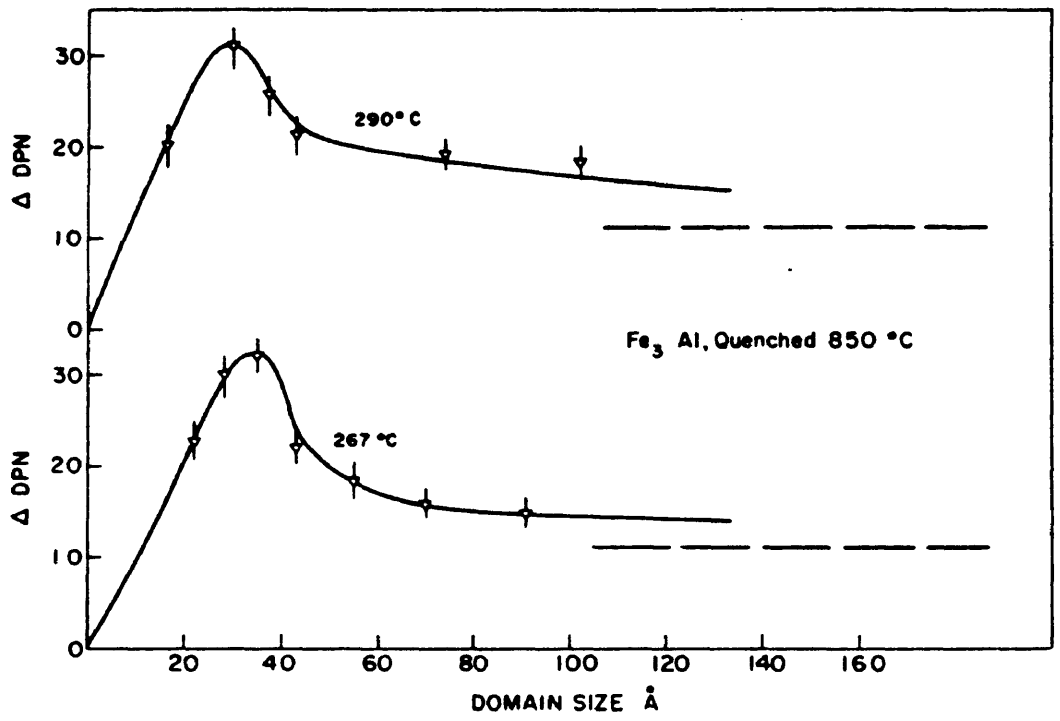

Figure 1.19 Microhardness versus DO_3 domain size for Fe-24.6 at. pct Al Alloy. After Davies (33).

Fe_3Al with either the B2 or DO_3 superlattice structures. Their findings indicated an intermediate APD size in either ordered structure ($d=4a_o$ in B2 structure, $d=4a_o'$ in DO_3 structure) would effectively uncouple the superlattice dislocations, leading to motion of individual dislocations in a partially ordered lattice. For the B2 superlattice, the stresses to move individual dislocations and superlattice dislocations through an APD network are shown in Figure 1.21. At small APD diameters corresponding to intermediate long range order, the separation of the superlattice dislocations was great, as seen in Fig. 1.22. Also, at these values of APD diameters, the stress to move individual dislocations through the network is not much greater than the stress to move superlattice dislocations, Fig. 1.21. Included in this plot is the effect of APD diameter on the twinning stress. As can be seen, this stress is much greater than the other curves, but is only important for deformation below room temperature or at high strain rates.

1.6 Environmental Embrittlement and Fe_3Al Alloys

Environmental embrittlement entails the interaction of some chemical species present in the environment with the material, which causes a macroscopic degradation of material

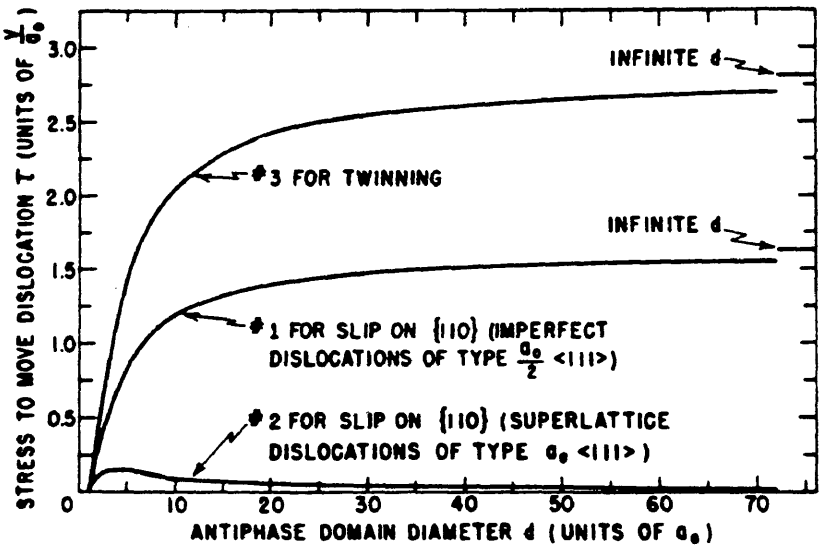

Figure 1.20 Shear stress versus APD diameter for B2-ordered alloys. After Marcinkowski and Fisher (34).

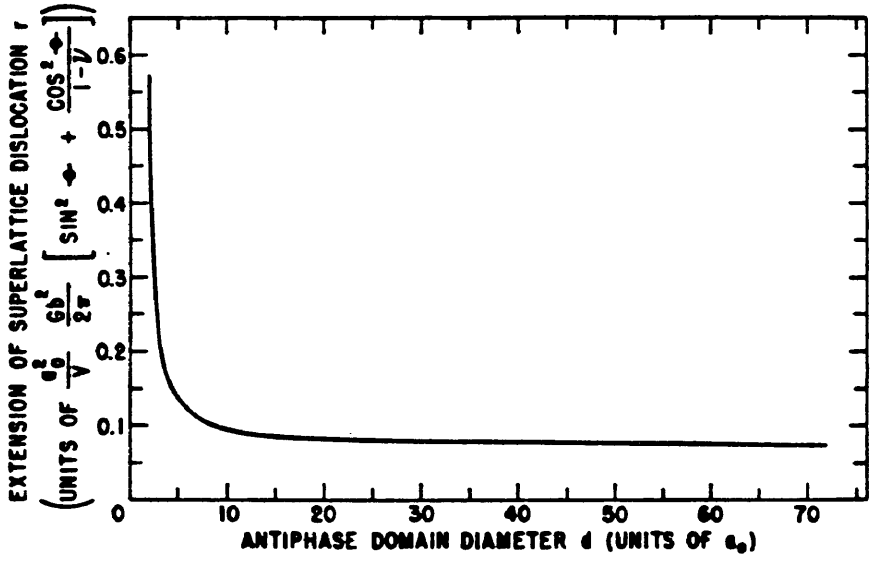

Figure 1.21 Separation of superlattice dislocations with APD diameter for B2 ordered alloys. After Marcinkowski and Fisher (34).

properties, most notably ductility and UTS. The first indication that iron aluminides were susceptible to environmental embrittlement at ambient temperatures came from the results of Liu and coworkers in their tensile studies of FeAl-based (B2) Fe-36.5 at. pct aluminum alloys (35), and Fe-28 at. pct aluminum Fe_3Al-based (B2 or DO_3) alloys (36) in various environments. It was found that environments containing water vapor decreased the room temperature ductility and UTS compared to vacuum, oxygen, or dry hydrogen environments. Thus the reaction of water vapor with the material caused an embrittlement phenomenon which is closely linked to hydrogen embrittlement of other alloys. Before examining the direct cause of environmental embrittlement in iron aluminides, different theories which explain the results of materials exposed to hydrogen-bearing environments will be reviewed.

1.6.1 Hydrogen Embrittlement Theories

An excellent review on hydrogen effects in iron and steel has been performed by Hirth (37). The major points of his review will be discussed, along with findings from other researchers.

1.6.1.1 Hydrogen Diffusion. - The first theory explains hydrogen damage as the result of atomic hydrogen diffusing into the matrix ahead of a crack, and locally softening the matrix. This provides for enhanced dislocation motion ahead of the crack, allowing increased microvoid nucleation and coalescence. Hydrogen embrittlement is therefore a microscopically ductilizing process which leads to a decrease in the macroscopic ductility and ultimate tensile strength (UTS). This requires that the molecular hydrogen dissociate via the following reaction:

$$H_2(g) = 2H(g) \qquad (1.3)$$

The important step is determining how the hydrogen first comes into contact with the material. This step is known as adsorption.

1.6.1.2 Hydrogen Adsorption. - A second theory uses an adsorption mechanism to explain hydrogen damage. As will be explained shortly, adsorption of molecular or atomic hydrogen to cracked surfaces, and subsequent diffusion of atomic hydrogen into this region enhances dislocation motion which is localized to the crack region. This causes localized ductile rupture leading to macroscopic decreases in both ductility and UTS.

1.6.1.3 Adsorption and Decohesion. - The third embrittlement model involves hydrogen adsorption and the subsequent decrease in fracture (cohesive) strength of the material. The adsorbed atoms decrease the potential energy between nearest neighbors, thus decreasing the stress required to break the atomic bonds.

1.6.2 Hydrogen Embrittlement of Iron Alloys

Although many studies have been done concerning the effects of hydrogen on iron and its alloys, the purpose of this discussion is to highlight a few of the important findings which may be applicable to the iron-aluminum alloy system.

Ransom and Ficalora (38) studied the influence of hydrogen chemisorption on iron magnetization. Molecular hydrogen (H_2) was postulated to adsorb onto the surface of iron via the following reaction:

$$H_2(g) = H_2^+(ads) + e^- \qquad (1.4)$$

The result was a decrease in magnetization due to a decrease in unpaired d-electrons responsible for magnetization in the iron atoms. This result was also interpreted as a metal-H_2^+ bond (38). Furthermore, the adsorbed H_2^+ species could then

react with available electrons via the following reaction:

$$H_2^+(ads) + 3e^- = 2H^-(ads) \qquad (1.5)$$

The adsorbed H^- was recognized as the embrittling species, according to an earlier study by Pecora and Ficalora (39). This reaction caused an increase in magnetization, meaning an increase in the number of unpaired d-electrons occurred.

Since the adsorption process involves two steps, one reaction will be rate controlling compared to the other at different temperatures. The first reaction has been observed to go to completion at temperatures below 300K. That is, the bulk of the adsorbed species will exist below 300 K as H_2^+. Above 300K, the second reaction goes to completion. That is, the bulk of the adsorbed species will exist above 300K as H^-. It should also be remembered that the concentration of H^- adsorbed is dependent upon the H_2^+ concentration. Thus below 300K the second reaction is rate controlling, whereas the first reaction is rate controlling above 300K. Fig. 1.22 shows H^- population with temperature, indicating that near room temperature, the maximum population will be present. Fig. 1.23 shows that the adsorption rate of $H_2(g)$ on iron decreases with increasing temperature. These figures are used to elucidate what

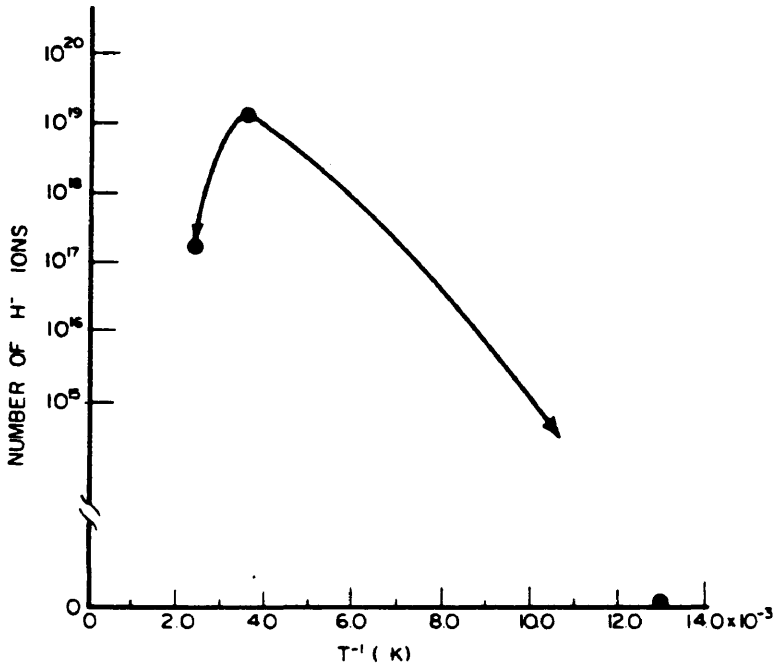

Figure 1.22 H^- population versus 1/T for iron. After Ransom and Ficalora (38).

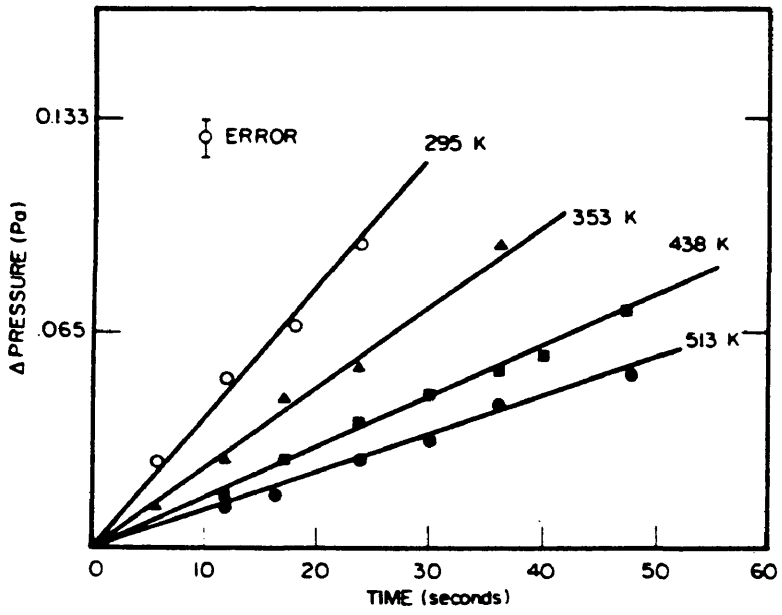

Figure 1.23 Adsorption rate of H_2 on iron (slope of pressure versus time curve) and temperature. After Ransom and Ficalora (38).

happens with the hydrogen cracking frequency with temperature, as postulated in Fig. 1.24, which also indicates the controlling adsorption process for the different temperature regimes.

Lynch (40) presented results which were reasoned to be associated with adsorption phenomena. Lynch compared liquid-metal induced embrittlement (LMIE) and hydrogen embrittlement (HE) of a tempered martensitic steel, and concluded that both showed similar fracture behavior. Since an important step in LIME is associated with adsorption of the liquid species onto crack surfaces, Lynch proposed that a similar phenomenon occurs for hydrogen. The hydrogen adsorption facilitated the nucleation of dislocations from crack tips. Lynch's proposed mechanism is shown in Fig. 1.26 for both LIME and HE. Also, considerable diffusion was postulated to occur after adsorption. Therefore, hydrogen diffusion into the matrix and its interaction with dislocations at the cracks appear to be the controlling mechanism.

If dislocation motion is enhanced ahead of a crack, then some explanation must exist which adequately describes the phenomena. In their environmental TEM cell experiments on high purity iron, Tabata and Birnbaum (41) observed an increase in the dislocation velocity with increasing

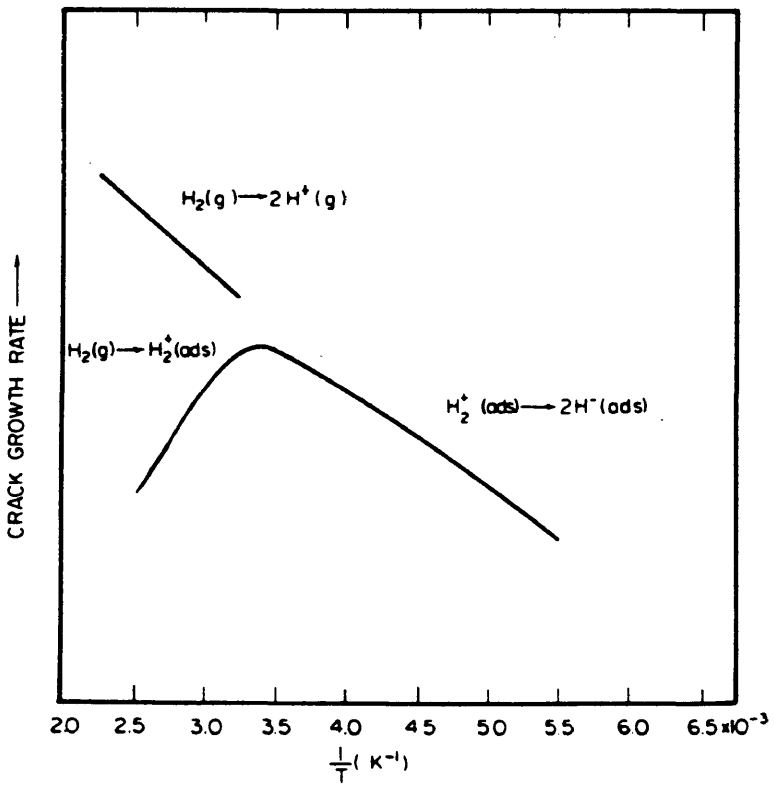

Figure 1.24 Postulated crack growth rate versus 1/T for iron embrittled by hydrogen. After Ransom and Ficalora (38).

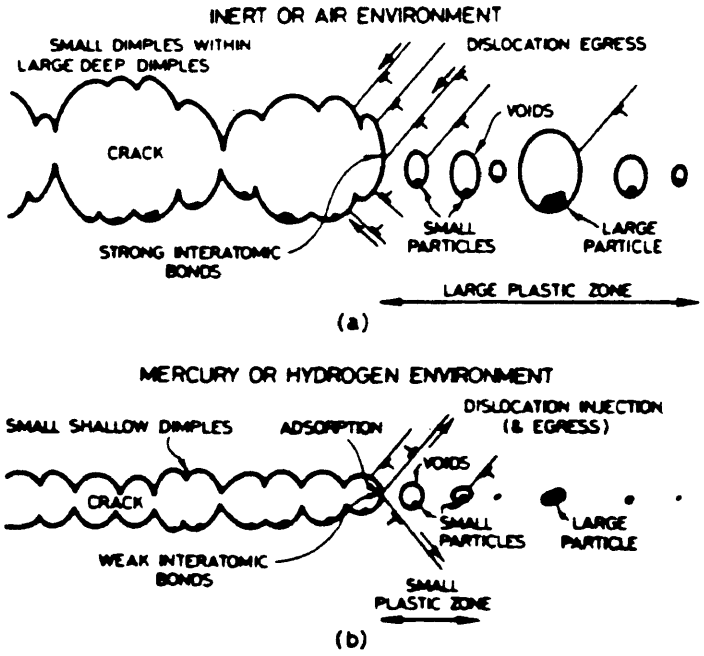

Figure 1.25 Lynch's proposed crack growth mechanism in (a) inert environments, and (b) mercury or hydrogen environments (40).

hydrogen pressure (fugacity). Using the relation describing dislocation velocity:

$$V = V_0 \left(\frac{\tau}{\tau_0}\right)^m \tag{1.6}$$

where V is related to the strain rate according to:

$$\dot{\varepsilon} = \rho\, b\, V \tag{1.7}$$

V_0, τ_0 and m are empirical constants, whereas τ is the flow stress. The value τ_0 is related to the lattice friction stress. Tabata and Birnbaum determined that the flow stress of iron was decreased in the presence of hydrogen. Also, the amount of hydrogen increased in the triaxial stress region ahead of the crack according to the following equation:

$$\frac{C_H^{\sigma}}{C_H^{0}} = \exp\left(\frac{\bar{V}_H\, \sigma_s}{RT}\right) \tag{1.8}$$

where C_H^0 and C_H^{σ} are the atomic hydrogen concentrations in the lattice far away from the crack tip and in the stress field ahead of the crack tip, $\bar{V}_H$ is the partial molar volume of solution of atomic hydrogen in the lattice, σ_s is the spherical component of the stress field, R and T have their usual meaning (42). Dislocation dragging of hydrogen plus the enhanced dislocation mobility resulted in high hydrogen contents in the triaxial stress region.

In terms of fracture behavior, room temperature observations show a ductile mechanism which is highly localized (37, 40). Nakasato and Bernstein (43) studied the crystallographic behavior of hydrogen-induced cleavage cracking in purified iron and iron-silicon alloys. Their x-ray trace and optical observations showed that pure iron cleavage-cracked on {110}-type slip planes after charging with hydrogen, and showed characteristic striations parallel to the crack front with tear ridges perpendicular to the crack direction. Adding silicon changed the crystallographic nature of the cleavage cracks. Cracking was observed to be on {100}-type cleavage planes for iron-3 wt. pct silicon alloys. These fracture surfaces lacked striations and significant tear ridges, in contrast to pure iron. These indicated that the addition of silicon embrittled the iron matrix. Since silicon enhances slip on {110} slip planes in iron (44), the ability of dislocations to cross-slip, or the ability to initiate other slip systems in the matrix will have a significant effect on the fracture behavior. Additionally, iron-silicon alloys can form the DO_3 superlattice structure just as in the iron-aluminum system. Therefore, similar behavior may be expected for the iron aluminides.

1.6.3 Hydrogen Embrittlement of Aluminum Alloys

Because iron aluminides contain at least 24 at. pct aluminum, some understanding of how aluminum alloys are embrittled by hydrogen is necessary since the embrittlement phenomenon will involve both iron and aluminum atoms.

Speidel (45) proposed a mechanism by which aluminum is embrittled by hydrogen. His mechanism was based on the following reaction:

$$2Al + 3H_2O = Al_2O_3 + 6H^+ + 6e^- \qquad (1.9)$$

The presence of water vapor in the atmosphere will react with aluminum to form alumina, while releasing atomic hydrogen which embrittles the material through localized ductile rupture. In contrast, tests performed in dry hydrogen environments did not result in any ductility decrease. This is also in contrast to iron alloys, which are embrittled by dry hydrogen. Whether or not H^+ was released was not apparent. Speidel did not provide evidence that H^+ was the species released. His reasoning was based on the fact that the above reaction is common to aluminum alloys exposed to water. Not emphasizing this dilemma, Speidel attributed the embrittlement phenomenon to the production of diffusible hydrogen, which caused either intergranular or transgranular fracture and macroscopically

lower ductility.

Scamans and Tuck (46), and Ricker and Duquette (47) proposed the formation of hydrated alumina on aluminum alloy surfaces according to the following reaction (47):

$$2Al(s) + (3+X)H_2O = Al_2O_3 \cdot X(H_2O)(s) + 3H_2(g) \quad (1.10)$$

Using X=3 for bayerite, this reaction product reacts further with aluminum via the following reaction:

$$2Al(s) + Al_2O_3 \cdot 3H_2O(s) = 2Al_2O_3(s) + 3H_2(g) \quad (1.11)$$

It was noted that alumina is created in this second reaction, whereas molecular hydrogen gas (H_2) is created in both. Additionally, both sets of researchers observed blistering of the oxide surface. This blistering was related to the rapid evolution of hydrogen gas during the initial reaction between water vapor and aluminum.

With respect to the hydrogen gas released, Scaman and Tuck reasoned that the hydrogen gas dissociated and diffused through grain boundaries. Interestingly enough, their fracture behavior showed all intergranular fracture. Ricker and Duquette reasoned along similar lines, but included that the water vapor must adsorb and react, releasing molecular hydrogen which dissociated into atomic hydrogen. Diffusion of the atomic species to the region ahead of crack tips was postulated to be the main phenomenon which induced

embrittlement. Ricker and Duquette reasoned that diffusion of the atomic hydrogen was the rate limiting step since the rates of surface reactions and adsorption were assumed to be much faster than bulk diffusion.

Bond and coworkers (48), using an in-situ environmental cell TEM technique, deformed pure aluminum foils in wet or dry hydrogen atmospheres. It was postulated from observations that hydrogen decreased the flow stress and enhanced dislocation mobility in front of cracks, similar to the findings for pure iron (41, 42). Fracture was observed as a highly localized ductile process. Atomic hydrogen, which formed from the dissociation of molecular hydrogen under the influence of the electron beam, was deemed responsible for embrittlement.

Thus, considering what has been observed for both iron and aluminum alloys, both atoms will apparently play important roles in the environmental embrittlement of iron aluminides

1.6.4 Hydrogen Embrittlement of Fe_3Al Alloys

Liu and coworkers (35, 36) in their ambient temperature environmental testing of iron aluminides, attributed the embrittlement phenomenon to the reaction of water vapor with aluminum atoms at freshly cracked surfaces during tensile

deformation. The reaction would form alumina, and liberate hydrogen to embrittle the material, according to the reaction postulated by Speidel. Yet no basis for this reaction was given in the work on iron aluminides (35, 36). No real difference in fracture behavior was observed since the typical transgranular cleavage fracture mode of Fe_3Al was independent of environment or the amount of ductility. Thus the environmental embrittlement of iron aluminides shows similarities to the hydrogen embrittlement of aluminum alloys.

1.6.5 Hydrogen Embrittlement of Other Ordered Alloys

Hydrogen embrittlement is not solely a problem in iron aluminides. Co_3Ti (49), Ni_3Fe (50), and Ni_3Al+B (51), all $L1_2$ ordered compounds, are found to be embrittled by hydrogen environments. Cathodically charging with atomic hydrogen (49, 50) or in-situ TEM environmental cell techniques (51) revealed embrittlement phenomena. For the case of boron-doped Ni_3Al (51), it was revealed that the hydrogen environment enhanced dislocation mobility and crack growth. This enhanced dislocation behavior was similar to that of iron (41, 42) and aluminum (48). Fracture behavior of boron-doped Ni_3Al changed from ductile rupture to mixed ductile rupture and intergranular. In terms of environment,

it appears the $L1_2$ compounds are embrittled by dry environments, in contrast to iron aluminides which are embrittled by wet environments. Whether this susceptibility difference is based on alloy elements or crystal structure remains to be seen.

1.7 Summary of Background Information

From the above review, it is apparent that there are many factors controlling the deformation behavior of Fe_3Al-based alloys at ambient or elevated temperatures. It must be emphasized that these factors will contribute to the material's weldability. To summarize, the effects of alloying on APB energies, along with the degree of long range order, will affect the superlattice dislocation motion in iron aluminides, and thus how the material yields and plastically deforms. Also, other factors to consider are APD structures with their associated APDBs, and environmental effects. Taking the above factors into account, plus welding process and the initial condition of the base material, the ability to weld these ordered materials can then be addressed. To date, no published results exist reporting effects of domain structures on the high temperature mechanical properties of Fe_3Al with the B2 structure. It is expected that they may not be beneficial

due to the unstable nature of the APDBs at higher temperatures. For the case of DO_3 domains below 550°C, other than the work of Davies (33), there have not been many studies describing the effects of domains on the material properties. Also, no attempts have been made to signify the effect of either APD structure on weld cracking resistance during cooling.

Both aluminum and iron will play vital roles in the environmental embrittlement of iron aluminides. These materials are not embrittled by dry hydrogen environments, which is attributed to the significant amount of aluminum. This is unlike the behavior of iron or its alloys. However, this large amount of aluminum makes iron aluminides susceptible to embrittlement by the reaction of water vapor with either free aluminum or a hydrated alumina layer. Since hydrogen is released as aluminum is reacted at crack tips, it appears that the embrittlement behavior is similar to both aluminum alloys and iron alloys because of adsorption and diffusion phenomena.

2. EXPERIMENTAL PROCEDURE

2.1 Alloy Selection

Weldability screening tests were performed on a variety of Fe_3Al alloys by Dr. Stan David of Oak Ridge National Laboratory (ORNL) (3, 4). The results of these tests determined that an alloy designated FA-129 had the best weldability characteristics for both electron beam (EB) and gas-tungsten arc (GTA) processes. The composition of this alloy is given in Table 2.1. The hyperstoichiometric aluminum composition was used, since increasing aluminum content improved weldability (10). Chromium was added for slightly improved room temperature ductility (27), and niobium and carbon were added in an attempt to precipitate NbC. However, this and similar alloys were also subject to microcracking across the weld during cooling, even after high heat input welding with the GTA process (4).

Table 2.1 FA-129 Alloy Composition
at. pct (wt. pct)

Fe	Al	Cr	Nb	C
66.3 (77.7)	28.0 (15.9)	5.00 (5.45)	0.50 (0.97)	0.20 (0.05)

2.2 Material Processing

Sheet material (0.76 mm thick) or plate material (10 mm thick) were provided by ORNL. The alloy FA-129 was processed according to the following schedule: ingot preparation consisted of vacuum induction melting and drop casting into water-cooled copper molds. The material was then hot-rolled starting at 1000°C and finished at 650°C. Optical microscopy was used to reveal the microstructures. Polished sheet or plate specimens were etched in a solution of 50% acetic acid, 33% nitric acid, and 17% hydrochloric acid. Images were taken on an AusJena MeF3 or Leco Neophot 21 photomicroscopes.

2.2.1 Stress Relieved Sheet Material

For sheet material, stress relieving was performed at 750°C for one hour followed by oil quenching for the first set of hot ductility specimens. This heat treatment gave an unintentional, finely recrystallized grain structure which was not stable as will be discussed in a future section. For the second set of hot ductility specimens, FA-129 was annealed at 690°C and water quenched. This heat treatment resulted in a partially recrystallized microstructure.

2.2.2 Recrystallized Sheet Material

To create a recrystallized structure, an anneal at 850°C for one hour (10) accomplished this goal.

In terms of long-range order, the partially ordered B2 structure could be quenched-in with the stress-relief anneal, according to x-ray diffraction analyses. The implications of this in relation to the phase transformations in this alloy system will be discussed later.

2.3 Hot Ductility Testing

Hot ductility testing was performed on Gleeble 1500 thermomechanical simulators at ORNL and CSM. Punched sheet specimens or threaded round tensile bars were utilized in the hot ductility testing. The basic premise of the hot ductility test is to fracture the material in tension at a given temperature. This simulates the behavior of the material at temperatures where brittle fracture problems can occur upon cooling of weldments. Brittle fracture regimes based on temperature, cooling rate, or atmosphere can thus be determined for a material.

Type K thermocouple wires (chromel-alumel) 0.010 in. in diameter were percussion welded to the specimen at the

center of the control zone, approximately four wire diameters apart within the same isothermal plane. This allowed for fast response of the thermal control feedback system, according to Duffers, Incorporated (52).

Both the thermal and mechanical signals to the specimen were controlled using computer programs developed with software provided by Duffers Scientific (Gleeble Programming Language). Heating and cooling rates, temperature holds, and deformation rates were tailored using these programs.

In addition, the atmosphere in which the specimen resided was controlled. With the use of jaw extensions, a test chamber has been designed for the Gleeble 1500. The chamber consists of aluminum, with ports drilled and tapped for chamber plugs, gas ports, gas bleed valve, and jaw extension rams. The top is open to the atmosphere, and can be closed by placing a 0.75 in. thick glass plate on top of an o-ring seal. Tests were performed in ambient air, 99.9999% (research grade [RG]) helium, argon plus 99.999% (ultra-high purity [UHP]) helium quench, or UHP helium with 54% relative humidity (He-54% RH).

2.3.1 Testing of Sheet Material

All hot ductility testing of sheet material was performed at an engineering strain rate of $3.3 \times 10^{-3} s^{-1}$. The

first hot ductility tests were performed in ambient air with sheet tensile specimens, Fig. 2.1. These specimens were tested using stainless steel grips which tightened the specimen with allen screws. This combination was then placed within the copper wedge jaws, Fig. 2.2. These are the same grips used for testing nickel aluminide sheet specimens (1). A known GTA weld thermal cycle for iron aluminide sheet, provided by Robbie Reed of ORNL (3), was used in developing Gleeble computer programs, Fig. 2.3. This thermal cycle was recorded from the heat-affected zone of a binary iron aluminide which was GTA welded at 4.2 mm/s, 35 amperes current, and averaged 8.5 volts. These conditions corresponded to a heat input of 159 cal/cm. Pulling in tension until fracture at a desired control temperature was performed on either the heating portion or the cooling portion of the thermal cycle. Ductility was measured as percent reduction of area of the failed specimens. The final reduced area was calculated from SEM micrographs.

After being informed about environmental embrittlement of iron aluminides by water vapor (35, 36), the next set of sheet specimens were tested in a helium atmosphere using RG helium, containing less than 0.5 ppm of the following impurities: H_2O, H_2, and O_2. Other impurities of the same

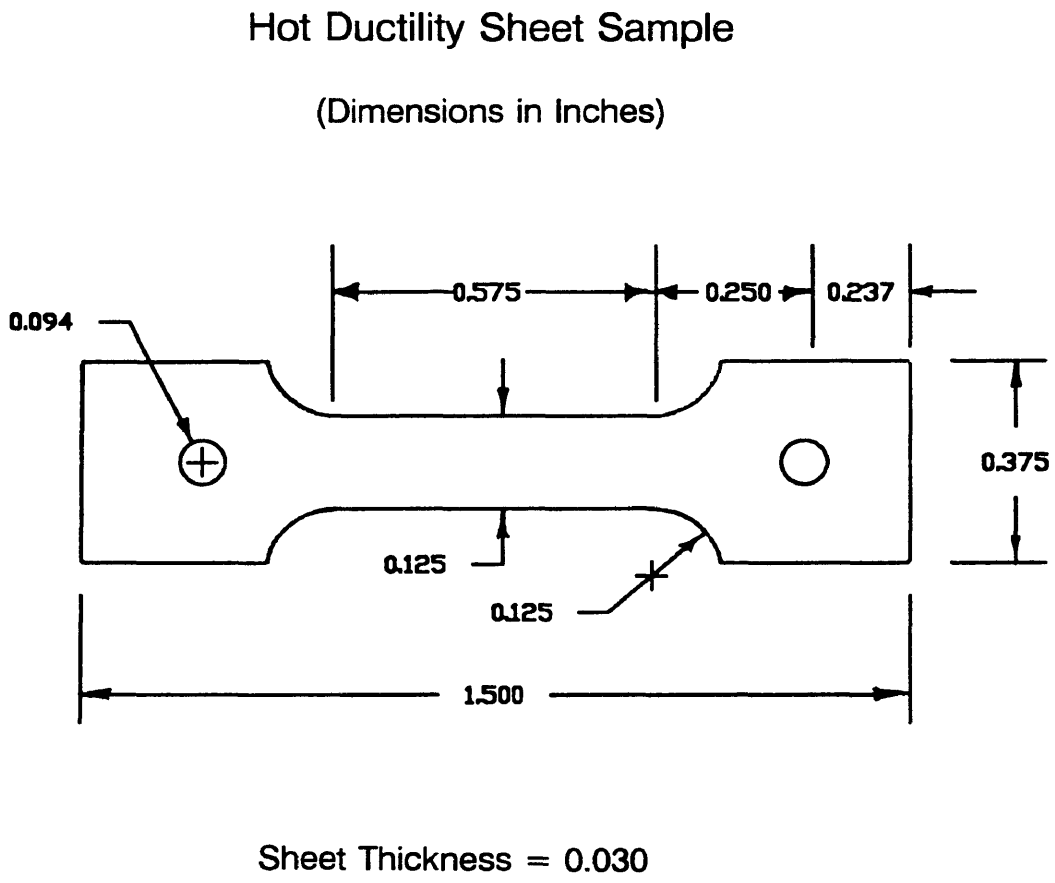

Figure 2.1 Hot ductility sheet specimen geometry. Modified from Maguire (1).

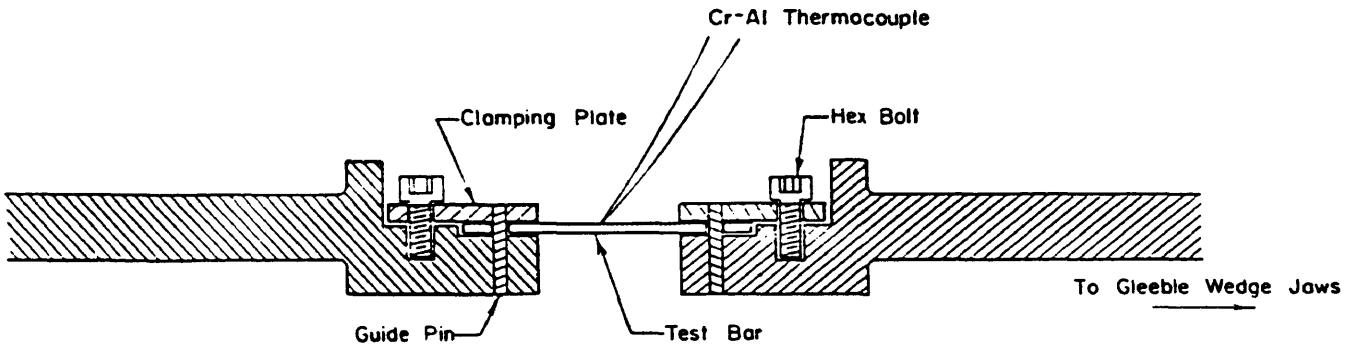

Figure 2.2 304 stainless steel hot ductility grips used for testing sheet specimens. From Maguire (1).

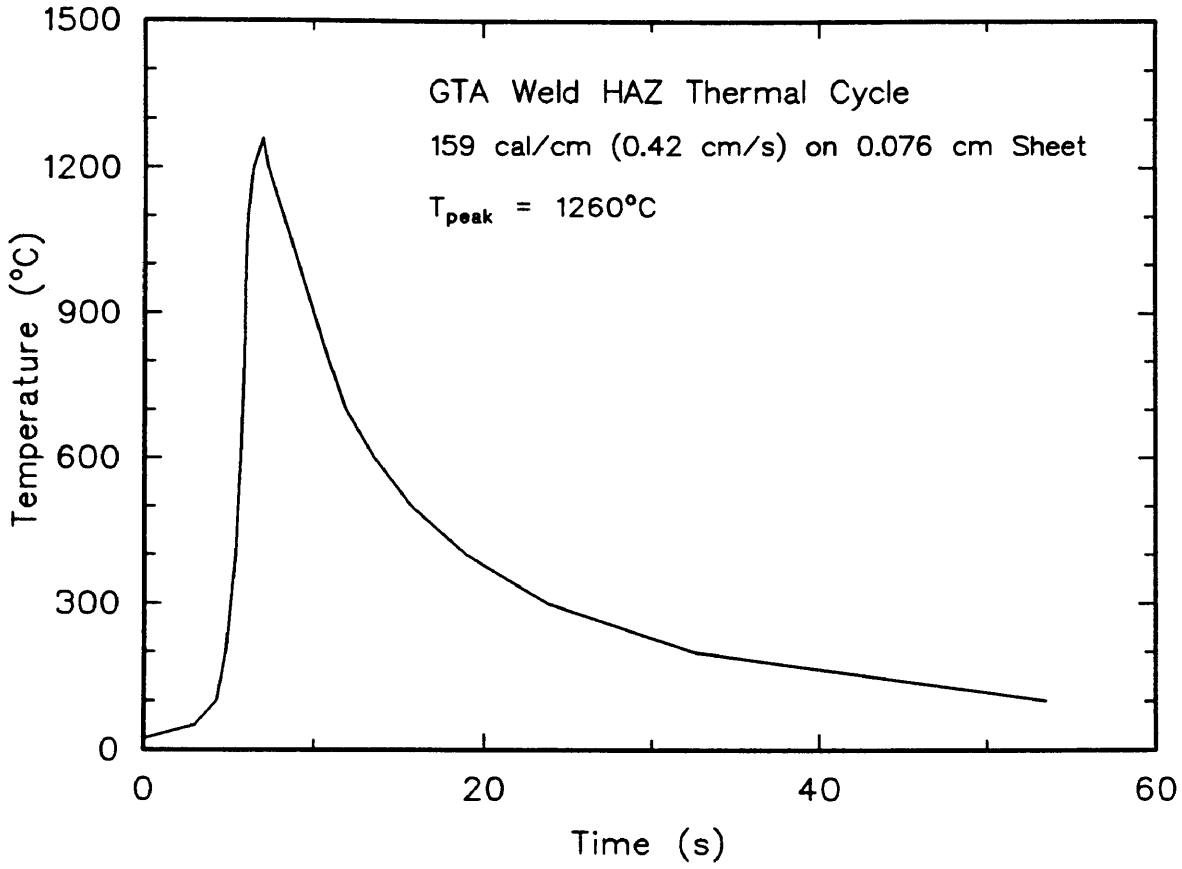

Figure 2.3 HAZ thermal cycle for 0.42 cm/s GTA weld on 0.76 mm iron aluminide sheet. After David, et al (3).

concentration were listed as: CO, CO_2, N_2, Ar, Ne,and Kr.

2.3.2 Cooling Rate Tests on Round Tensile Specimens

Different GTA weld heat inputs were simulated on the Gleeble 1500 using thermal cycles developed using a number of different calculations. Information from the weld heat input such as cooling rate were important in developing these thermal cycles. Additionally, some material properties were estimated to complete the development. The techniques used are discussed below.

2.3.2.1 Cooling Rate Estimation. To determine the effect of cooling rate on material properties, cooling rates were calculated from the two-dimensional Rosenthal equation:

$$\frac{dT}{dt} = \frac{2\,\pi\,\Gamma\,\rho\,C_p\,h^2\,(T - T_o)^2}{\eta^2\,H_w^2} \qquad (2.1)$$

where:

dT/dt = Two Dimensional Cooling Rate (deg. K/s)
Γ = Thermal Conductivity (W/cm-K)
ρ = Material Density (g/cm^3)
C_p = Heat Capacity (cal/mole-K)
d= Sheet Thickness (cm)
T = Temperature which will define cooling rate (K)
T_o = Preheat Temperature (K)
η = GTA Welding Efficiency
H_w = Weld Heat Input (cal/cm)

Before utilizing this equation, material properties such as

thermal conductivity and heat capacity were estimated. These estimated properties were calculated as follows.

2.3.2.2 Thermal Conductivity Estimation. Thermal conductivity was estimated using resistivity data versus temperature from Claudette McKamey of ORNL (53). The resistivity data was converted to thermal conductivity data by use of the Wiedmann-Franz Law (54):

$$\Gamma = \frac{L\,T}{\beta} + p_c \qquad (2.2)$$

where:

Γ = Thermal Conductivity (W/cm-K)
L = Lorenz Number = 2.45×10^{-8} W-Ω/K^2
T = Temperature (K)
β = Electrical Resistivity (Ω-cm)
p_c = Phonon Thermal Conductivity (W/cm-K)

This technique was used by Santella and coworkers (54) for converting resistivity data of Ni_3Al alloys to thermal conductivity data. It is also noted that the estimated thermal conductivity values for FA-129 were not corrected for phonon thermal conduction. Thermal conductivity values were generated (Table A-1) and were plotted in Fig. 2.4.

2.3.2.3 Heat Capacity Estimation. Heat capacity was estimated for the binary alloy $Fe_{72}Al_{28}$ using the Neumann-Kopp rule to calculate the composition-weighted sum of the

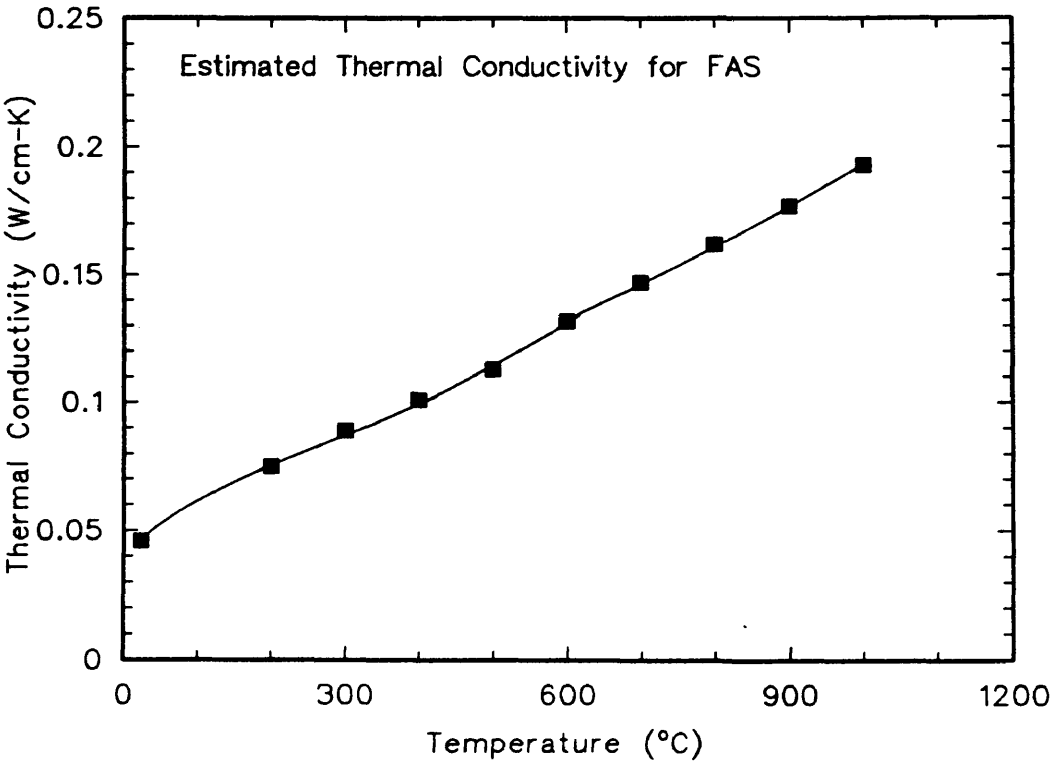

Figure 2.4 Calculated thermal conductivity data for FAS (28 Al, 2 Cr, 0.05 B, Bal. Fe) versus temperature. Reprinted by permission from C.G. McKamey (53).

heat capacities for both iron and aluminum (54, 55):

$$xC_p(Fe) + yC_p(Al) = C_p(Fe_xAl_y) \qquad (2.3)$$

Where x = 72 and y = 28 for $Fe_{72}Al_{28}$. This gives reasonable estimates of heat capacity data for compounds up to 1200 K. The heat capacity data were generated (Table A-2), and are shown in Fig. 2.5.

2.3.2.4 Thermal Cycle Development. When values for all material properties, including density of $Fe_{72}Al_{28}$ (6.5 g/cm^3, Ref. 10), and welding parameters were gathered, the efficiency of the GTA welding process, η, was calculated from the thermal cycle provided by ORNL (Fig. 2.3) and rearranging equation 2.1. The cooling rate between 1000 and 700°C was chosen since it was nearly linear in this temperature range. The efficiency was calculated to be 0.48, typical of the GTA welding process.

Once the above were accomplished, the cooling rates for different welding speeds (3, 4) were calculated using equation 2.1.

Table 2.2 lists these values which were the basis of the cooling rate tests. Thus, the test matrix for the round tensile bar hot ductility tests would consist of 100°C/s, 400°C/s, and 900°C/s cooling rate tests.

Once cooling rates were established for the different

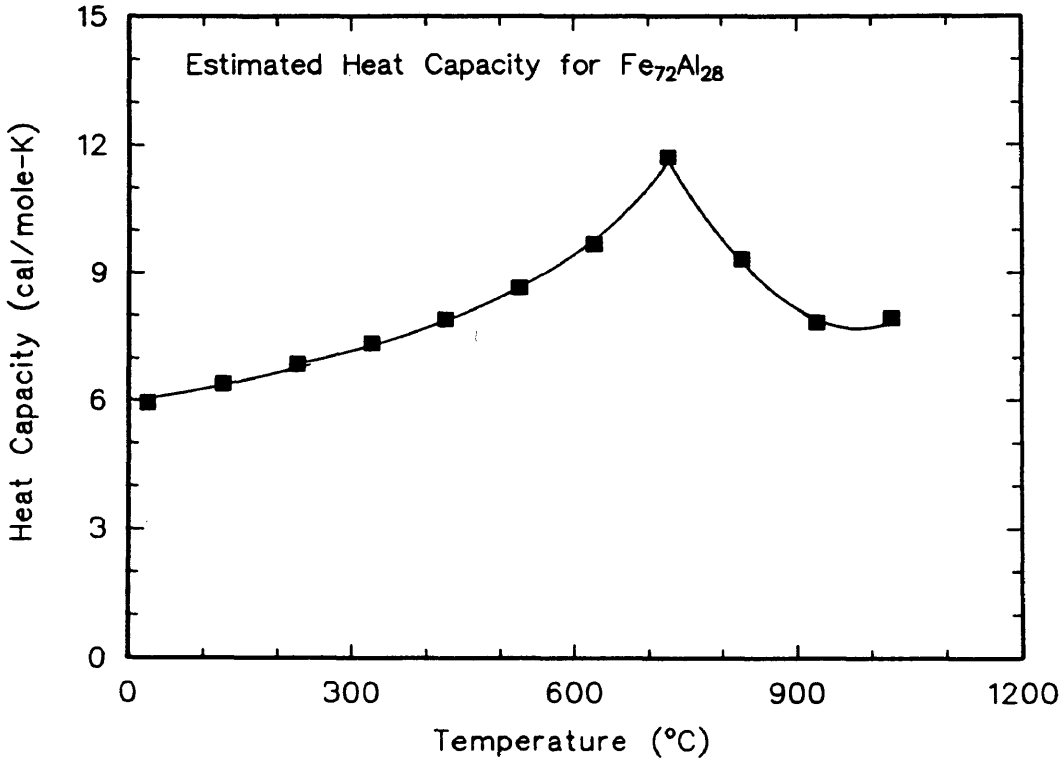

Figure 2.5 Calculated heat capacity data versus temperature. Technique from Kubachewski and Alcock (55).

Table 2.2 Calculated Cooling Rates
GTA Welds on 0.76 mm Sheet

Welding Speed cm/s (in./min.)	Heat Input cal/cm	$\left(\frac{dT}{dt}\right)_{1000\text{-}700^\circ C}$ °C/s
0.42 (10)	159	100
0.85 (20)	78.7	400
1.27 (30)	52.7	900

heat inputs, a Lotus 123 spreadsheet program was used to develop logarithmic cooling curves. Based on the original thermal cycle, a linear temperature range (ΔT) was defined between 1000°C and 700°C, and had a certain time change (Δt), corresponding to a desired cooling rate. The rest of the cooling curve could be developed, based on peak temperature, 1250°C, ΔT, and Δt. Time and temperature increments were calculated and used in the Gleeble programs.

Heating rates were based on the original thermal cycle, Fig. 2.3. For the 100°C/s cooling rate thermal cycle, the original heating portion of the thermal cycle was used. For the higher cooling rates (400 and 900°C/s), a heating rate which was twice as fast was used to model the effects of a faster-moving welding torch. These simulated thermal cycles were programmed into the computer control of the Gleeble, and imposed on round tensile bars.

2.3.2.5 Round Tensile Bar Development. Round, threaded tensile bars were used for the cooling rate tests. This design had a decisive advantage over sheet specimens in that higher loads and more accurate ductility data could be obtained. The only disadvantage was that direct, helium gas quenching on the surface of the specimen was necessary to achieve all calculated cooling rates. The sub-sized Gleeble test specimens were machined by IHLY Industries of Englewood Colorado. Since machining data on iron aluminides were scarce, and any attempts to saw or use cutting tools to machine the material were futile, grinding was the only possible means of machining the tensile bars.

Before machining the threads and reduced section, ground FA-129 round blanks were stress relieved by heating in a furnace at 10°C/min to 690°C, holding for one hour, pulled from the hot zone, and air cooled on furnace brick. Prior to testing, all tensile bars were heat treated in a box furnace containing a continuous stream of argon gas to provide a protective atmosphere and minimize any thermal cracking according to the following schedule: heat-up at 10°C/min to 845°C, held for one hour to provide recrystallization, furnace cooled to 700°C in 30 minutes, pulled from the hot zone and placed on a stainless steel sheet to cool.

For both the 100 and 400°C/s cooling rate tests, the specimen geometry is shown in Fig. 2.6. The design is similar to that used for nickel aluminides (1), but with a longer span.

For the 900°C/s cooling rate tests, the same heat treated bars were ground down to 0.069 in. diameter in the reduced section, since the 0.097 in. diameter bars could not attain this high cooling rate. After being ground down further, the specimens were subsequently stress relieved in an argon atmosphere at 693°C for one hour, pulled from the furnace hot zone, and cooled on a stainless steel sheet.

2.3.2.6 Inert Atmosphere Testing. Tensile specimens were threaded into each grip, placed within the larger copper jaws, and loaded into the Gleeble test chamber. Care was taken to insure equal half spans for each side. Failure to do so could cause improper testing conditions within the sample control zone. To perform a test, the chamber was evacuated and back-filled with argon gas twice. During testing, a steady stream of argon gas was flowing through the chamber, providing a controlled atmosphere. All Gleeble programs for the round tensile bars were designed to heat to a peak temperature of 1250°C, helium quenched to the desired test temperature for testing, and fractured in tension at an

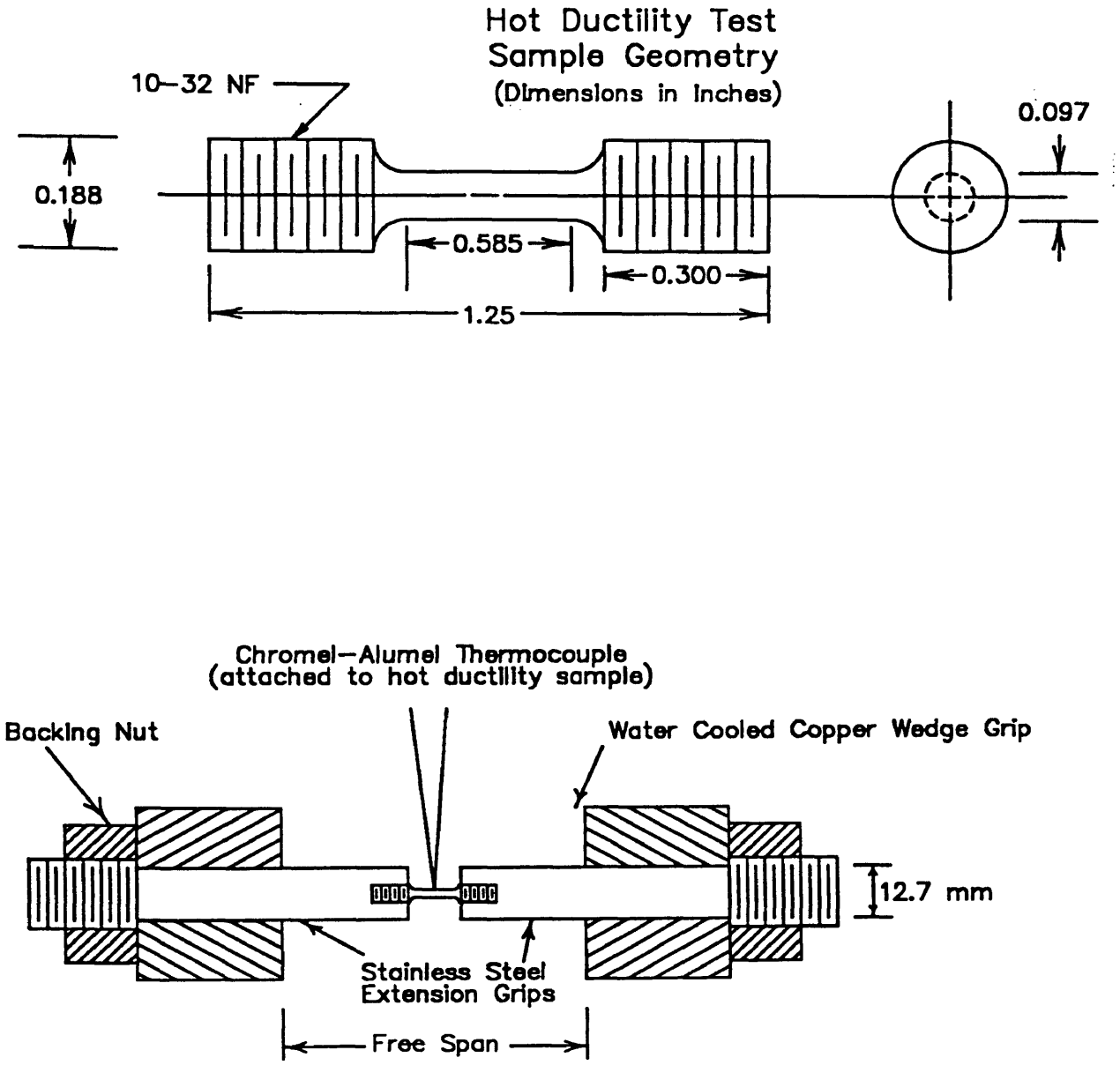

Figure 2.6 Round sample geometry for cooling rate hot ductility tests (a), and grip assembly (b). Modified from Maguire (1).

engineering strain rate of $0.08s^{-1}$. This strain rate was chosen based on the work of Santella and coworkers (54) who quantified strain rate behavior of ordered nickel aluminide alloys. This strain rate approaches values expected for nickel aluminides, since these materials are subjected to relatively high strain rates when welded.

Quenching from 1250°C was accomplished by means of a copper tube connected to the external helium quench apparatus. Once signaled in the program, the solenoid valve on the pressurized quench apparatus would open, and send a stream of helium directly onto the sample control zone. Once the specimen reached the control temperature, the helium was shut off, and the specimen was fractured. The gas pressure varied for each cooling rate: 900°C/s used 30 psi, whereas 400°C/s and 100°C/s used 20 psi.

Because a symmetric, longitudinal thermal gradient exists across the free span of a Gleeble specimen, two different approaches were utilized in testing. For temperatures 500°C and above, the stainless steel bolts and copper jaws combination were used (Fig. 2.2). From experience with FA-129 sheet specimens, round specimens tested at 300°C and 100°C were helium quenched and held at these respective temperatures using the above mentioned grip combination for two seconds, and then quenched to room

temperature. These quenched specimens were then threaded into 10 mm diameter threaded stainless steel extensions, and these placed in the 10 mm stainless steel hot jaws, with 0.6 inch span from the face of the wedge jaw to where the shoulder of the specimen met the jaw extender, Fig 2.7. These hot jaws provided for a broader temperature profile across the free span of the specimen, and reduced the chance of the specimen breaking at the shoulder where the temperature was found to be substantially lower than the control zone.

2.3.2.7 Testing in Water Vapor Environment. Testing FA-129 round tensile bars in a controlled water vapor environment required bubbling UHP helium gas through a constant humidity solution to stabilize the dewpoint in the gleeble test chamber. The solution chosen, $Mg(NO_3)_2 \cdot 6H_2O$, would provide a constant relative humidity of approximately 54% at 22°C (56) and was prepared in a Pyrex 250 ml gas bubbler shown in Fig. 2.8. The only requirement was that the solid salt be in contact with the saturated solution. After bubbling through the solution, the helium-water vapor gas mixture (He-54% RH) passed through a glass wool mist filter, and then on to the Gleeble test chamber. A Panametrics Model 2100 Hygrometer was connected to a

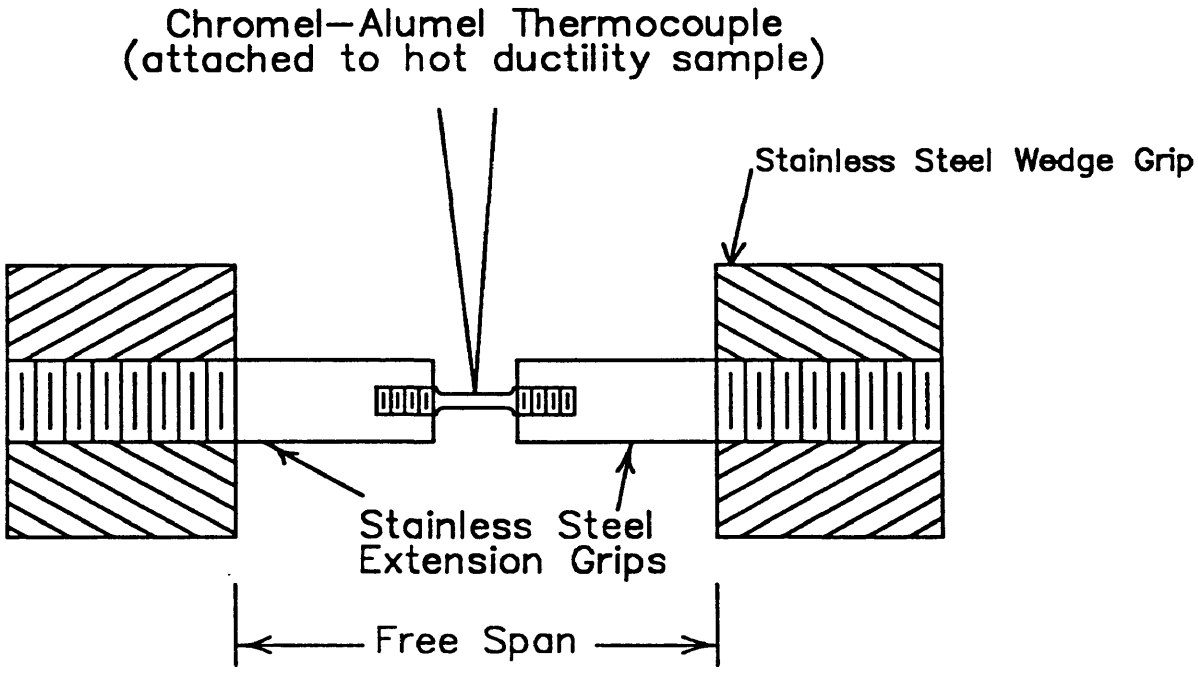

Figure 2.7 Hot grip assembly used for tests below 500°C.

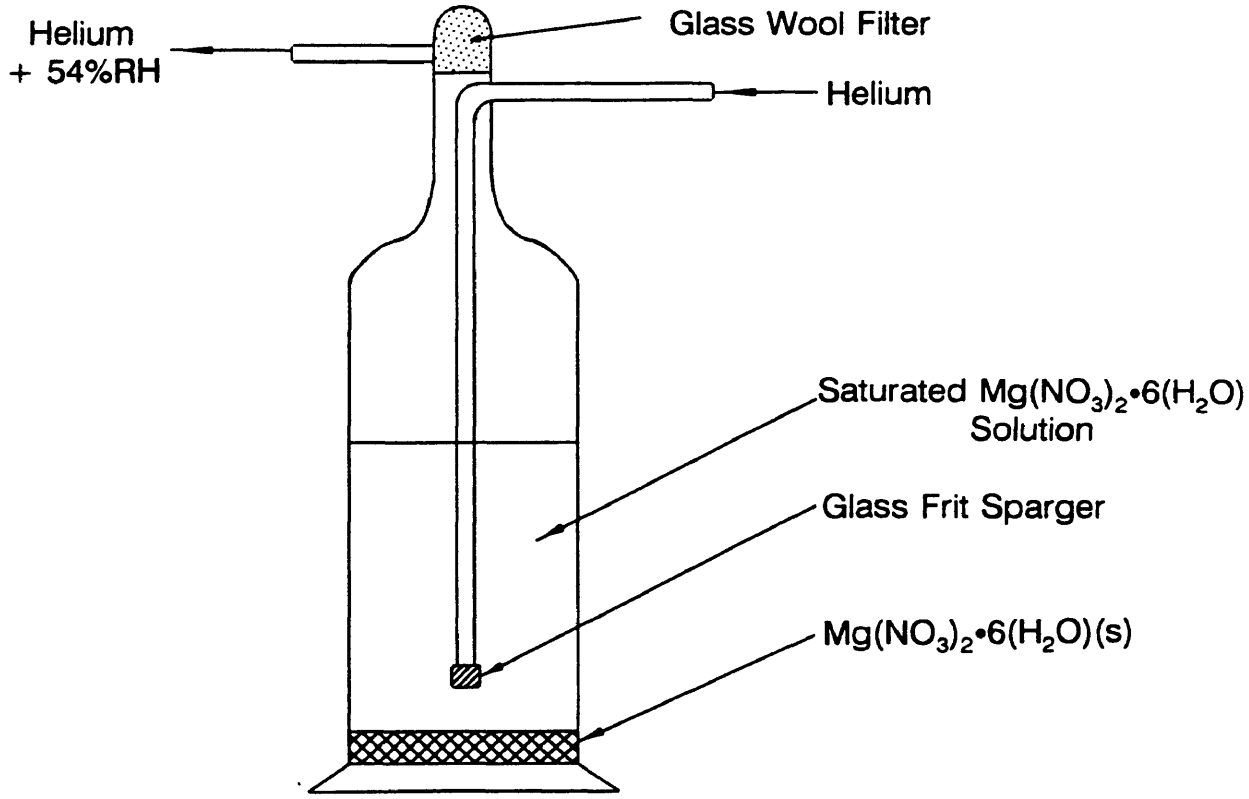

Figure 2.8 Schematic of gas bubbler with $Mg(NO_3)_2 \cdot 6H_2O$ saturated solution.

swagelock fitting which was drilled and tapped into one of the small chamber plugs. This provided for the exhaust port on the Gleeble test chamber.

The hygrometer was used to record the dewpoint of the gas stream flowing through the test chamber. A hygrometer measures the dewpoint of the gas stream by means of the output of an alumina probe, which changes impedance with the percent moisture (humidity) present. This impedance change results in an output voltage which is sensed by the hygrometer.

The dewpoint defines the temperature at which the water vapor existing in the atmosphere will become saturated. Since the constant humidity solution provides a 54% relative humidity gas stream, the vapor pressure of water present will be 54% of the saturated vapor pressure at room temperature. The dewpoint can be calculated for the constant humidity gas stream by taking 54% of the saturated water vapor pressure at room temperature (22°C), and then matching the calculated vapor pressure with it saturation temperature (dewpoint) from the steam tables. This was calculated to be 12°C. The exhaust from the test chamber was monitored with the hygrometer until the dewpoint (12°C) was reached and remained stable for 25 minutes. Once stabilized, the hot ductility tests were performed on

specimens helium-quenched to 100°C, 300°C, and 350°C. Both 100°C/s and 400°C/s cooling rates were investigated.

To perform a test, the chamber was first evacuated with the mechanical vacuum pump, and back-filled with RG helium. This was performed twice to insure adequate removal of ambient air. The dewpoint of this helium gas was measured to be -30°C. Second, UHP helium (dewpoint = -34°C) was bubbled through distilled water at room temperature in a bubbler similar to the one in Fig. 2.8, which decreased the time necessary to achieve the desired dewpoint of 12°C since the dewpoint was 22°C for any gas bubbling through the distilled water. Once a 10°C dewpoint was achieved, the helium was bubbled through the constant humidity solution, which allowed the dewpoint to increase and stabilize at 12°C for testing.

2.3.2.8 Temperature Measurements Outside of Control Zone. Since temperature gradients across the span of the specimen do occur, a method of measuring the temperature at the radius was accomplished. This was done to determine why some specimens would fail at the radius instead of the control zone when using the stainless steel hot jaws and the He-54% RH environment. In addition to the control thermocouple attached to the middle of the reduced section

(control zone), another thermocouple was percussion welded in the same manner at the radius of one end where the diameter reduced to 0.097 in., Fig. 2.9. This radius thermocouple was connected to a thermocouple plug attached to a metal support sheet on the moving jaw. An insulated, extension thermocouple was connected to this plug, passed through a chamber plug, to a Doric 450 battery powered temperature indicator.

The one advantage of using this type of temperature indicator is that it was completely isolated from the gleeble circuitry. That is, the thermocouple output will contain electronic background noise associated with the rectified AC voltage signal which is applied to the test specimen. If the thermocouple signal is not protected or isolated, a rapidly changing temperature output is observed which alternates around some mean value. This can be observed on a thermocouple display monitor which is not isolated by simply plugging it into a wall socket. Isolation circuitry or an isolation amplifier is required to eliminate this noise. Thus the battery operated indicator isolated the signal and provided a steady temperature display similar to what is observed on the Gleeble 1531 temperature servo which displays the control zone temperature.

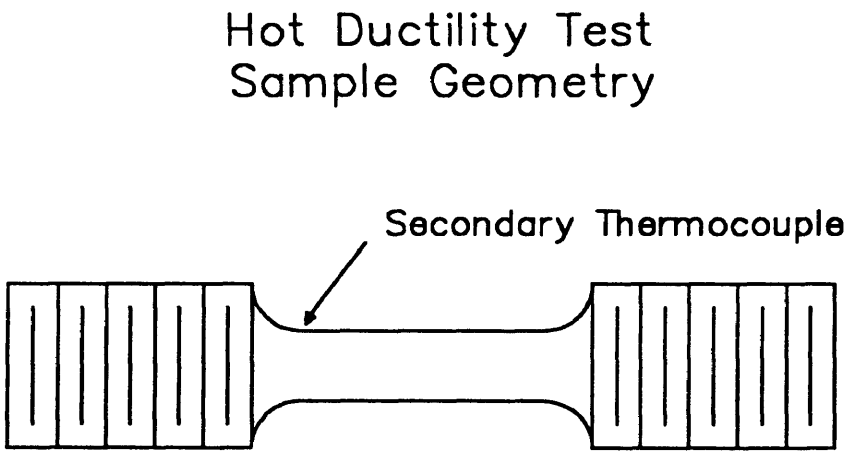

Figure 2.9 Placement of shoulder thermocouple.

2.4 Long Range Order and Ambient Temperature Properties

Sheet tensile and x-ray diffraction specimens were heat treated to produce the different superlattice structures and varying degrees of long range order. These tests were performed to determine the effects of superlattice structure and long range order on the ambient temperature material properties. Long range order parameters were calculated from x-ray diffraction data of sheet specimens heat treated in a salt pot to produce either the B2 or DO_3 superlattice structure. Increasing annealing times at 500°C were utilized to increase the DO_3 long range order parameter.

Sheet specimens were annealed at 700°C, or 500°C to develop the different superlattice structures or degrees of long range order. For each time and temperature condition, one x-ray specimen and two tensile bars were used for the long range order determination and material properties, respectively.

All specimens were initially annealed at 700°C for one hour and water quenched to create the B2 structure. Specimens were set aside for this condition. Next, the remainder of specimens were annealed at 500°C to create DO_3 long range order. DO_3 specimens were developed for the following times at 500°C: 24, 48, and 96 hours. In

addition, an extra set of specimens annealed at the 96 hour condition were subsequently annealed at 700°C for one hour. Specimens were water quenched after pulling from the molten salt bath.

A technique used by Anthony and Fultz (57), with help from Warren (58), was used to determine long range order parameters. The basis of this technique involves taking the integrated intensity ratio of the superlattice and fundamental diffraction peaks determined experimentally, and comparing it to that ratio determined by calculation (theory). Equations describing this technique which were used in analyzing the x-ray diffraction data are as follows:

$$S_{DO_3} = 0.88 \left[\left(\frac{I_{111}}{I_{220}} \right)_{exper.} / \left(\frac{I_{111}}{I_{220}} \right)_{calc.} \right] \qquad (2.4)$$

$$S_{B2} = 0.56 \left[\left(\frac{I_{100}}{I_{110}} \right)_{exper.} / \left(\frac{I_{100}}{I_{110}} \right)_{calc.} \right] \qquad (2.5)$$

The coefficients 0.88 for DO_3 and 0.56 for B2 relate to the maximum amount of long range order attainable for the specific composition (17). The coefficients, experimental data and theoretical calculations were based on using a $Fe_{72}Al_{28}$ binary alloy. For this composition, the maximum amount of long range order for either structure is calculated by the following equations (17):

$$S_{DO_3}(max) = 2\ (1 - 2x) \qquad (2.6)$$

Where x is the atomic fraction of aluminum in the alloy greater than 0.25 atomic fraction. Similarly, the B2 long range order is calculated as:

$$S_{B2}(max) = 2x \qquad (2.7)$$

To calculate the theoretical intensity ratio, the complex conjugate form factors, consisting of the real and imaginary components of the iron and aluminum atomic scattering factors, were developed for a $Fe_{72}Al_{28}$ alloy. For the DO_3 long range order parameter, both the fundamental ($F_F F_F^*$) and superlattice ($F_S F_S^*$) form factors were required:

$$F_F F_F^*(DO_3) = 256\ [(x_{Fe} f_{Fe} e^{-M_{Fe}} + x_{Al} f_{Al} e^{-M_{Al}})^2 +$$

$$(x_{Fe} \Delta_{Fe} e^{-M_{Fe}} + x_{Al} \Delta_{Al} e^{-M_{Al}})^2] \qquad (2.8)$$

$$F_S F_S^*(DO_3) = 16\ S^2[(f_{Fe} e^{-M_{Fe}} - f_{Al} e^{-M_{Al}})^2 +$$

$$+ (\Delta_{Fe} e^{-M_{Fe}} - \Delta_{Al} e^{-M_{Al}})^2] \qquad (2.9)$$

Likewise, for the B2 structure:

$$F_F F_F^*(B2) = 4\,[(x_{Fe} f_{Fe} e^{-M_{Fe}} + x_{Al} f_{Al} e^{-M_{Al}})^2 + (x_{Fe}\Delta_{Fe} e^{-M_{Fe}} + x_{Al}\Delta_{Al} e^{-M_{Al}})^2] \quad (2.10)$$

$$F_S F_S^*(B2) = S^2\,[(f_{Fe} e^{-M_{Fe}} - f_{Al} e^{-M_{Al}})^2 + (\Delta_{Fe} e^{-M_{Fe}} - \Delta_{Al} e^{-M_{Al}})^2 \quad (2.11)$$

X-ray analyses were performed on a Rigaku system in the Physics Department at CSM using Cu Kα radiation. The radiation detector counter rotated through 2θ while the specimen remained stationary. Sheet x-ray specimens were attached to a glass slide by means of double sided tape. These specimens were aligned so that the x-ray beam and rolling direction were nearly parallel. Also, this provided for maximum interaction since the specimens were oblong shaped with the longest dimension in the rolling direction. Fundamental and superlattice peaks were recorded by means of a computer acquisition program. Peak finding, peak height, area beneath diffraction peaks, and $K\alpha_2$ stripping were determined or performed to isolate the diffraction peaks. Once the areas beneath the diffraction peaks were obtained, the technique developed by Warren was performed to determine

the long range order parameter for each condition. No attempt was made to exclude preferred orientation effects of the sheet material.

Ambient temperature material properties were determined by tensile tests on an Instron machine, operated on time drive at a crosshead velocity of 0.05 in./min. This gave an engineering strain rate of $5x10^{-3}s^{-1}$. Ductility was measured as percent elongation of the reduced section of the sheet specimens. Yield and fracture strengths were determined by taking the load at 0.2 % offset and at fracture, respectively.

3. RESULTS AND DISCUSSION

This section presents the results of this investigation. This study emphasized the effects of grain size, cooling rate, and environment on the hot ductility of alloy FA-129.

3.1 Hot Ductility of FA-129 Sheet Material

The results of hot ductility testing on sheet material are presented in this section. Sheet specimens were utilized first because they were readily available and minimized use of material.

3.1.1 Stress Relieved FA-129

The first hot ductility tests were performed on specimens punched from FA-129 sheet which was stress relieved at 750°C for one hour followed by oil quenching. This treatment was not intended to give a recrystallized microstructure. However, the microstructure did recrystallize, with an initial grain size of 30μm, Fig. 3.1. These specimens were tested either on the heating portion or the cooling portion of the thermal cycle in Fig 2.3. The hot ductility results are presented in Fig 3.2. As was observed, the hot ductility of the material depended upon

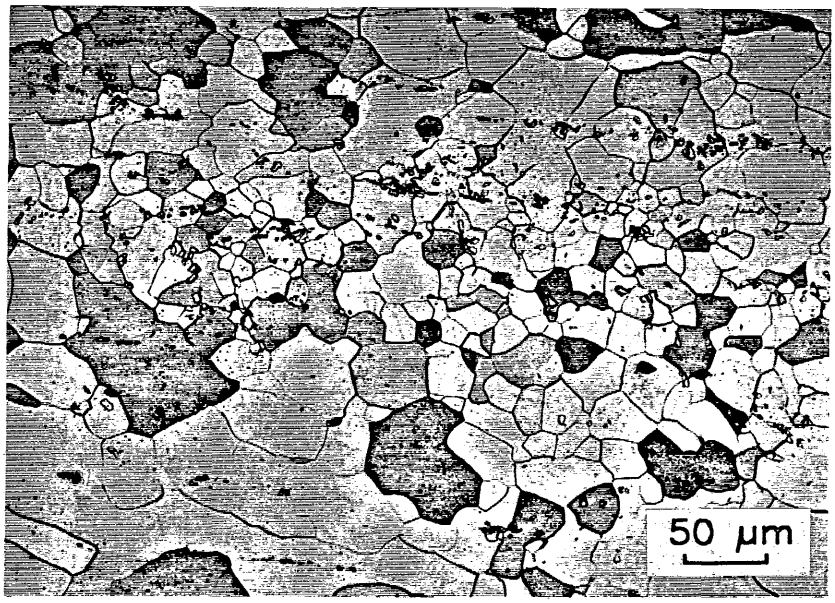

Figure 3.1 Microstructure of FA-129 stress relieved at 750°C and oil quenched. Average grain size = 30μm.

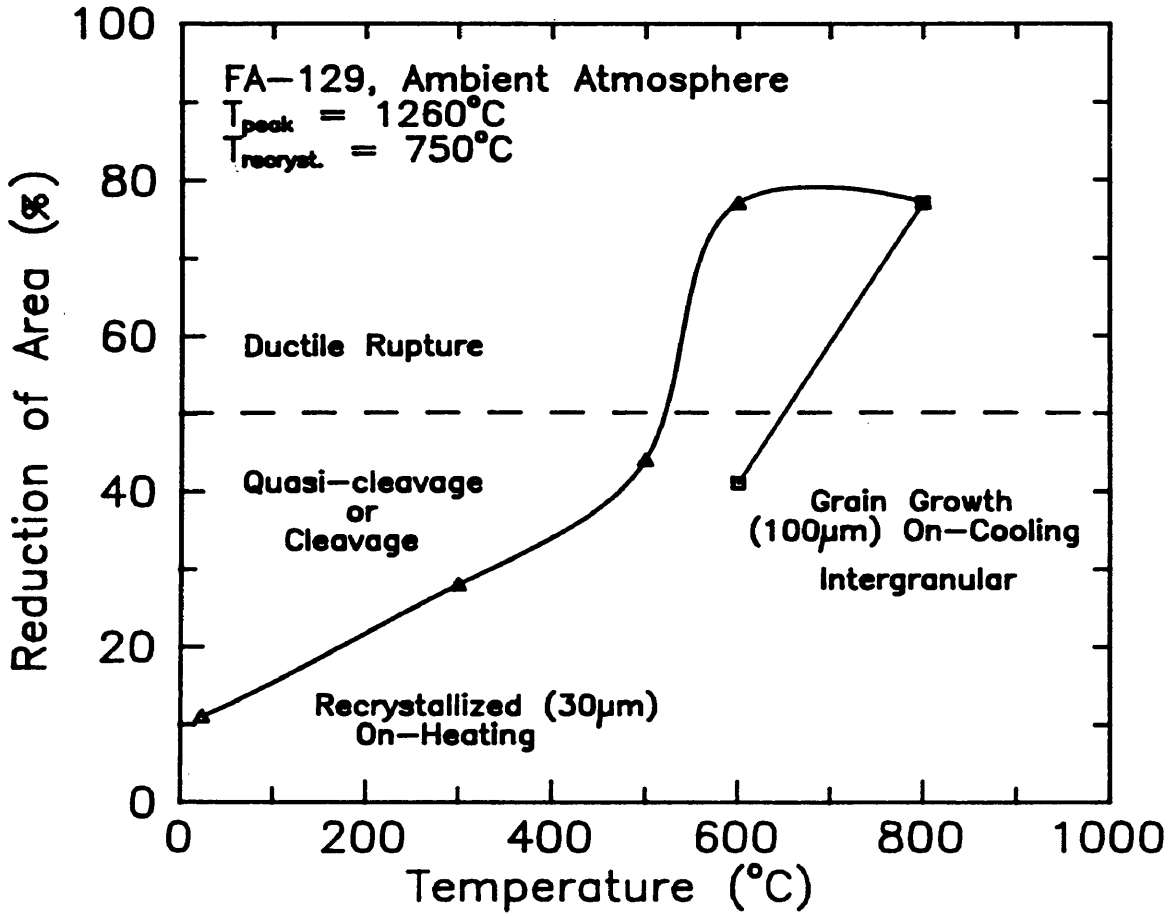

Figure 3.2 Hot ductility results for sheet specimens initially stress relived (750°C) and subjected to 4.2 mm/s weld thermal cycle.

whether the specimen was tested during the heating portion or the cooling portion of the thermal cycle. The significant ductility drop at 600°C upon cooling from the peak temperature indicated important microstructural changes occurred during the thermal cycle. Fractographic results of these 600°C tests are presented in Fig. 3.3 a) on-heating and b) on-cooling, respectively. It was observed that significant grain growth occurred in the on-cooling specimen when compared to the on-heating specimen. After observing the fracture surface, it was apparent that the grain size grew to approximately 100μm. Additionally, the fracture behavior changed from mostly ductile rupture (on-heating) to mixed ductile rupture with deep intergranular pull-out. It can be concluded that this grain growth was responsible for the change in fracture behavior and drop in ductility.

The next hot ductility tests were performed on specimens which were stress relieved at 690°C. This heat treatment yielded a partially recrystallized microstructure, Fig. 3.4. These specimens were tested in a similar way to those described above, except for the atmosphere which was 99.9999% helium. The hot ductility data are shown in Fig. 3.5. The hot ductility trend was similar to the behavior observed in Fig. 3.2. Fractography, however, that indicated a significant change in fracture behavior occurred at 500°C,

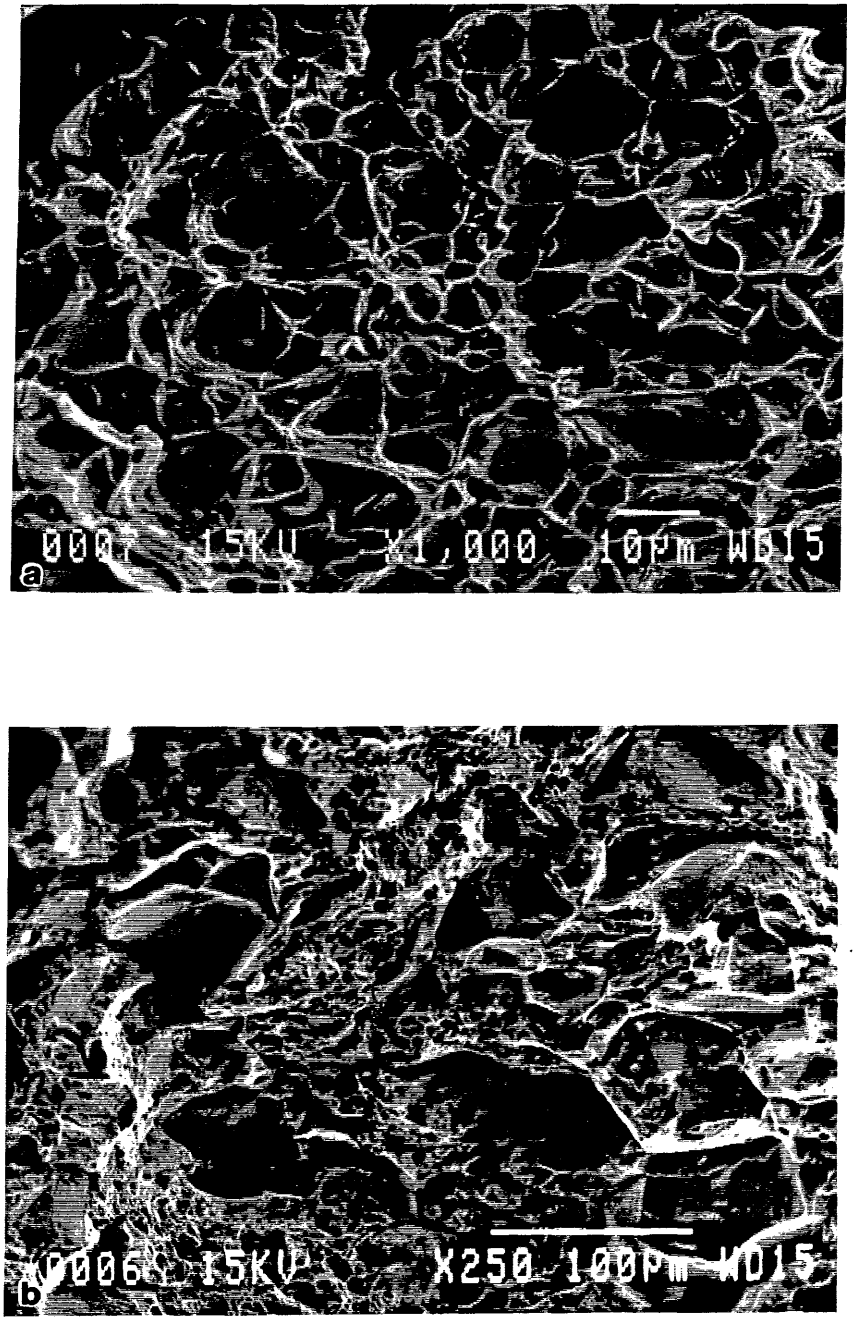

Figure 3.3 Fracture surfaces of hot ductility specimens tested at 600°C; a) on-heating, showing ductile rupture, and b) on-cooling, showing mixed ductile rupture and intergranular pull-out.

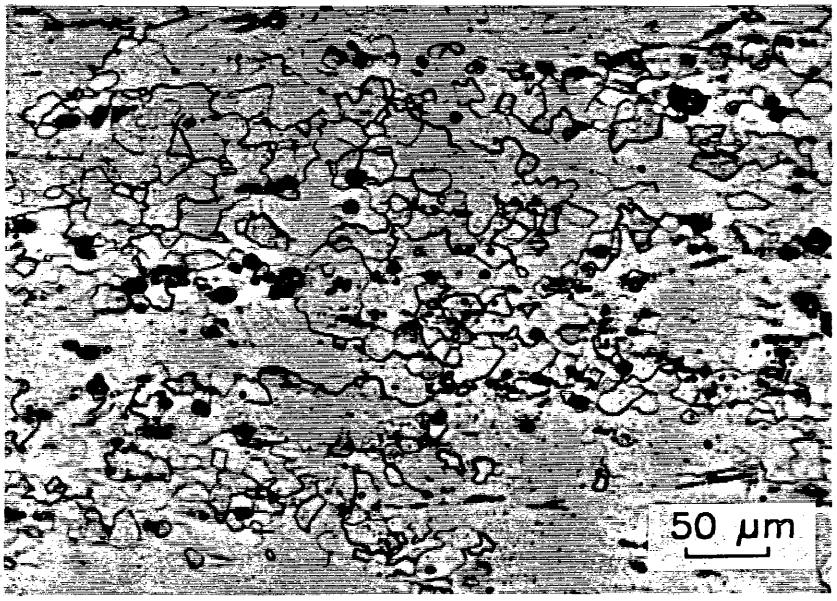

Figure 3.4 Partially recrystallized microstructure of FA-129, stress relieved at 690°C and water quenched.

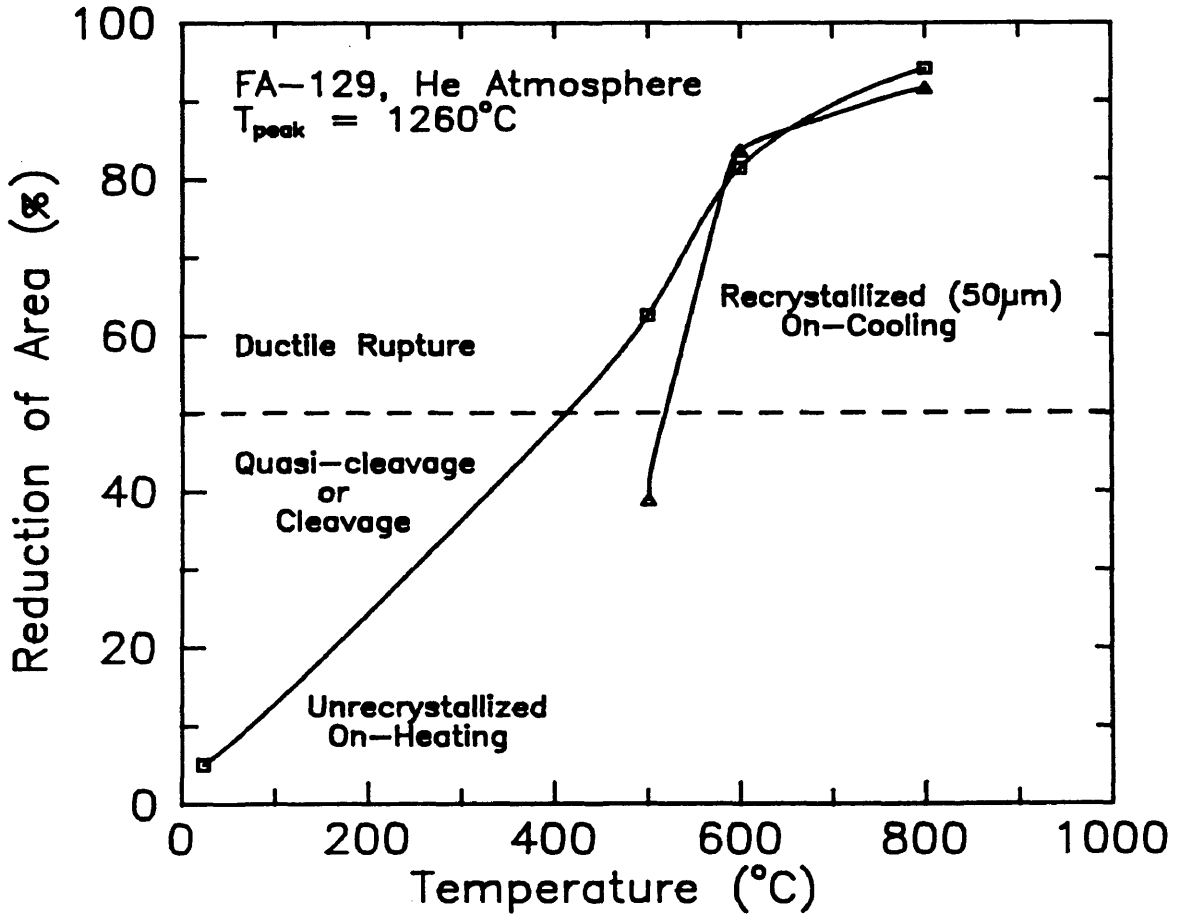

Figure 3.5 Hot ductility results for sheet specimens initially stress relieved (690°C) and subjected to 4.2 mm/s GTA weld thermal cycle.

as seen in Fig. 3.6. The grains grew to approximately 50 μm during the thermal cycle. Fracture behavior changed from ductile rupture to mostly quasi-cleavage. This was further indication that grain growth was responsible for the change in fracture behavior.

3.1.2 Recrystallized FA-129

The third set of hot ductility tests on sheet material was performed in helium on FA-129 tensile specimens recrystallized at 850°C for one hour and water quenched. This heat treatment resulted in a grain size of 26μm, Fig. 3.7. The hot ductility results of these tests are shown in Fig. 3.8. Compared to the other hot ductility tests, the behavior was similar. Once again, grain growth proceeded to approximately 70μm, which resulted in a change in fracture behavior at 500°C. This grain growth resulted in quasi-cleavage fracture upon cooling from the peak temperature, Fig. 3.9.

3.1.3 Effects of Thermal Cycle on Grain Size

In reviewing the hot ductility data, the most significant finding was that grain growth occurred for specimens which experienced the peak temperature (1260°C)

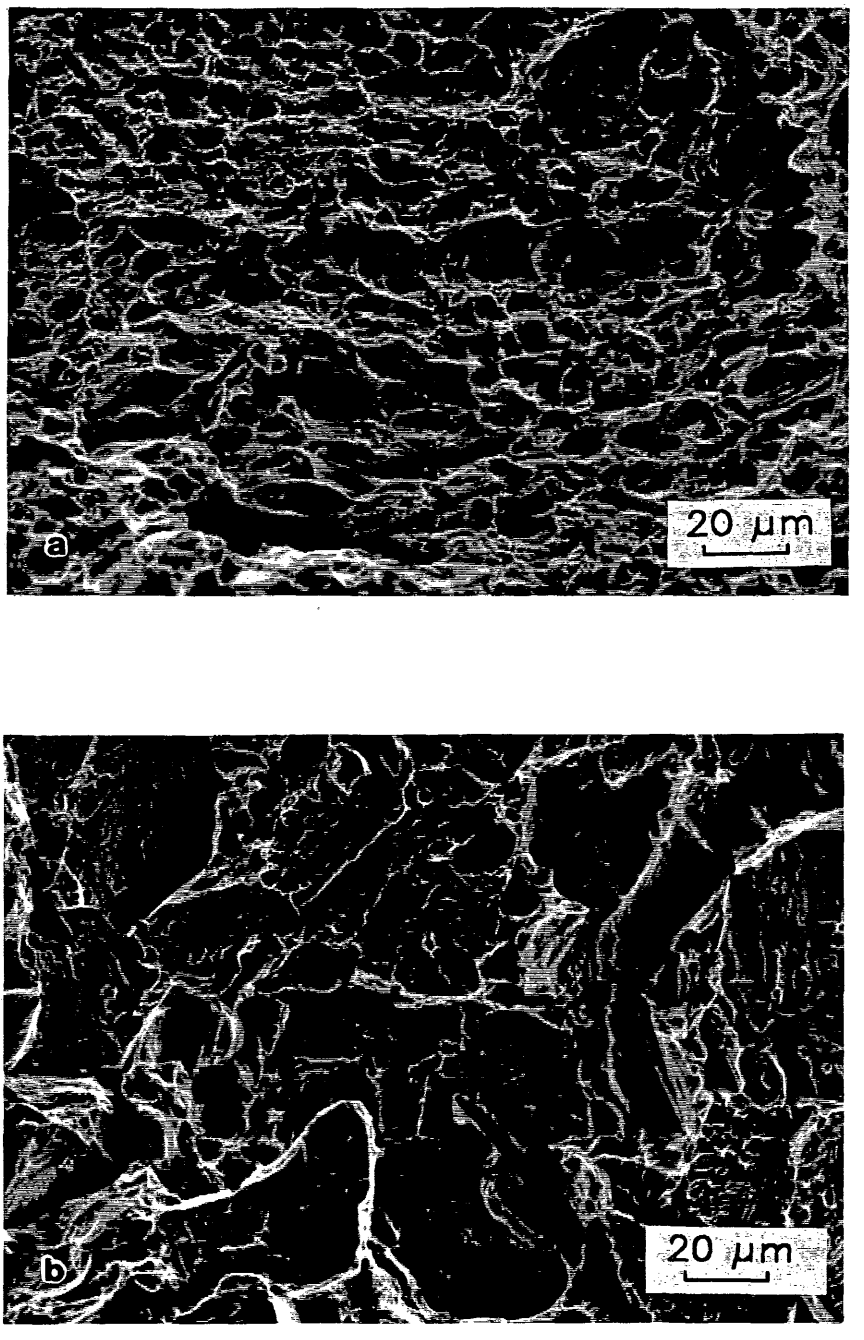

Figure 3.6 Fracture surfaces of hot ductility specimens tested at 500°C; a) on-heating, showing ductile rupture, and b) on-cooling, showing mainly quasi-cleavage.

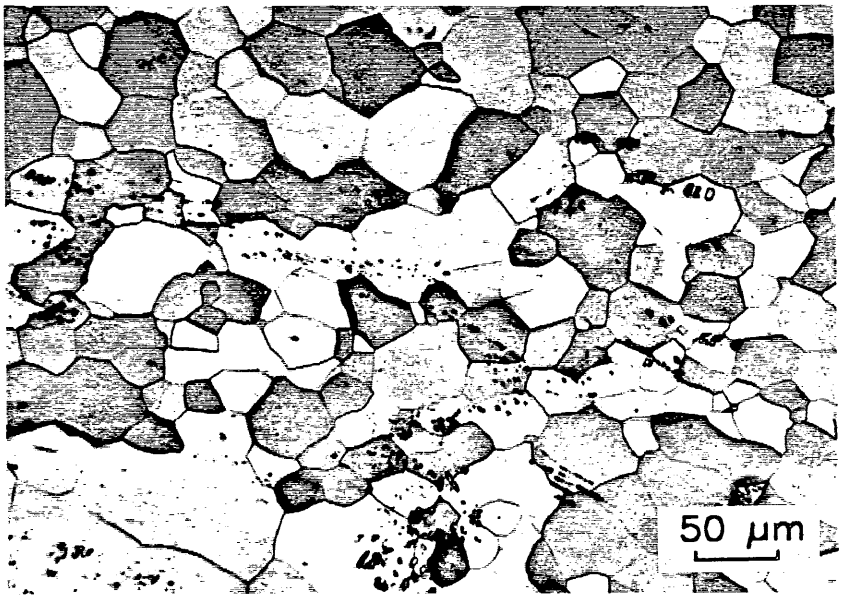

Figure 3.7 Recrystallized (845°C) microstructure of FA-129. Average grain size = 26μm.

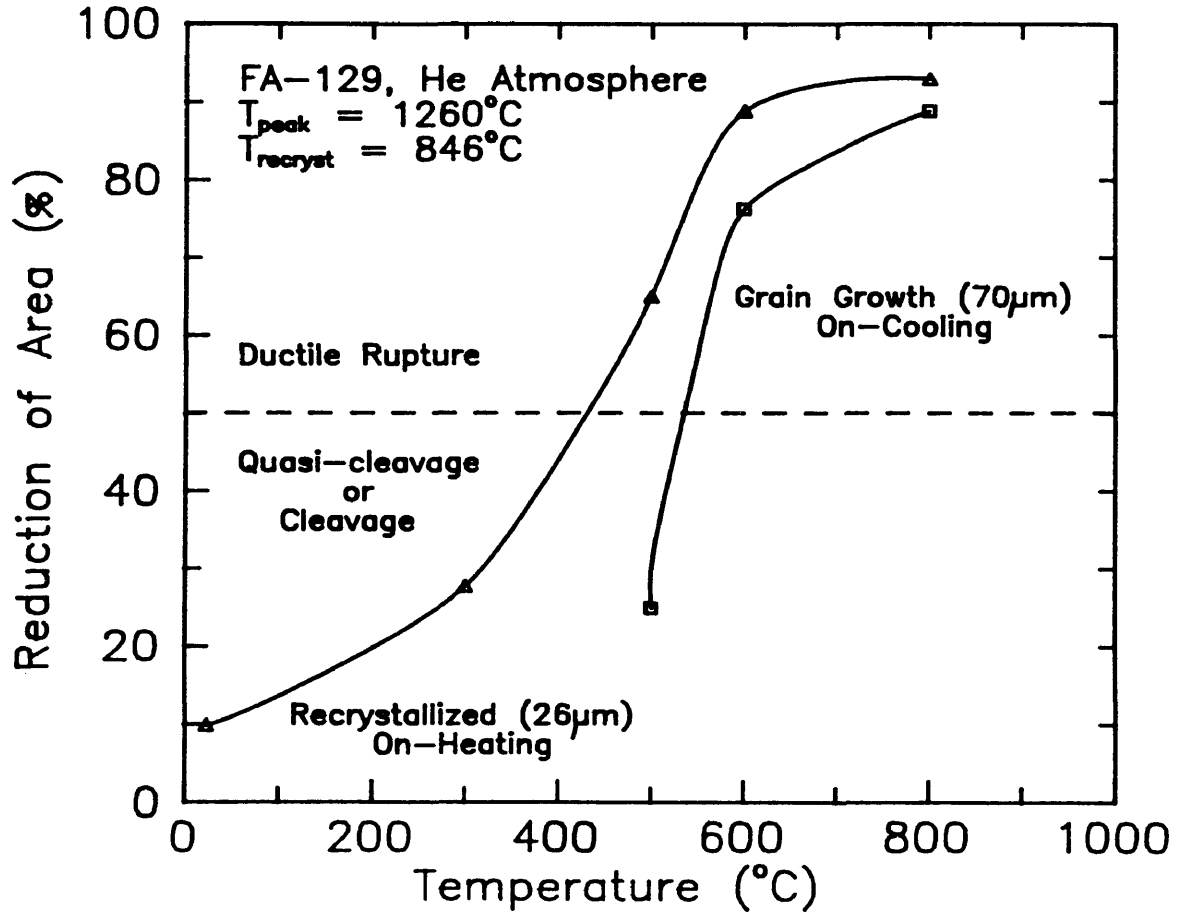

Figure 3.8 Hot ductility results for recrystallized FA-129 and tested in RG helium environment.

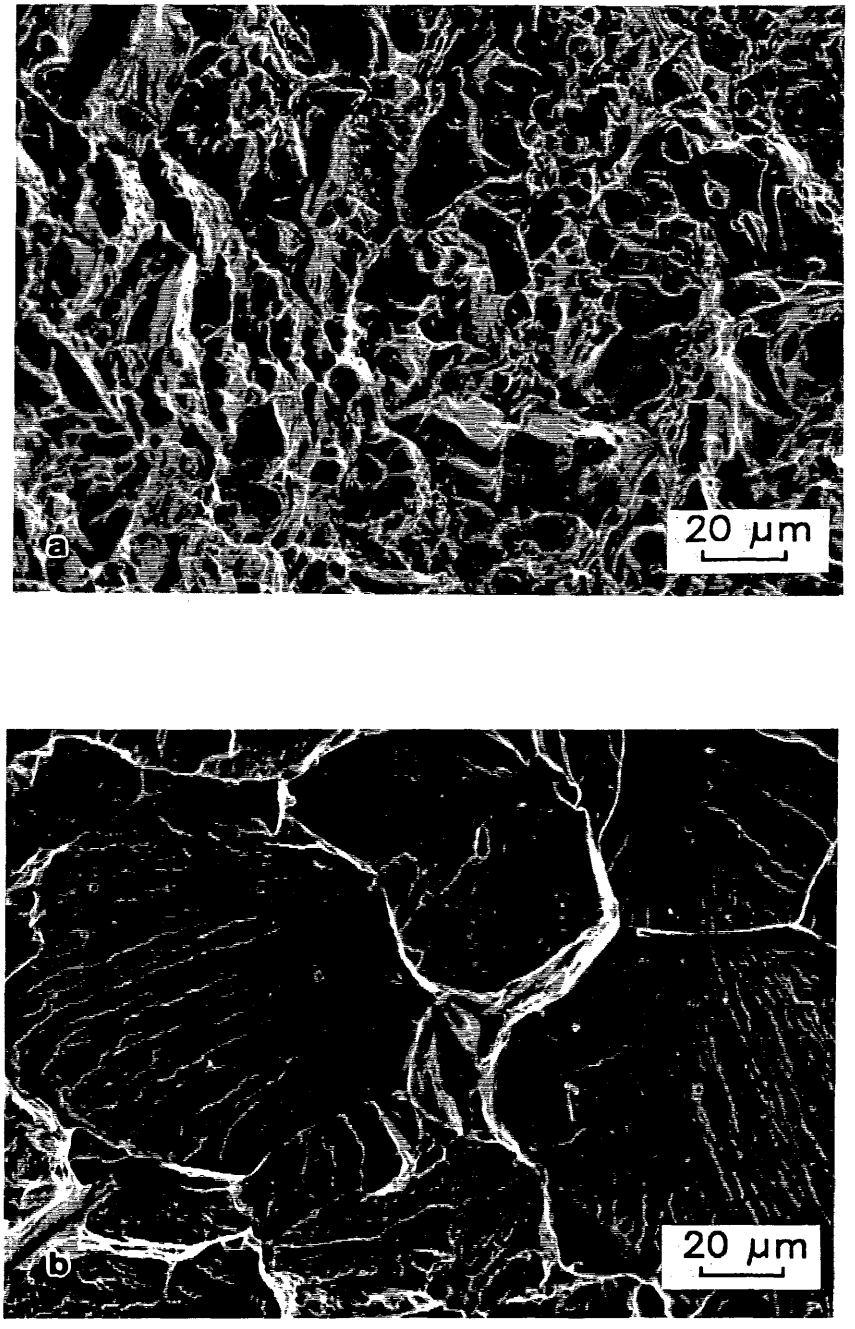

Figure 3.9 Fracture surfaces of hot ductility specimens tests at 500°C; a) on-heating, showing mainly ductile rupture, and b) on-cooling showing mainly quasi-cleavage.

and were then tested on the cooling portion of the thermal cycle. For all hot ductility tests performed with sheet specimens, it was apparent that an approximate three-fold increase in the grain size occurred for specimens tested in this manner. This indicates that the microstructure of FA-129 is unstable with respect to a weld thermal cycle, and that grain growth will occur, regardless of whether the material is partially or fully recrystallized. Thus, since hot ductility and fracture mode of FA-129 are very sensitive to grain size, so will be the weld cracking susceptibility.

3.1.4 Combined Effects of Processing and Thermal Cycle

It is apparent that processing prior to subjecting the iron aluminide FA-129 to a weld thermal cycle may play an important role in the weld cracking behavior. Since the thermal cycle effectively induces grain growth, processing to limit this grain growth for improved ductility will be ineffective. Since the stress relieved material was observed to be unstable with respect to the thermal cycle, a recrystallization anneal was performed. This was utilized in an attempt to stabilize the microstructure. However, these recrystallized grains did grow during the thermal cycle. This indicated that niobium carbide (NbC)

precipitation in FA-129 did not occur to limit grain growth. TiB_2 particles, although beneficial in limiting grain growth, increase the hot cracking susceptibility of iron aluminides during welding (3, 10).

3.1.5 Fracture Behavior with Temperature

In accordance with grain growth, the fracture behavior changed upon cooling from the peak temperature. This resulted in: 1) a change from ductile rupture on-heating to mixed ductile rupture and intergranular fracture on-cooling at 600°C, and 2) a change from ductile rupture on-heating to mostly quasi-cleavage on-cooling at 500°C. For a grain size of 100μm at 600°C, the grain size is basically too coarse to be effective in dispersing slip in the partially ordered B2 structure. The intergranular behavior is indicative of planar slip within the grains. However, for a grain size of 70μm at 500°C, the grain size is fine enough to inhibit planar slip and intergranular fracture. Since quasi-cleavage is observed, it is an indication that duplex slip is controlling within the DO_3 superlattice structure. If slip is operating on two intersecting {110} planes, Fig. 3.10, dislocations which coalesce into ⟨100⟩ dislocations and pile-up at the intersection (a {100}-type plane) will nucleate cleavage cracks. Thus after successive pile-ups,

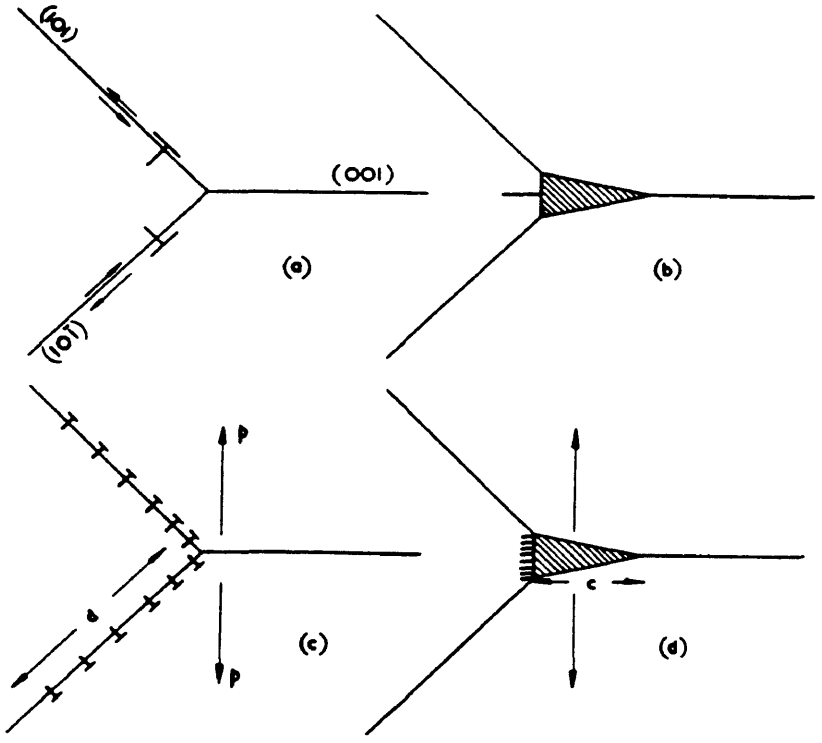

Figure 3.10 Dislocation coalescence model for ⟨111⟩{110} dislocations intersecting on {100} planes and reacting to form ⟨100⟩ immobile dislocations in bcc iron. From Cottrell (59).

the crack can propagate with stress until fracture is complete.

The basic nature of the intergranular fracture (600°C) and cleavage fractures (500°C) at particular grain sizes indicate the preference for slip on certain planes and the lack of slip dispersal. That is, planar slip occurred and caused intergranular fracture, whereas duplex slip occurred, and caused cleavage fracture. Indications of slip dispersal, ie. ductile microvoid coalescence, were evident for grain sizes below 30μm, Fig. 3.5. Thus, further slip dispersal is necessary for grain sizes greater than about 30μm.

For temperatures below 500°C, no hot ductility data were generated for the on-cooling sheet specimens, since the specimens fractured close to the grips, and away from the control zone.

With the results of the screening hot ductility tests, it has been shown that the hot ductility of FA-129 is very sensitive to grain size. These findings are similar to the results of Schulson et al (60) for B2-ordered NiAl tensile tests at 400°C, Fig. 3.11. The ductility of FA-129 at 500°C was plotted similarly, for the on-heating tests and on-cooling tests, Fig. 3.12, using approximate grain sizes for the on-cooling specimens. Even though transgranular

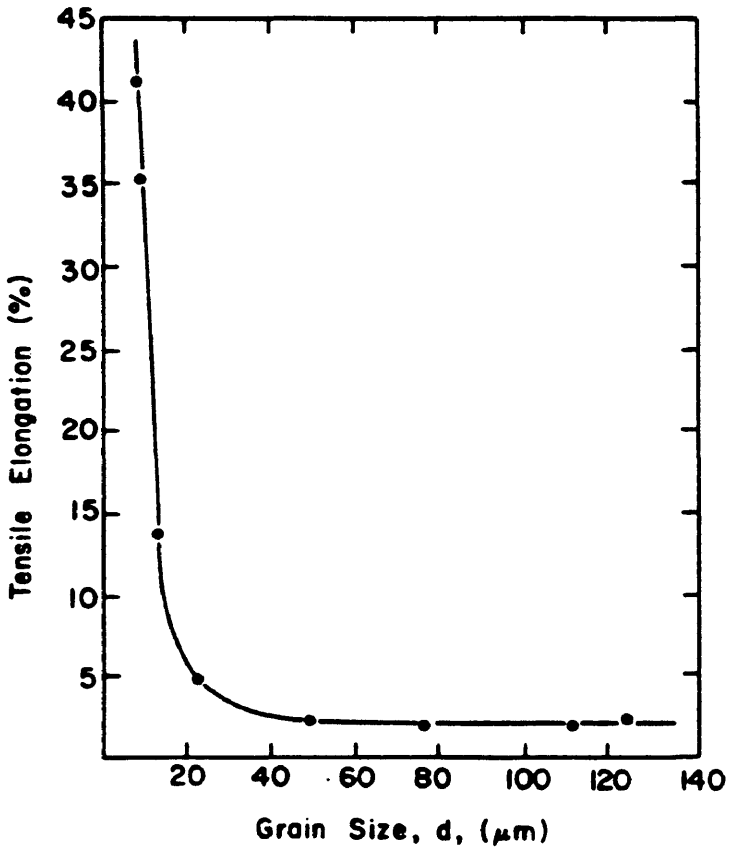

Figure 3.11 Ductility versus grain size for B2-NiAl tested at 400°C. From Schulson and coworkers (60).

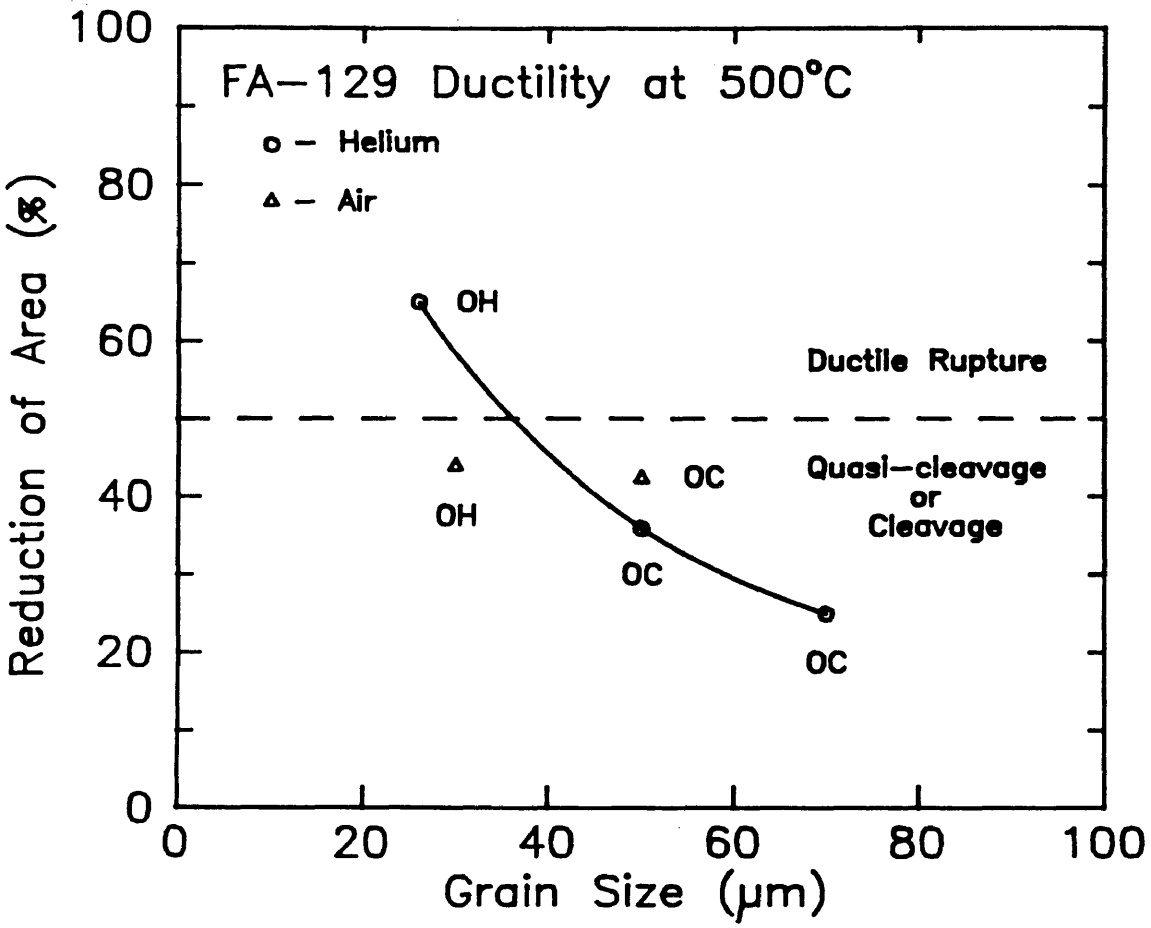

Figure 3.12 Ductility versus grain size for FA-129 tested on-heating or on-cooling at 500°C.

cleavage was observed on-cooling at 500°C, the material still showed significant ductility, in accordance with the results of Schulson. Schulson explained that a brittle material could exhibit "ductile" behavior (high percentage elongation) when the grain size was fine enough, Fig 3.11, even though the material failed in a brittle manner (cleavage). Thus, FA-129 with a grain size of 50μm does experience considerable plasticity before fracture; however,the pile-up of dislocations, possibly on the {110} slip planes, nucleated cleavage cracks on {100} planes. The material eventually failed in a more brittle fashion.

To alleviate dislocation slip concentration on {110} slip planes, or initiate other slip systems (ie., {112} or {321} slip planes) to enhance slip dispersal, barriers to dislocation motion must be implemented to refine the slip path length. Since no data exist on carbide precipitation for FA-129, plus the fact that no other solid state phase transformations occur besides order-disorder, the one possible means was to investigate antiphase domain structures.

3.1.6 Antiphase Domain Effects

For the case of nickel aluminides (1), antiphase domain structures with disordered films wetting the boundaries

(APDBs) were effective in dispersing slip and enhancing the hot ductility of the material. This ultimately improved the weldability of nickel aluminides, virtually eliminating HAZ cracking during welding. In the case of iron aluminides, APD structures (B2 or DO_3) can be formed; B2 domains will form first, with DO_3 domains forming within these. If these domain structures were effective barriers to dislocation motion, then a greater fraction of ductile rupture would be expected at 500°C upon cooling, since the material would order in the DO_3 phase field during deformation. During deformation, DO_3 domains are likely to be formed. However, quasi-cleavage dominates the fracture behavior. Therefore, it is reasonable that APDBs are not effective in dispersing slip. Since the NNNAPB energy in DO_3 Fe_3Al is low compared to other ordered systems, the dislocations may not see these APDBs as barriers and slip through them, even though they exist on {110} planes. In Ni_3Al alloys modified with chromium (1), a disordered skin wetted the APDBs, effectively uncoupling the superlattice dislocations and enhancing cross slip in the material. This also indicates the material passed through a two phase ($\gamma+\gamma'$) region upon cooling. For the case of FA-129, which contains 28 at. pct aluminum, a disordered skin of sufficient thickness may not exist, due to the lack of a two phase region at any

intermediate temperature, and based on the binary alloy phase diagram, Fig. 1.1. Krzanowski and Allen (30) indicated that quenching of alloys with compositions near the two phase α+B2 field resulted in B2 antiphase domains with the disordered α phase wetting the APDBs. Since the aluminum composition of FA-129 will dictate the phase transitions for this alloy, and chromium does not affect the positions of these phase fields, the composition of this alloy is too far away from both the α+B2 and α+DO_3 phase fields (30, 31) to realize any potential for disordered skins to wet either the B2 or DO_3 APDBs. Whether these regular APBs influence the dislocation motion through FA-129 is not well established, but hot ductility and fracture evidence indicates that they are not effective barriers to dislocation motion.

3.1.7 Summary of Sheet Results

The results of the hot ductility tests on sheet specimens indicated that regardless of the microstructure before subjecting the material to a weld thermal cycle, considerable grain growth occurred. This resulted in significant decreases in ductility and changes in fracture behavior. Also, it was apparent that B2 or DO_3 antiphase domains and their boundaries could not provide any slip

dispersal since the composition of FA-129 is too far away from any two-phase, ordered-disordered fields.

3.2 Effect of Long Range Order on Ambient Properties

Sheet tensile bars were subjected to long-time anneals at 500°C. Specimens tested consisted of material in the stress relieved condition (B2), and specimens annealed at 500°C for 24, 48, and 96 hours to create DO_3 long range order. B2 and DO_3 long range order parameters were calculated from x-ray diffraction data from sheet samples. As can be seen in Fig 3.13, significant changes in the DO_3 long range order parameter do not affect the ambient temperature properties. Thus, it was postulated that the long range order parameter was not a contributing factor to the deformation behavior of the material.

3.3 Effect of Cooling Rate on Round Specimens

The starting microstructure of the round bars is shown in Fig. 3.14, with a grain size of 42μm.

The effect of cooling rate between 1000 and 700°C appeared to make little difference in the material behavior. Plots of fracture strength and percent reduction of area versus temperature for the three different cooling rates are

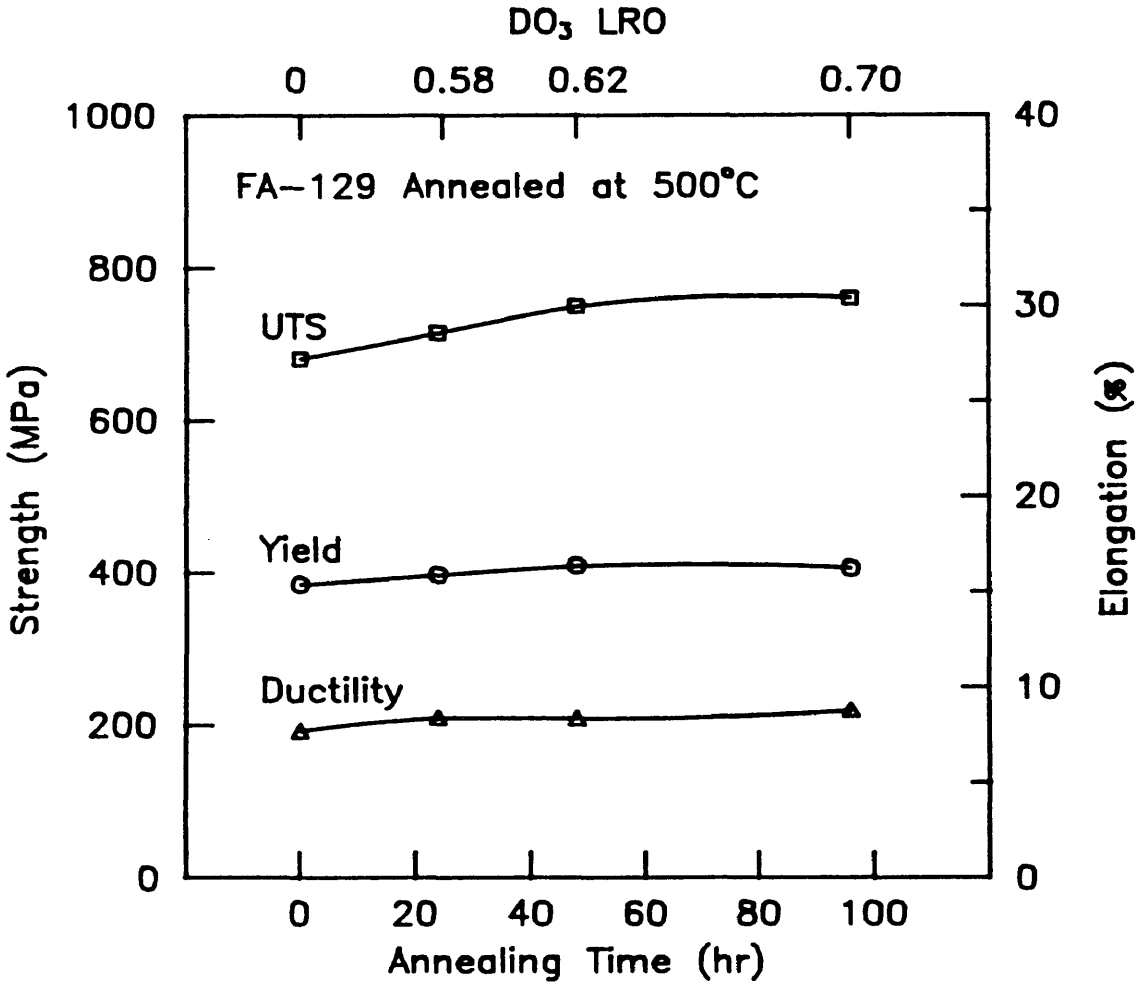

Figure 3.13 Yield strength, fracture strength, and ductility versus long range order for sheet specimens tested at room temperature in ambient air.

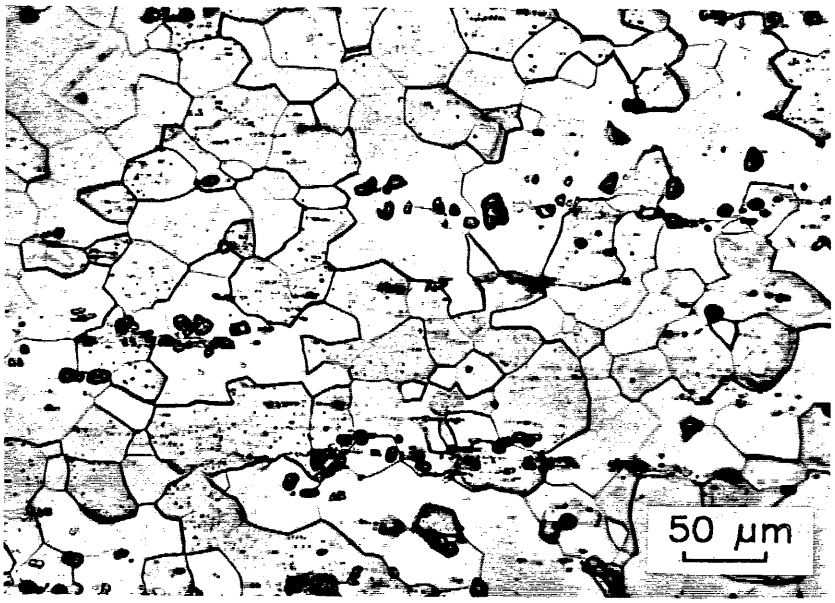

Figure 3.14 Recrystallized microstructure of round tensile bars. Average grain size is 42 μm.

presented in Figs. 3.15 a) and b), respectively. In addition, fractographs of the hot ductility specimens quenched at 100°C/s are presented in Fig. 3.16. These represent the typical fracture behavior with temperature, since there were no significant differences in fracture behavior between the cooling rates (heat input). These results support the finding that no significant differences in material behavior were observed for the range of cooling rates studied

3.4 Effect of Environment

The results of hot ductility testing in the helium-water vapor atmosphere (He-54% RH) are now presented.

Successful tests, indicated by fracture within the control zone, were accomplished at 100°C and 358°C. Tests where the control zone temperature was 300°C did not fracture within that region. For these hot ductility tests, the specimens failed at the shoulder where the diameter had achieved 0.097". A thermocouple attached to the same place on an identical specimen which experienced only the thermal program for the 300°C test indicated that the shoulder temperature was 165°C. This same specimen was used to determine the control zone temperature which gave a shoulder temperature of approximately 200°C. This temperature was

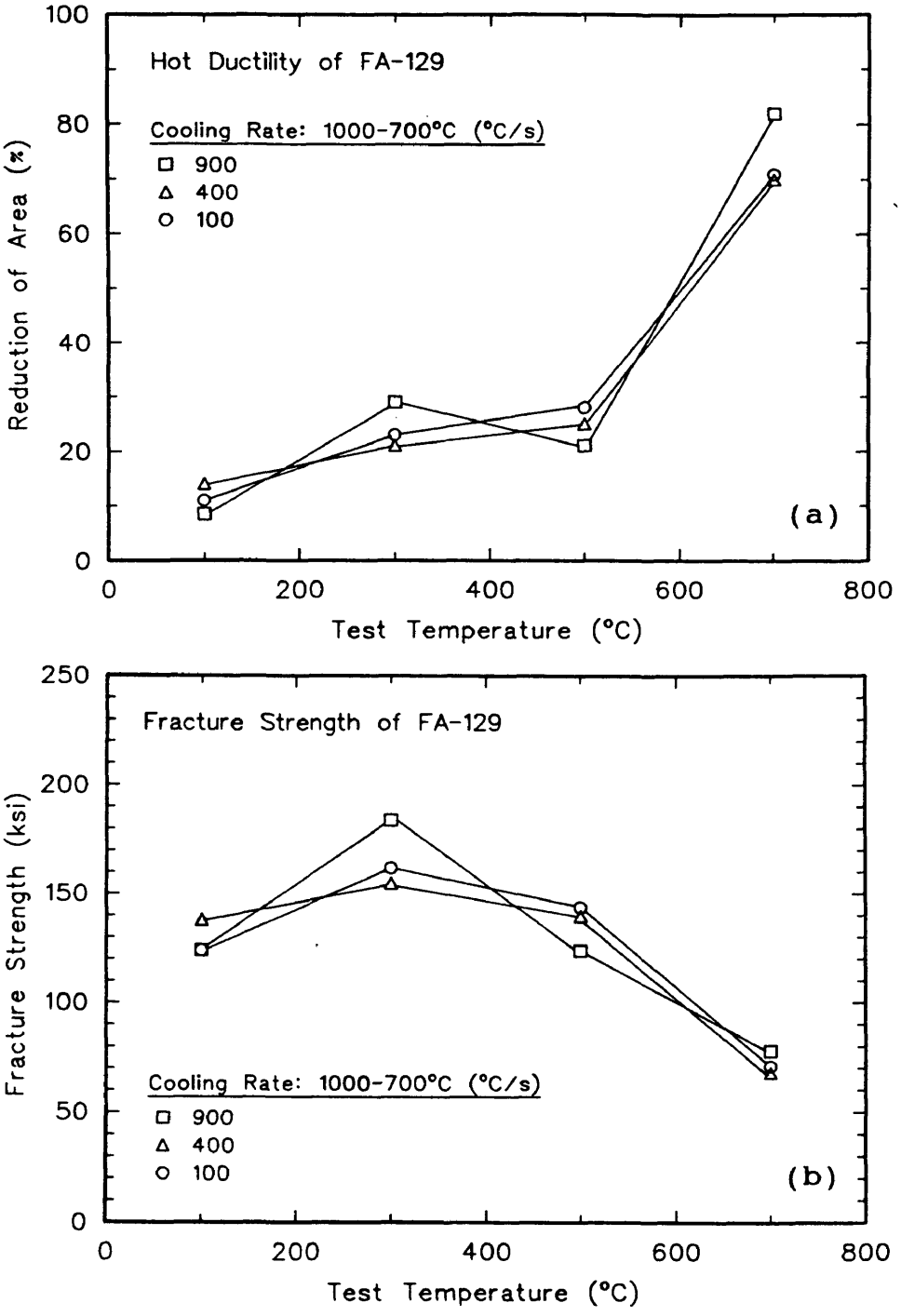

Figure 3.15 Results of on-cooling hot ductility tests for different cooling rates, tested in argon + UHP helium environment: a) hot ductility, and b) fracture strength.

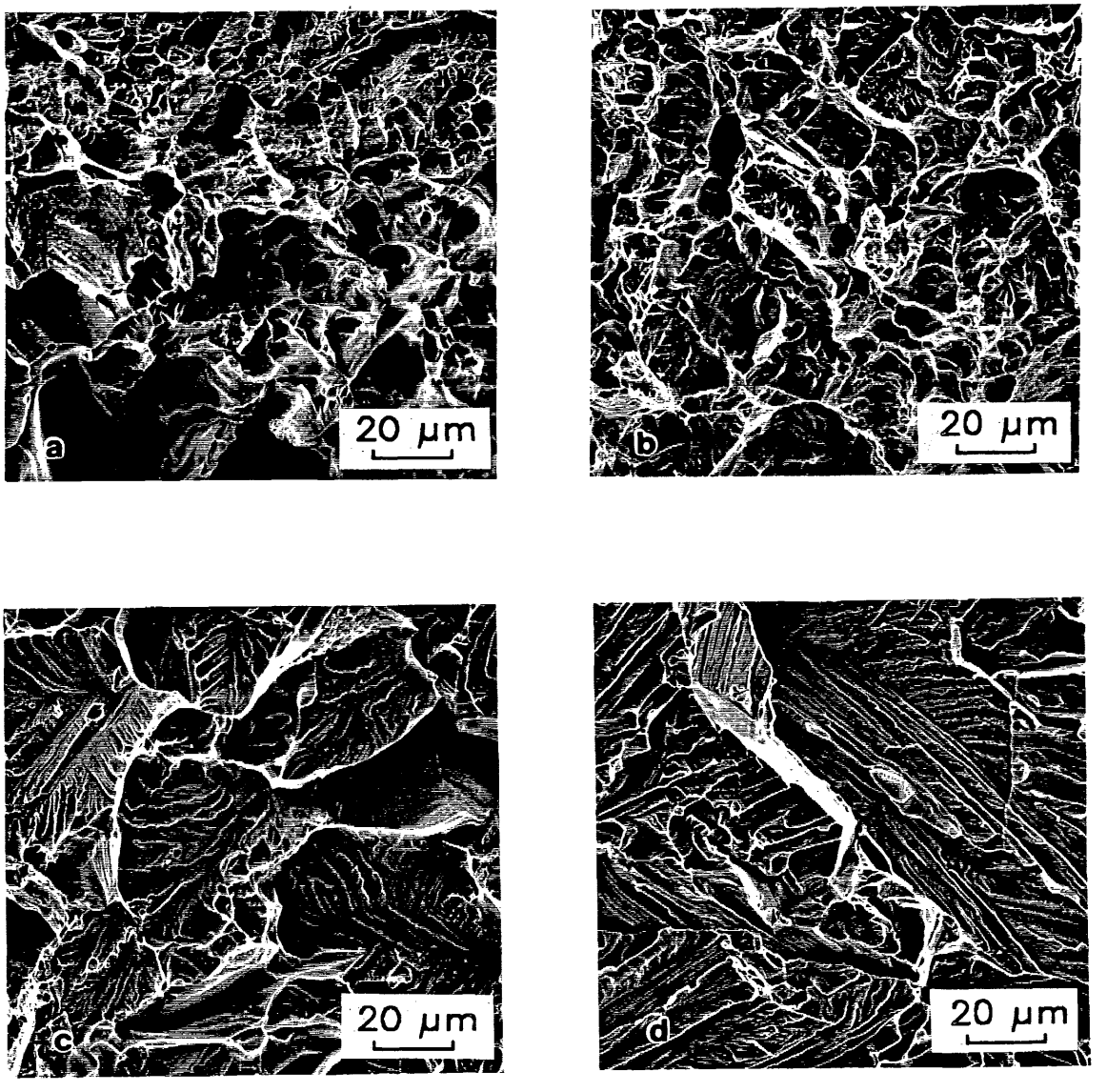

Figure 3.16 SEM fractographs of specimens quenched at 100°C/s: a) 700°C, b) 500°C, c) 300°C, and d) 100°C.

chosen since in general, steels will see a diminishing hydrogen embrittlement effect at 200°C, Fig. 3.17 (61). It was found that a control zone temperature of 358°C gave a shoulder temperature of 195°C. For this shoulder temperature, the specimen fractured in the control zone, indicating a lack of embrittlement susceptibility. Interestingly enough, a specimen which achieved a control zone temperature of 354°C, experienced a shoulder temperature of 190°C and promptly failed at the shoulder. These results emphasized the real temperature sensitivity to hydrogen embrittlement.

Embrittlement at 100°C for the two different cooling rates was indicated by the percent decrease in fracture strength and percent reduction of area based on specimens tested in the helium atmosphere, Table 3.1.

Table 3.1 Percent Change (Δ) in Material Properties Tested at 100°C in He-54%RH Environment

Cooling Rate (°C/s)	%Δ Ductility	%Δ Fracture Strength
400	22	19
100	44	34

Results for the 300°C control zone tests in the He-54% RH environment, which fractured at 165°C at the shoulder, could

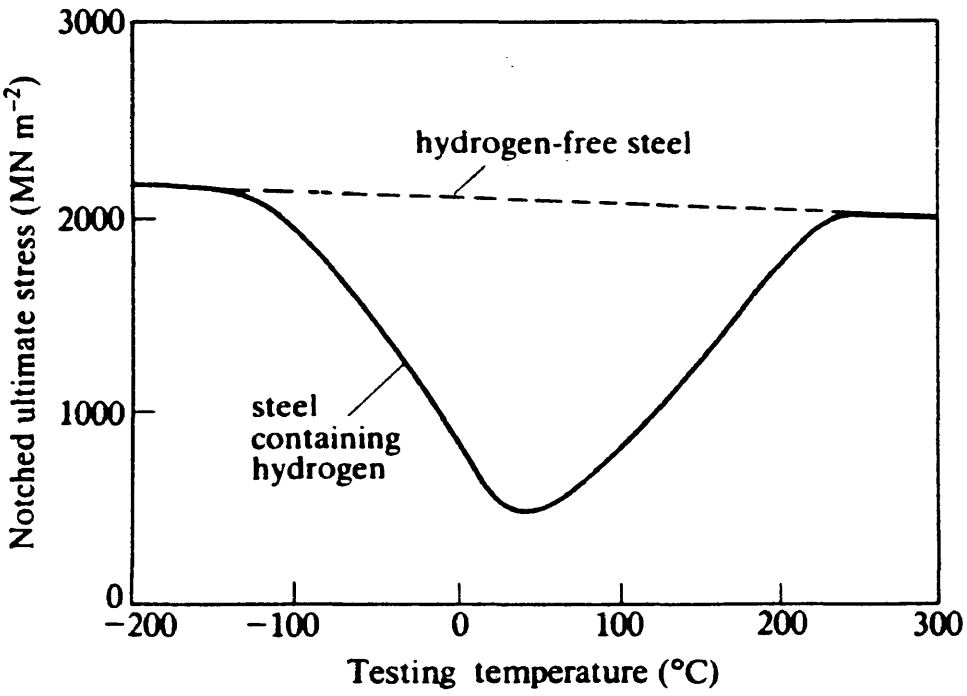

Figure 3.17 Effect of hydrogen on fracture strength of steel versus temperature. From Lancaster (60).

not be compared, and were plotted in Fig. 3.18 a) and b) with data generated from dry helium tests for comparison.

Fractographs of the specimens tested in the He-54% RH environment are compared to the fractographs of the specimens tested in dry helium in Fig. 3.19. For the 400°C/s cooling rate tests, there is no significant difference in fracture morphology between the two atmospheres. That is, mixed quasi-cleavage and intergranular fracture are observed in both environments. Also, the ductility difference is 22%. No significant difference was seen in the deformation behavior, as shown in the load-stroke (deflection) data from the hot ductility tests, Fig. 3.20. The only indication an embrittlement phenomenon occurred was the decrease in ductility and fracture strength.

For the 100°C/s cooling rate tests, however, there was a noticeable difference observed in the fracture morphology between the two environments as seen in Fig. 3.21. The dry helium fracture surface showed typical mixed quasi-cleavage and intergranular fracture. Comparing the two specimens, it was observed that there were finely-spaced tear ridges on the cleavage facets for the specimen tested in dry helium. For the specimen tested in He-54% RH, the tear ridges were spaced further apart and not as high in elevation, plus

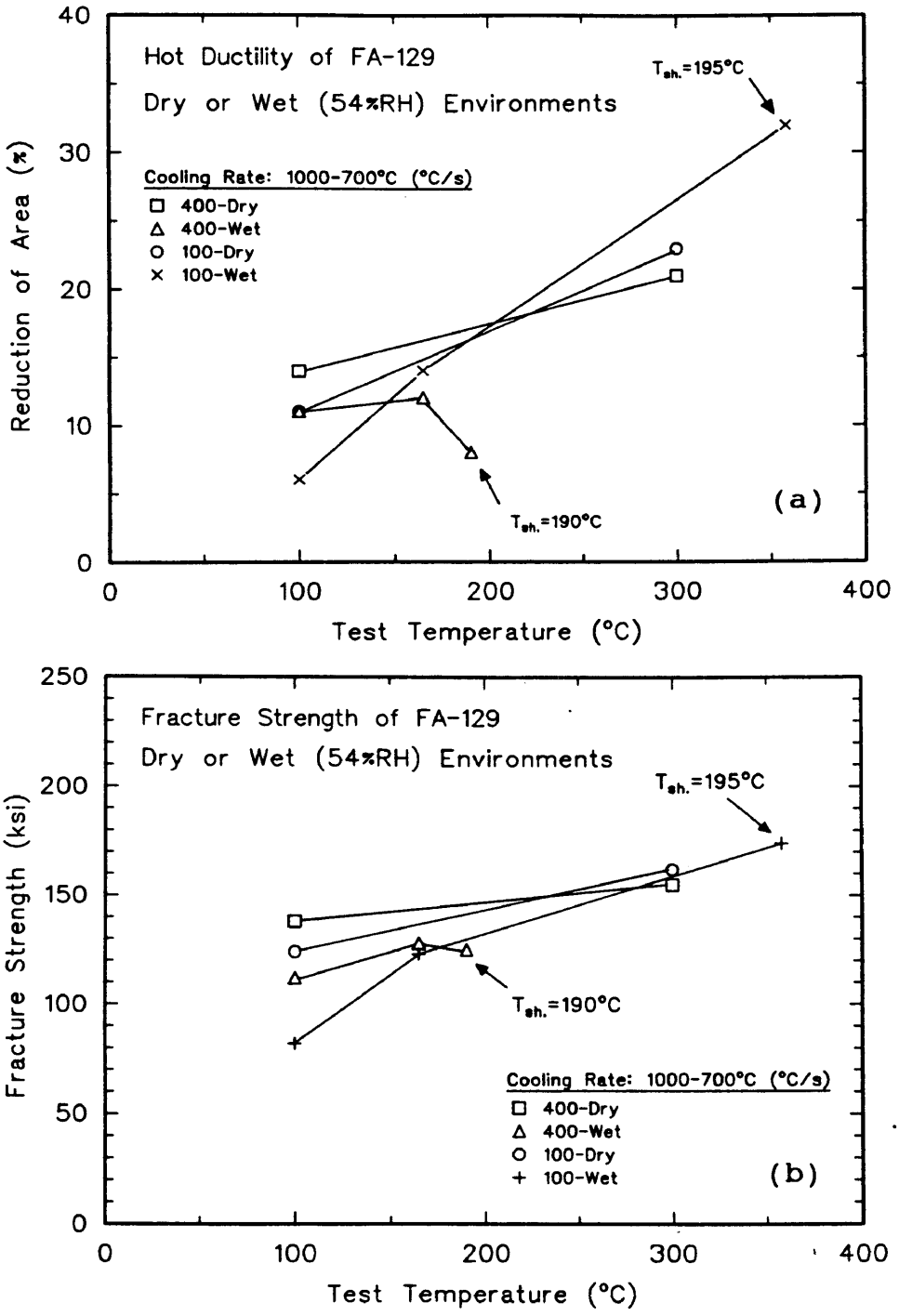

Figure 3.18 Results of testing in He-54% RH environment compared to dry helium testing; a) ductility, and b) fracture strength.

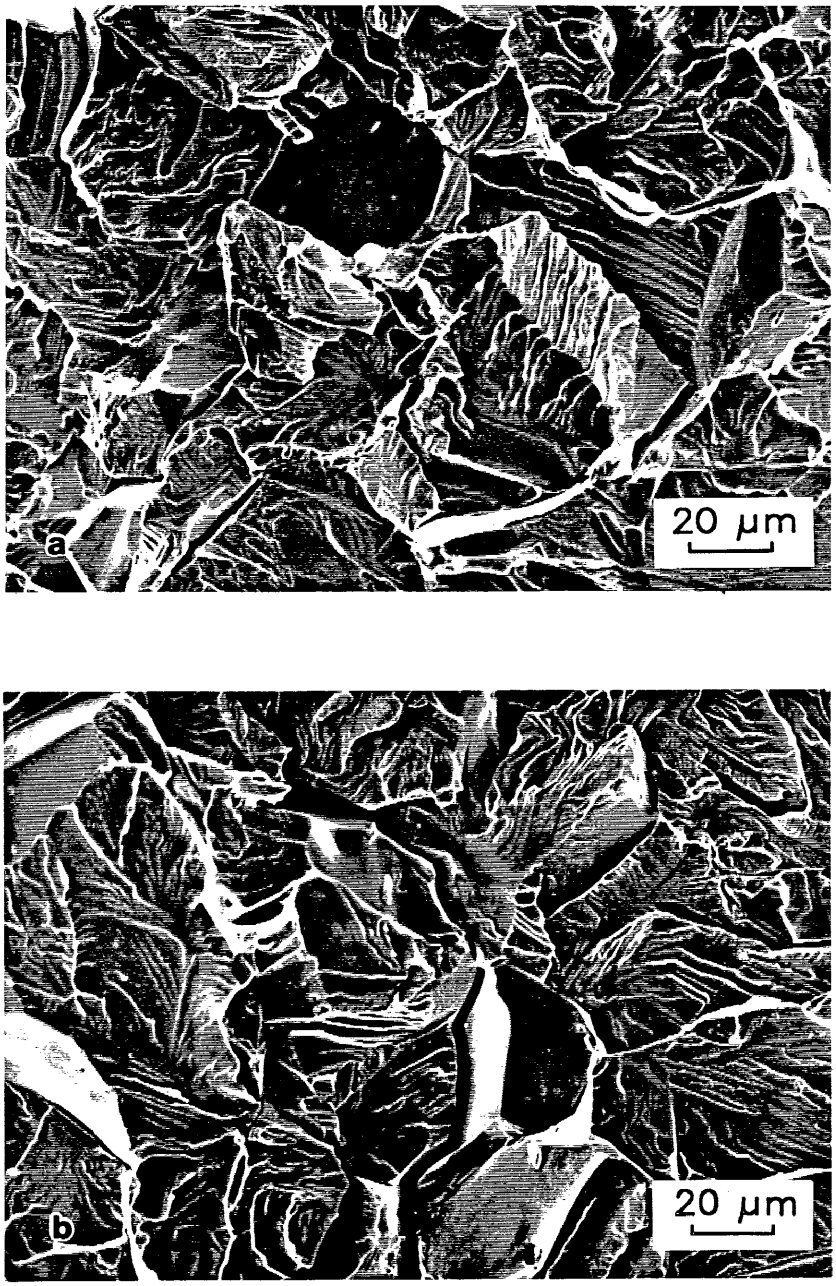

Figure 3.19 SEM fractographs of specimens tested in dry helium a), and He-54%RH, b). 400°C/s cooling rate, tested at 100°C.

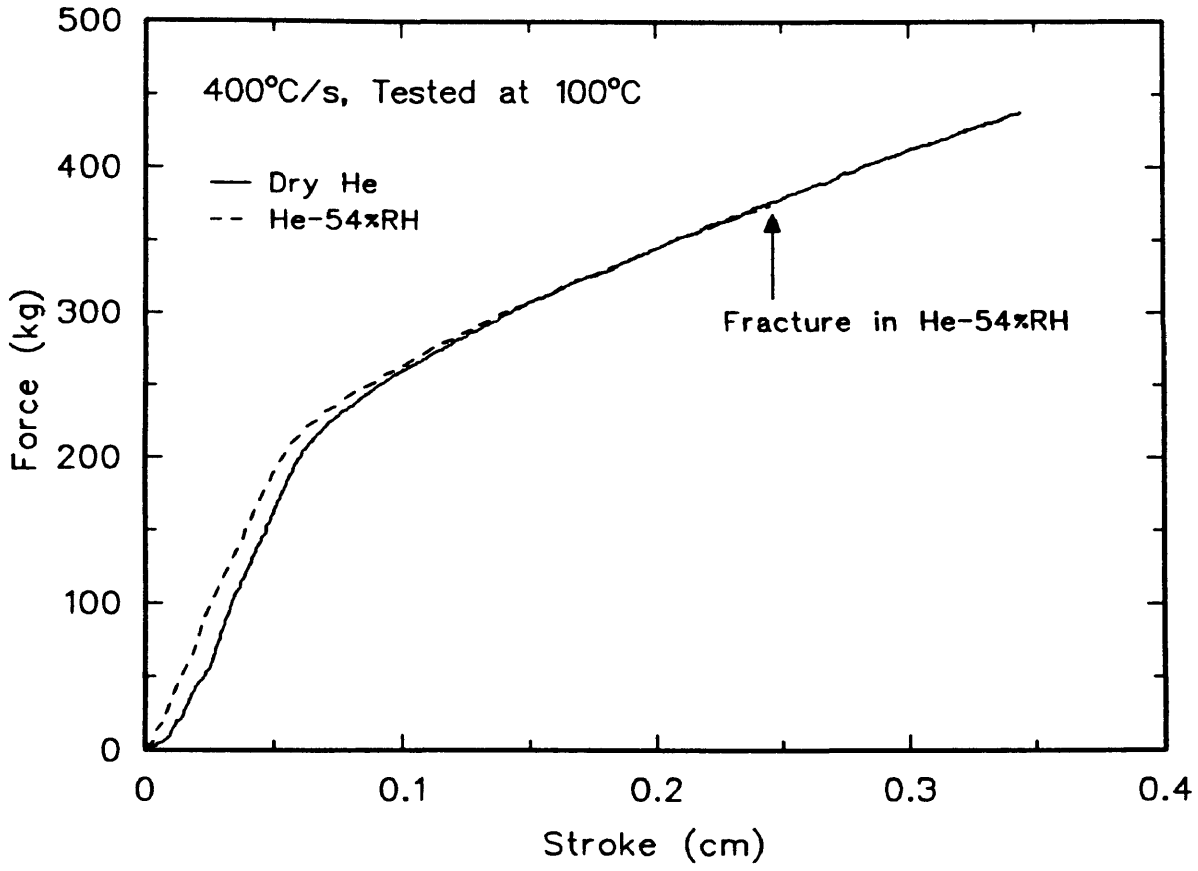

Figure 3.20 Load versus stroke curves for 400°C/s tests.

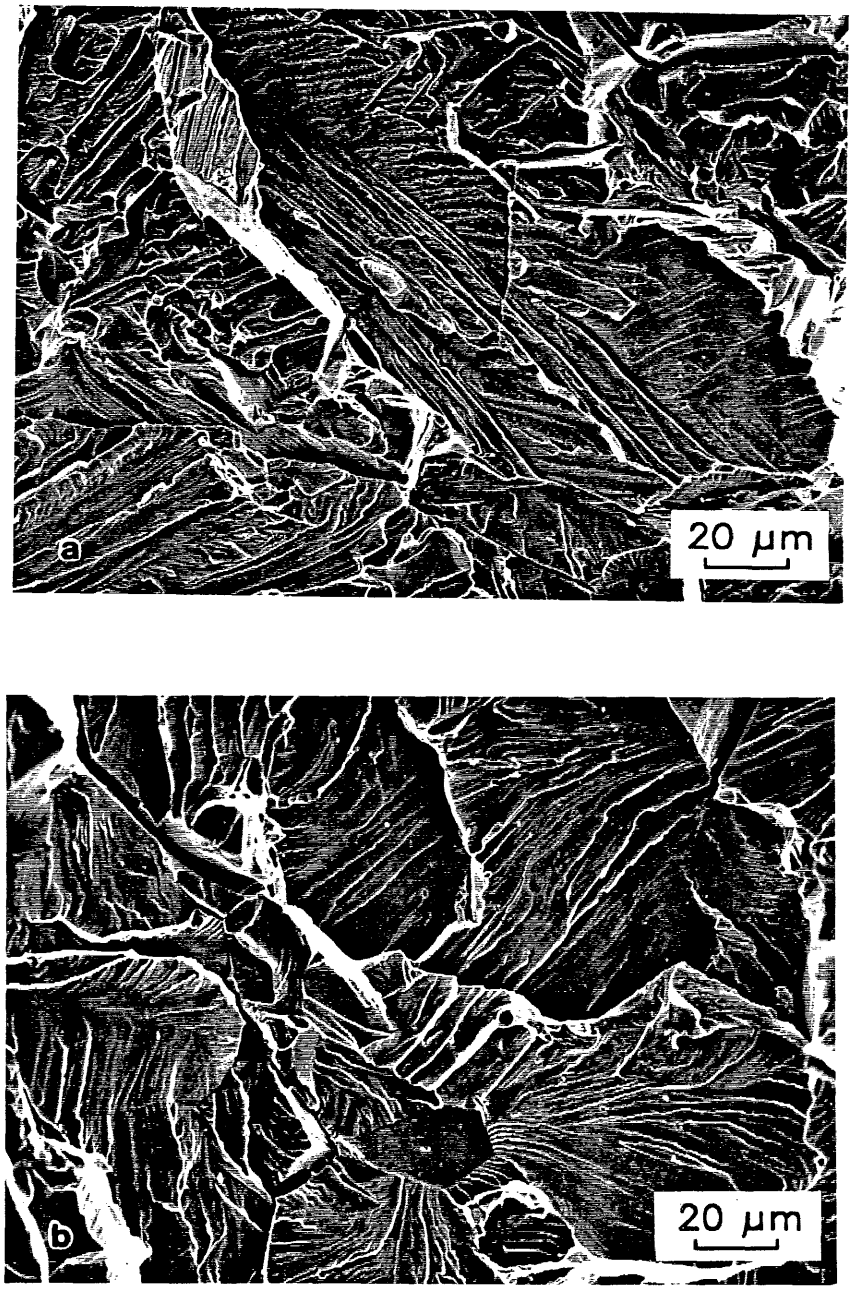

Figure 3.21 SEM fractographs comparing: a) dry helium environment, and b) helium-54%RH environment. 100°C/s cooling rate, tested at 100°C.

there was evidence of pure cleavage (flat facets) between the tear ridges. These results support the enhancement of cleavage crack nucleation and reduced plasticity. In addition, the ductility change was 42%. The load-stroke curves for both 100°C/s cooling rate tests are also shown in Fig. 3.22 for comparison. It was observed that there were striking differences in their yielding behavior. The material in He-54% RH yielded at a higher load (stress), yet strain hardened at approximately the same rate as the specimen tested in dry helium. This should also be compared to the 400°C/s tests where no significant differences in yielding hardening behavior were observed.

3.5 Fracture Behavior with Temperature

With the use of round tensile bars and stainless steel hot grips, the fracture behavior of FA-129 below 500°C was evaluated, in contrast to the sheet specimens. On-cooling fracture behavior of round tensile bars at 500°C and above compared well to the sheet specimen results.

Based on both the sheet and round tensile bar fractography results, a fracture map of FA-129 with temperature is presented in Fig. 3.23. As can be seen, the more brittle quasi-cleavage fracture morphology initiates between 600 and 500°C. However, the quasi-cleavage is

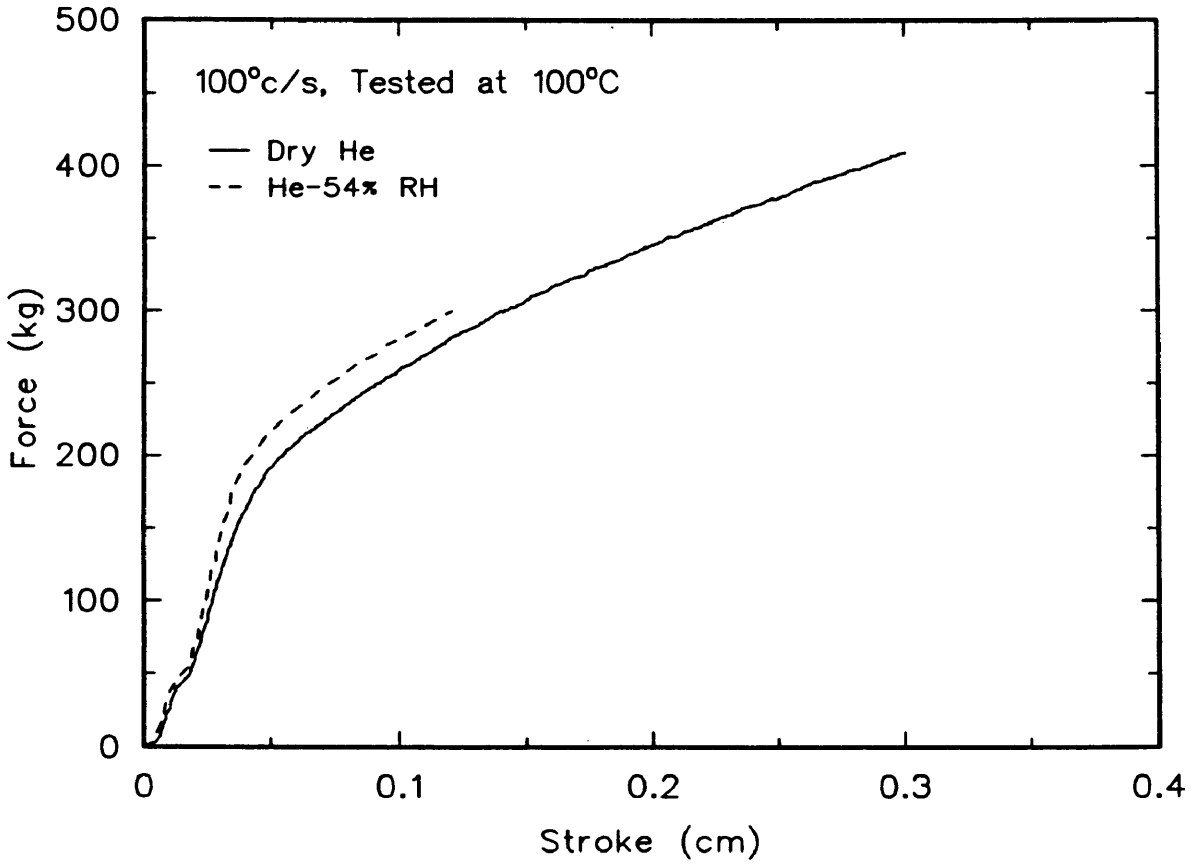

Figure 3.22 Load versus stroke curves for 100°C/s tests.

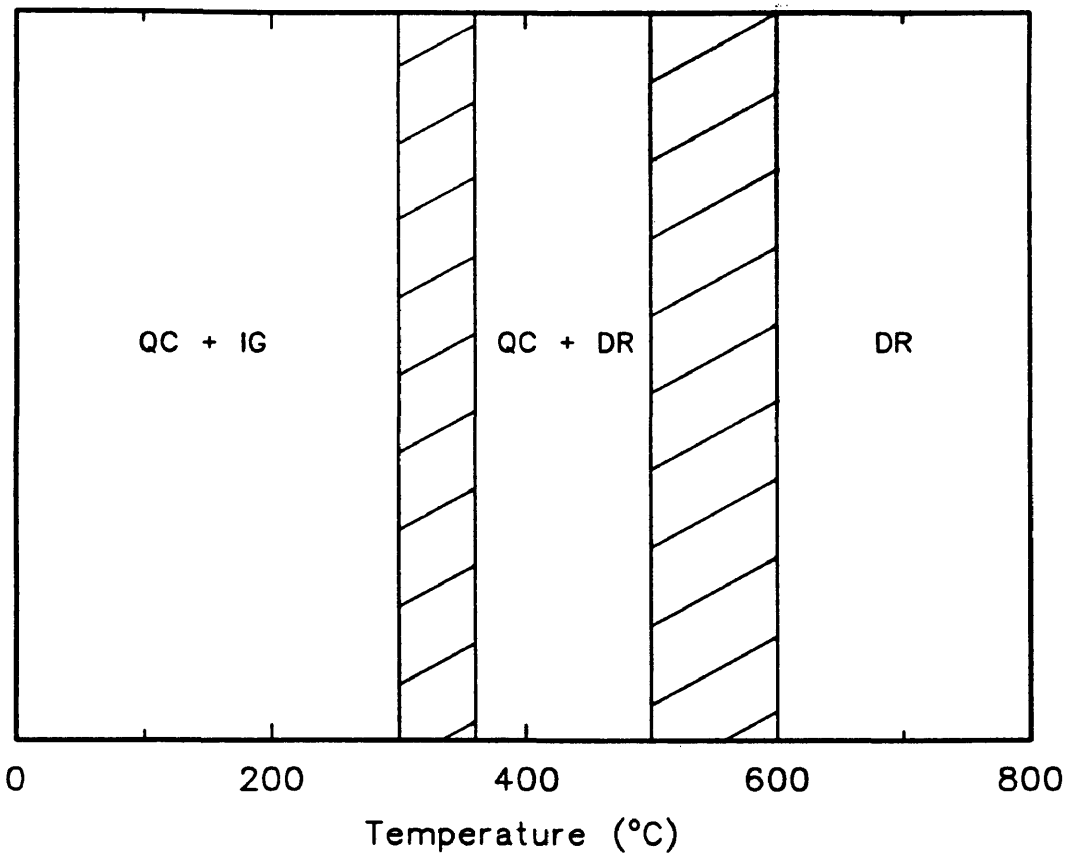

Figure 3.23 On-cooling fracture behavior map versus temperature for alloy FA-129.

present along with ductile microvoids, and this behavior continues until approximately 358-300°C. Below 300°C, the material exhibits a mixed, quasi-cleavage and intergranular morphology, without any ductile microvoids. The disappearance of ductile microvoids is indicative of a ductile-to-brittle transition temperature (DBTT). For FA-129, the DBTT is somewhere in the range of 300-358°C, since regions of ductile rupture coincided with quasi-cleavage at 358°C and 500°C. To further support this, high temperature charpy impact data for iron aluminide alloy FAH (same composition as FA-129) are presented in Fig. 3.24 (62). It was observed that the temperature where the upper-shelf energy is reached is 350°C for the LT orientation.

Further indications that the DBTT is within this temperature range were observed for the fracture strength data for the round Gleeble tensile bars. The fracture strength increased with decreasing temperature, from 700°C to a peak fracture strength (400°C/s) at 358°C (He-54% RH) or 300°C (dry helium). Below 358°C, the fracture strength decreased. These results can be explained as follows. For a true brittle material, there will be a transition temperature where fracture changes from brittle to more ductile behavior. Below this temperature, the stress necessary to cause ductile rupture (microcrack nucleation)

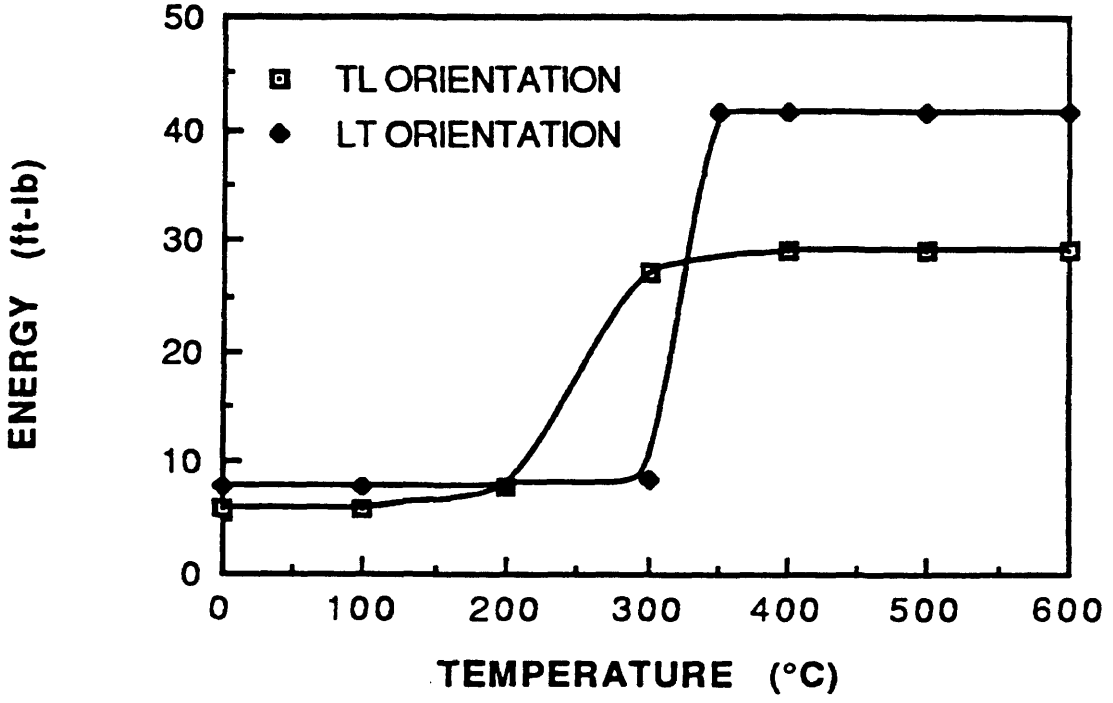

Figure 3.24 Charpy impact data for Fe_3Al-based iron aluminide alloy FAH (FA-129). Reprinted by permission of Dave Alexander, ORNL (62).

is much higher than the stress to cause brittle fracture (microcrack propagation). The stress to cause ductile rupture normally decreases with an increase in temperature whereas the brittle fracture stress is taken to be temperature insensitive. Above the temperature where both stresses are equal, the material can nucleate microcracks, but the stress necessary to propagate them is so much higher that the material fails in a ductile manner, ie. microvoid coalescence. Using this logic, the behavior of FA-129 can then be explained. Below 300°C, the material failed by a brittle mechanism while the fracture strength increased with temperature to this point. Above 300°C, the material shows signs of microvoid coalescence along with quasi-cleavage. In addition, the fracture strength decreased with increasing temperature from this point as the frequency of microvoid coalescence increased. A schematic of this thinking for FA-129 is presented in Fig. 3.25.

3.6 Hydrogen Embrittlement in FA-129

With the results of the He-54%RH tests, a logical understanding of hydrogen embrittlement in FA-129 can now be presented.

As anticipated, testing in the water vapor atmosphere decreased both the fracture strength and ductility,

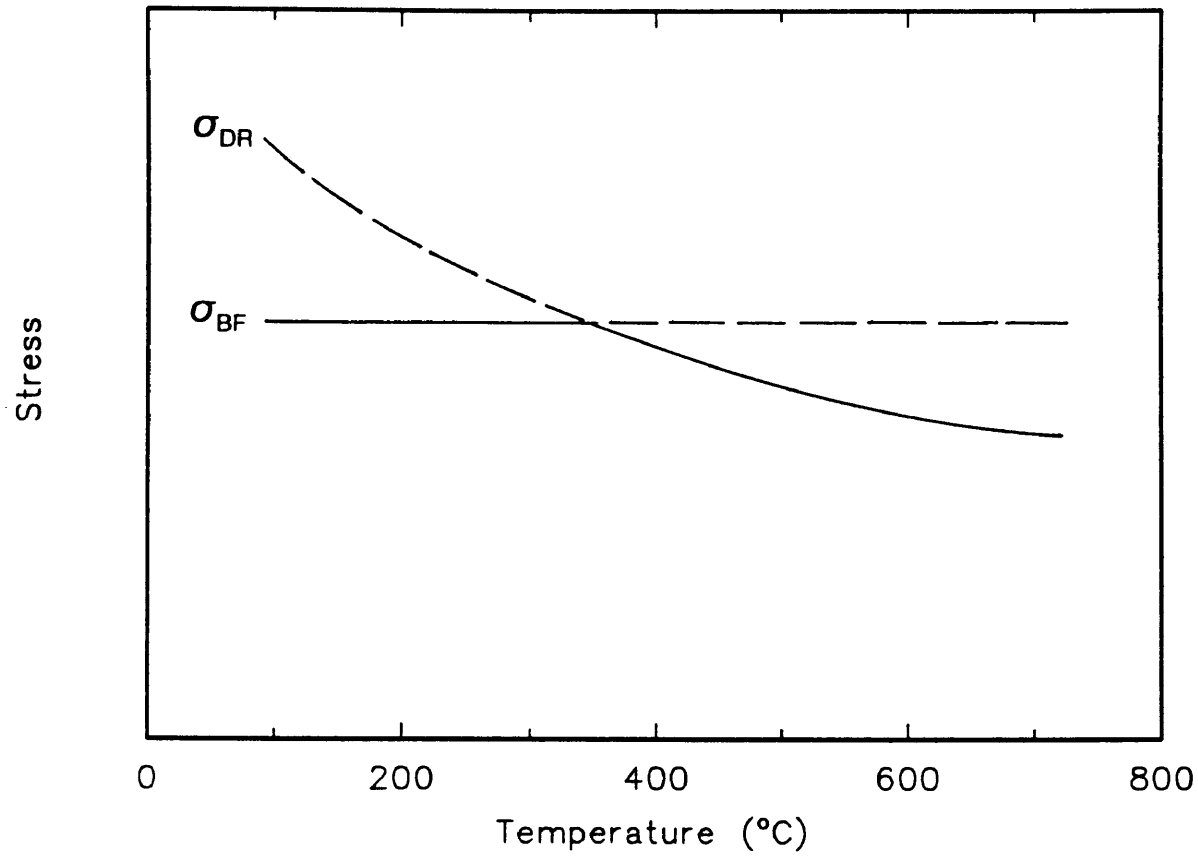

Figure 3.25 Change in both brittle fracture stress and ductile rupture stress with temperature, indicating a ductile-to-brittle transition temperature near 350°C.

confirming the results of Liu and coworkers (36). For the specimens quenched at 400°C/s, no significant difference in fracture morphology was observed. This is not surprising since the material behaved in a brittle manner at temperatures below 300°C, regardless of atmosphere. This is also in agreement with Liu and coworkers (36), who observed no change in fracture morphology with widely differing atmospheres for Fe_3Al-based alloys. However, the specimens quenched at 100°C/s showed noticeable differences in fracture and yielding behavior. Hence, the embrittlement for the specimens quenched at the lower cooling rate (100°C/s) was more severe than that for the specimens quenched at the higher cooling rate (400°C/s).

Additionally, the material's susceptibility to brittle fracture was exacerbated by the lack of dispersed slip below 500°C upon cooling, and further enhanced by the reaction of water vapor to release hydrogen for embrittlement at temperatures below 200°C. Softening (or increased slip) on the {110} slip plane has been observed for hydrogen-charged iron and steel (37), and cleavage cracks have been observed to propagate on {110} planes in pure iron also charged with hydrogen (43). For hydrogen-charged Fe-3%Si alloys (44), slip occurs primarily on {110} planes, yet secondary slip traces directly ahead of cleavage cracks were determined to

be {112} planes. This secondary slip behavior was indicative of high stresses surrounding the crack region, and resulted in high resolved shear stresses which initiated slip on {112} planes. Cleavage cracks propagated on {100} planes, which were also observed by Nakasato for similar alloys.

For FA-129, it was difficult to tell if the cleavage planes were {100} or {110}. For the 100°C/s quenched specimen tested at 100°C in He-54% RH, more clean cleavage facets were seen, along with wider-spaced tear ridges compared to the one tested in dry helium. Since the specimen tested in dry helium revealed ductile tear ridges which were higher in elevation, one may conclude that cleavage occurred on {110} planes, similar to what was found for hydrogen cracking in pure iron (43). However, no striations parallel to crack fronts were observed in FA-129, tested in either dry or wet helium environments. The tear ridges present on the cleavage facets emphasize that very localized plasticity occurred during fracture. This may be the result of {112} slip in FA-129, which would be localized to the crack tip regions regardless of whether the material was in a dry or wet environment. It should also be noted that aluminum and silicon affect iron in similar ways, yet to a different extent. Both alloying additions result in

DO_3 superlattice formation. However, silicon additions greatly enhance the ordering energies between iron atoms, which are not as strong when iron is alloyed with aluminum. Nakasato and Bernstein (43) noticed a transition from {110} plane cracking to {100} cleavage plane cracking at about 1.5 wt. pct silicon. Thus, the fracture behavior of FA-129 in a dry helium atmosphere could be a result of {110} and {100} cleavage cracking. Further fractographic studies would help elucidate this in iron aluminides.

Finally, lack of dispersed slip in iron aluminides leaves the material susceptible to embrittlement in the presence of water vapor. The reaction between water vapor and aluminum (Equation 1.10) releases molecular hydrogen to adsorb, dissociate into an atomic species which is also adsorbed. Whether the adsorbed atomic hydrogen onto crack surfaces, or the diffusion of atomic hydrogen into the matrix ahead of cracks affects dislocation motion in the material can not be directly inferred from the observed behavior in FA-129. Yet, it is apparent that dislocation motion is affected by the presence of hydrogen, and may restrict the dislocations on {110} slip planes. Other factors which may restrict dislocation motion on {110} slip planes and increase the susceptibility to hydrogen embrittlement are: 1) APB energies have minima on {110} slip

planes, and 2) chromium additions reduce APB energies.

3.6.1 Temperature Limit to Hydrogen Embrittlement

Because a shoulder temperature of 195°C resulted in a control zone fracture (358°C) in the He-54% RH environment, this is evidence that an upper temperature limit exists for hydrogen embrittlement in iron aluminides. Approaching this in terms of adsorption theory from LMIE (63), theta (θ), the fraction of cracked surface covered with adsorbed species, will equal zero at the upper limit temperature where adsorption controls, and equal one at the lower limit temperature where diffusion controls. Thus, theta is a thermally activated function which shows an exponential decrease with temperature according to the function (63):

$$\theta = [1 - \exp(-\frac{\Delta G}{RT})] \qquad (3.1)$$

Where ΔG is the decrease in free energy resulting from the embrittler-parent metal atomic interaction (64). This theory provides a reasonable explanation for the behavior observed in FA-129. At the upper temperature limit, diffusion is not the controlling step; it is the adsorption of molecular hydrogen gas (38) onto crack surfaces which controls. Since the adsorption rate of hydrogen on iron decreases with increasing temperature (38), so should the

extent of embrittlement.

3.6.2 Effect of Hydrogen on Fracture and Flow Properties

According to adsorption theory (63), the fracture strength of the material should increase as theta decreases. Although the fracture strength increases with temperature from 100 to 300°C in the dry environment (possibly due to short-range ordering effects), the fracture strength also increases in the wet environment (100-358°C). As the temperature increases, the fracture strength values in the wet atmosphere begin to approach the values in the dry environment, Fig. 3.18. This phenomenon can be described best by (64):

$$\sigma_e = \sigma_c (1 - \beta\theta) \qquad (3.2)$$

where σ_e is the fracture strength lowered by the presence of embrittling species covering the crack surface (θ), β is a constant for a particular system, and σ_c is the unembrittled fracture (cohesive) strength. This would result in an exponential increase in the fracture stress with temperature to 200°C, in contrast to the temperature-insensitive value of the fracture stress shown in Fig. 3.25. At this upper limit temperature, the fracture stress in the water vapor environment would approach that of the value observed in a

benign environment. Thus it is observed that the fracture strength of FA-129 in the water vapor environment increased with temperature, and approached the values observed in the dry helium environment.

For the case of flow behavior, the water vapor environment had no apparent effect on yielding or strain hardening behavior of the specimens quenched at 400°C/s and tested at 100°C. However, for the specimens quenched at 100°C/s and tested at 100°C, the yielding behavior was different in the presence of water vapor. Higher load at yielding may indicate dislocation pinning by the presence of either adsorbed hydrogen or hydrogen which diffused into the matrix. In either case, localized, intense slip which occurred in the presence of hydrogen increased the rate of cleavage crack nucleation and propagation.

Thus, it is apparent that the environmental embrittlement of iron aluminides can be explained by examining the behavior of aluminum in the presence of water vapor, and iron in the presence of hydrogen gas. Water vapor must react with the aluminum in FA-129 at freshly cracked surfaces to liberate hydrogen gas. This hydrogen gas must then adsorb, dissociate into atomic hydrogen, which also adsorbs. Whether this adsorbed atomic species, or hydrogen which diffused into the matrix, was solely

responsible for the influence on dislocation motion was not established in this investigation. Regardless of this, the presence of water vapor in the environment embrittled FA-129.

4. CONCLUSIONS

Based on the results of this study, the following can be concluded:

1) The microstructure of FA-129 was unstable with respect to weld thermal cycles, regardless of processing prior to welding.

2) Grain growth during weld thermal cycles reduced the brittle fracture resistance of FA-129.

3) The iron aluminide alloy FA-129, when fractured during the cooling cycle, exhibited large changes in fracture behavior with temperature but not with cooling rate (heat input).

4) The disappearance of microvoid coalescence in the 358 to 300°C range indicated a ductile-to-brittle transition for FA-129.

5) In addition to a grain size effect, FA-129 was further embrittled by the presence of water vapor. Decreases in ductility and fracture strength were observed for tests performed in a water vapor-bearing environment.

6) Fracture behavior at 100°C did not change significantly between dry or wet helium environments for material quenched at 400°C/s. However, significant changes occurred for the material quenched at 100°C/s and tested in the wet

environment, indicated by increased spacing between tear ridges and more cleavage facets between these ridges.

7) The environmental embrittlement of FA-129 diminished at approximately 200°C for the He-54% RH environment, and indicated adsorption of the embrittling species was the controlling step near this upper temperature limit.

8) In terms of hot ductility and fracture behavior, there were no significant indications that domain structures (B2 or DO_3) were beneficial in alleviating cold cracking susceptibility. It is emphasized that TEM was not used to quantify the domain structures present in fractured specimens.

5. SUGGESTIONS FOR FURTHER WORK

This study looked at only one iron aluminide which was modified with chromium. David and coworkers (10) mentioned that niobium additions to binary iron aluminides resulted in weld cracking resistance similar to alloys containing chromium. To the author's knowledge, no studies examining the effects of niobium on hot ductility behavior exist. Careful study of niobium may serve to improve weldability behavior.

Second, only a few qualitative weldability tests on alloys containing less than 28 at. pct aluminum have been performed (9). These alloys would have possibly given two-phase, ordered plus disordered microstructures. However, since TiB_2 was added to limit grain growth, hot cracking of the alloys occurred. The effects of decreasing aluminum content on material properties have been studied, yet no in-depth knowledge on the effects of weld cracking resistance have been established. In the author's opinion, it would be interesting to see if disordered films at domain boundaries could serve to enhance the weldability of iron aluminides, since these effectively eliminated weld cracking in chromium-modified nickel aluminides (1).

Because FA-129 has a DBTT of approximately 350°C, the

fracture toughness of the material can typically be enhanced by refining the dislocation barrier spacing. Exclusive of a domain structure, fine, second phase dispersions, or methods to limit grain growth without inducing hot cracking will be the most important step to successfully utilizing iron aluminide alloy FA-129 in welding applications. Another consideration may be pre- and post-weld heat treatments to limit cold cracking, as noted by Brooks and Volio (9) in their studies of iron-aluminum alloy weldability. Also, control of atmosphere will be essential in limiting environmental embrittlement.

Finally, thermal conductivity could be considered in terms of thermal stresses generated by welding, as shown by Santella and coworkers (54) for nickel aluminides. Higher thermal conductivity alloys could alleviate thermal stresses more effectively than lower conductivity alloys, regardless of their hot ductility behavior. Since iron aluminides tend to have low thermal conductivity values, studies determining alloy additions which could increase thermal conductivity may be beneficial.

6. REFERENCES

1. Maguire, M. C. 1989. Weldability of Ductile Nickel Aluminides. Ph.D. Thesis. Colorado School of Mines, Golden, CO.

2. Stoloff, N. S. and R. G. Davies. "The Plastic Deformation of Ordered FeCo and Fe_3Al Alloys." Acta Met. 12 (1964): 473-485.

3. David, S. A., J. A. Horton, C. G. McKamey, T. Zacharia, and R. W. Reed. "Welding of Iron Aluminides." Welding Journal 68, no. 9 (1989): 372s-381s.

4. David, S. A., T. Zacharia, and R. W. Reed. "Weldability of Advanced Iron Aluminides." ORNL, 1989.

5. Sykes, C. and J. W. Bampfylde. "The Physical Properties of Iron-Aluminium Alloys." J. Iron and Steel Inst. 230, no. II (1934): 389-418.

6. Morgan, E. R. and V. F. Zackay. "Ductile Iron-Aluminum Alloys." Metal Progress 68, no. 4 (1955): 126-128.

7. Justusson, W., V. F. Zackay, and E. R. Morgan. "The Mechanical Properties of Iron-Aluminum Alloys." Trans. ASM 49 (1957): 905-923.

8. Kayser, F. X. "Iron-Aluminum Alloy Systems." WADC Technical Report 57-298 Part 1 (1957): 1-28.

9. Brooks, R. and A. Volio. "Iron-Aluminum Alloy Systems." WADC Technical Report 57-298 Part 14 (1959): 1-24.

10. McKamey, C. G., C. T. Liu, J. V. Cathcart, S. A. David, and E.H. Lee. "Evaluation of Mechanical and Metallurgical Properties of Fe_3Al-Based Aluminides." ORNL/TM-10125 (1986): 1-23.

11. Massalski, T. B., ed. 1986. Binary Alloy Phase Diagrams. Metals Park, Ohio: American Society for Metals.

12. Bradley, A. J. and A. H. Jay. "The Formation of Superlattices in Alloys of Iron and Aluminium." Proc. Roy. Soc. 136A (1932): 210-232.

13. Allen, S. M. and J. W. Cahn. "Mechanisms of Phase Transformations Within the Miscibility Gap of Fe-Rich Fe-Al Alloys." Acta Met. 24 (1976): 425-437.

14. Rivlin, V. G. and G. V. Raynor. "Critical Evaluation of Aluminum-Chromium-Iron System." Int. Met. Rev. 25, no.4 (1980): 139-157.

15. Stoloff, N. S. and R. G. Davies. "The Mechanical Properties of Ordered Alloys." Progress in Materials Science 13 (1966): 3-80.

16. Marcinkowski, M. J. and N. Brown. "Theory and Direct Observation of Dislocations in the Fe_3Al Superlattices." Acta. Met. 9 (1961): 764-786.

17. Leamy, H. J. and F. X. Kayser. "The Compressive Deformation of Behavior of Long Range Ordered Polycrystalline Iron-Aluminum Alloys." Phys. Stat. Sol. 34 (1969): 765-780.

18. Leamy, H. J., F. X. Kayser, and M. J. Marcinkowski. "The Plastic Deformation Behaviour of Long-range Ordered Iron-Aluminium Alloys: I. Single Crystal Deformation Experiments." Phil. Mag. 20 (1969): 763-777.

19. Ibid. "II. Transmission Electron Microscopical Observations." pp. 779-798.

20. Marcinkowski, M. J. and G. Lasko. "Behavior of Passing Dislocations in Superlattices." J. Appl. Phys. 38, no. 5 (1967): 2124-2133.

21. Marcinkowski, M. J. and G. Lasko. "Plastic Deformation Behavior in the Fe_3Si Superlattice." Trans. AIME 245 (1969): 1111-1120.

22. Marcinkowski, M. J. and D. S. Miller. "The Effect of Ordering on the Strength and Dislocation Arrangements in the Ni_3Mn Superlattice." Phil. Mag. 6 (1961): 871-893.

23. Mendiratta, M. G., H. M. Kim, and H. A. Lipsitt. "Slip Directions in B2 Fe-Al Alloys." Metall. Trans. A 15A (1984): 395-399.

24. Baker, I. and D. J. Gaydosh. "Flow and Fracture of Fe-Al." Mat. Sci. Eng. 96 (1987): 147-158.

25. Crawford, R. C. "Pairwise Interaction Energies in Iron - Aluminium Alloys." Phil. Mag. 35, no. 3 (1977): 567-574.

26. Crawford, R. C. and I. L. F. Ray. "Antiphase Boundary Energies in Iron-Aluminum Alloys." Phil. Mag. 35, no. 3 (1977): 549-565.

27. McKamey, C. G., J. A. Horton, and C. T. Liu. "Effect of Chromium on Properties of Fe_3Al." J. Mater. Res. 4, no. 5 (1989): 1156-1163.

28. Beeler, J. R. "Antiphase Boundaries and Domains." In Intermetallic Compounds. J.H. Westbrook, ed., pp. 233-268. New York: John Wiley & Sons, 1967.

29. Marcinkowski, M. J. and N. Brown. "Direct Observation of Antiphase Boundaries in the Fe_3Al Superlattice." J. Appl. Phys. 33, no. 2 (1962): 537-552.

30. Krzanowski, J. E. and S. M. Allen. "Solute-Drag Effects in Migrating Diffuse Interfaces-I. Theoretical Analysis and Application to APBs in Fe-Al Alloys." Acta. Metall. 34, no. 6 (1985): 1035-1044.

31. Ibid. "II. Experimental Investigation of APB Migration Kinetics and Comparison to Theory." pp. 1045-1050.

32. Raviprasad, R. and K. Chattopadhyay. "The Effect of Rapid Solidification on the Order-Disorder Transformation in Iron-based Alloys." Mat. Sci. Eng. 98 (1988): 281-284.

33. Davies, R. G. "Kinetics of Ordering and Domain Hardening in Fe_3Al." Trans. AIME 230 (1964): 903-907.

34. Marcinkowski, M. J. and R. M. Fisher. "Theoretical Analysis of Plastic Deformation in Superlattices Based on the Body-Centered Cubic Structure." J. Appl. Phys. 34, no. 8 (1963): 2135-2145.

35. Liu, C. T., E. H. Lee, and C. G. McKamey. "An Environmental Effect as the Major Cause for Room Temperature Embrittlement in FeAl." Scr. Metall. 23 (1989): 875-880.

36. Liu, C. T., C. G. McKamey, and E. H. Lee. "Environmental Effects on Room Temperature Ductility and Fracture in Fe_3Al." Scr. Metall. 24 (1989): 385-390.

37. Hirth, J. P. "Effects of Hydrogen on the Properties of Iron and Steel." Met. Trans. A 11A (1980): 861-890.

38. Ransom, C. M. and P. J. Ficalora. "An Adsorption Study of Hydrogen on Iron and its Relation to Hydrogen Embrittlement." Met. Trans. A 11A (1980): 801-807.

39. Pecora, L. M. and P. J. Ficalora. "A magnetization-Chemisorption Study of Hydrogen and Sulfur Dioxide on Iron." Met. Trans A 8A (1977): 1841-1848.

40. Lynch, S. P. "A Fractographic Study of Gaseous Hydrogen Embrittlement and Liquid-Metal Embrittlement in a Tempered-Martensitic Steel." Acta. Metall. 32, no. 1 (1984): 79-90.

41. Tabata, T. and H. K. Birnbaum. "Direct Observations of the Effect of Hydrogen on the Behavior of Dislocations in Iron." Scr. Metall. 17 (1983): 947-950.

42. Tabata, T. and H. K. Birnbaum. "Direct Observations of Hydrogen Enhanced Crack Propagation in Iron." Scr. Metall. 18 (1984): 231-236.

43. Nakasato, F. and I. M. Bernstein. "Crystallographic and Fractographic Studies of Hydrogen-Induced Cracking in Purified Iron and Iron-Silicon Alloys." Met. Trans. A 9A (1978): 1317-1326.

44. Tetelman, A. S. and W. D. Robertson. "Direct Observation and Analysis of Crack Propagation in Iron-3% Silicon Single Crystals." Acta Metall. 11 (1963): 415-426.

45. Speidel, M. O. 1977. "Hydrogen Embrittlement of Aluminum Alloys?" In Hydrogen Damage, ed. C.D. Beachem, 329-351. American Society for Metals, Metals Park, Ohio.

46. Scamans, G. M. and C. D. S. Tuck. 1979. "Embrittlement of Aluminum Alloys Exposed to Water Vapor." In Environment-Sensitive Fracture of Engineering Materials, ed. Z.A. Foroulis, 464-483. AIME-TMS, New York.

47. Ricker, R.E. and D.J. Duquette. "The Role of Hydrogen in Corrosion Fatigue of High Purity Al-Zn-Mg Exposed to Water Vapor." Met. Trans. A 19A (1988): 1775-1783.

48. Bond, G. M., I. M. Robertson, and H. K. Birnbaum. "Effects of Hydrogen Deformation and Fracture Processes in High-Purity Aluminum." Acta Metall. 36, no. 8 (1988): 2193-2197.

49. Takasugi, T. and O. Izumi. "Factors Affecting the Intergranular Hydrogen Embrittlement of Co_3Ti." Acta Metall. 34, no. 4 (1986): 607-618.

50. Camus, C. G., N. S. Stoloff, and D. J. Duquette. "The Effect of Order on Hydrogen Embrittlement of Ni_3Fe." Acta Metall. 37, no. 5 (1989): 1497-1501.

51. Bond, G. M., I. M. Robertson, and H. K. Birnbaum. "On the Mechanisms of Hydrogen Embrittlement of Ni_3Al Alloys." Acta Metall. 37, no. 5 (1989): 1407-1413.

52. 1986. Dynamic Thermal/Mechanical Metallurgy using the Gleeble 1500. 2nd edition, 28-32. Troy, New York: Duffers Scientific, Incorporated.

53. McKamey, C. G. ORNL, 1990.

54. Santella, M. L., M. C. Maguire, and S. A. David. "Analysis of Heat-Affected Zone Cracking in Ni_3Al Alloy Welds by Computer Modeling of Thermal Stresses." Welding Journal 68, no. 1 (1989): 19s-27s.

55. Kubachewski, O. and C. B. Alcock. 1979. Metallurgical Thermochemistry. Elmsford, New York: Pergamon Press, Inc.

56. Weast, R. C., ed. 1983. Handbook of Chemistry and Physics. 64th ed., p. E-42. Boca Raton, Florida: CRC Press, Inc.

57. Anthony, L. and B. Fultz. "Kinetic Paths of B2 and DO_3 Order Parameters: Experiment." J. Mater. Res. 4, no. 5 (1989): 1140-1142.

58. Warren, B. E. 1969. "X-ray Studies of Order-Disorder." Chapter 12 in X-ray Diffraction. Reading, Mass.: Addison-Wesley.

59. Cottrell, A. H. "Theory of Brittle Fracture in Steel and Similar Metals." Trans. AIME-TMS 212 (1958): 192-203.

60. Schulson, E. M. and D. R. Barker. "A Brittle to Ductile Transition in NiAl of a Critical Crack Size." Scr. Metall. 17 (1983): 519-522.

61. Lancaster, J. F. 1987. "Carbon and Ferritic Alloy Steels." Chapter 7 in Metallurgy of Welding. 4th. ed. London: Allen and Unwin.

62. Sikka, V. K. and J. R. Weir. "Iron Aluminides: Properties and Progress in the Development of a Family of Alloys Based on the Intermetallic Compound Fe_3Al." ORNL, 1990.

63. Preece, C. M. and A. R. C. Westwood. "Temperature-Sensitive Embrittlement of FCC Metals by Liquid Metal Solutions." Trans. ASM 62 (1969): 418-425.

64. Venkataraman, R., M. D. Baldwin, and G. R. Edwards. 1990. "Embrittlement of Steels by Lead." To be Published in Conference Proceedings of Sixth Beer-Sheva International Seminar on MHD Flows and Turbulence.

APPENDIX A

This section presents the necessary tables and thermal cycles generated for the cooling rate test which simulated different GTA weld heat inputs.

Table A-1 Estimated Thermal Conductivity Values for FAS

T (°C)	T (deg. K)	est. β (Ω-cm)	est. Γ (W/cm-K)
23	296	157	0.046
200	473	155	0.075
300	573	158	0.089
400	673	163	0.101
500	773	168	0.113
600	873	162	0.132
700	973	162	0.147
800	1073	162	0.162
900	1173	162	0.177
1000	1273	162	0.193

Table A-2 Heat Capacity Estimates for $Fe_{72}Al_{28}$ (cal/mole-K)

T (deg. K)	T (°C)	C_p (Fe)	C_p (Al)	C_p $Fe_{72}Al_{28}$
298	25	6.00	5.82	5.95
400	127	6.50	6.12	6.39
500	227	7.02	6.42	6.85
600	327	7.58	6.72	7.34
700	427	8.24	7.01	7.90
800	527	9.17	7.31	8.65
900	627	10.48	7.60	9.67
1000	727	13.56	7.00	11.72
1100	827	10.23	7.00	9.33
1200	927	8.16	7.00	7.84
1300	1027	8.31	7.00	7.94

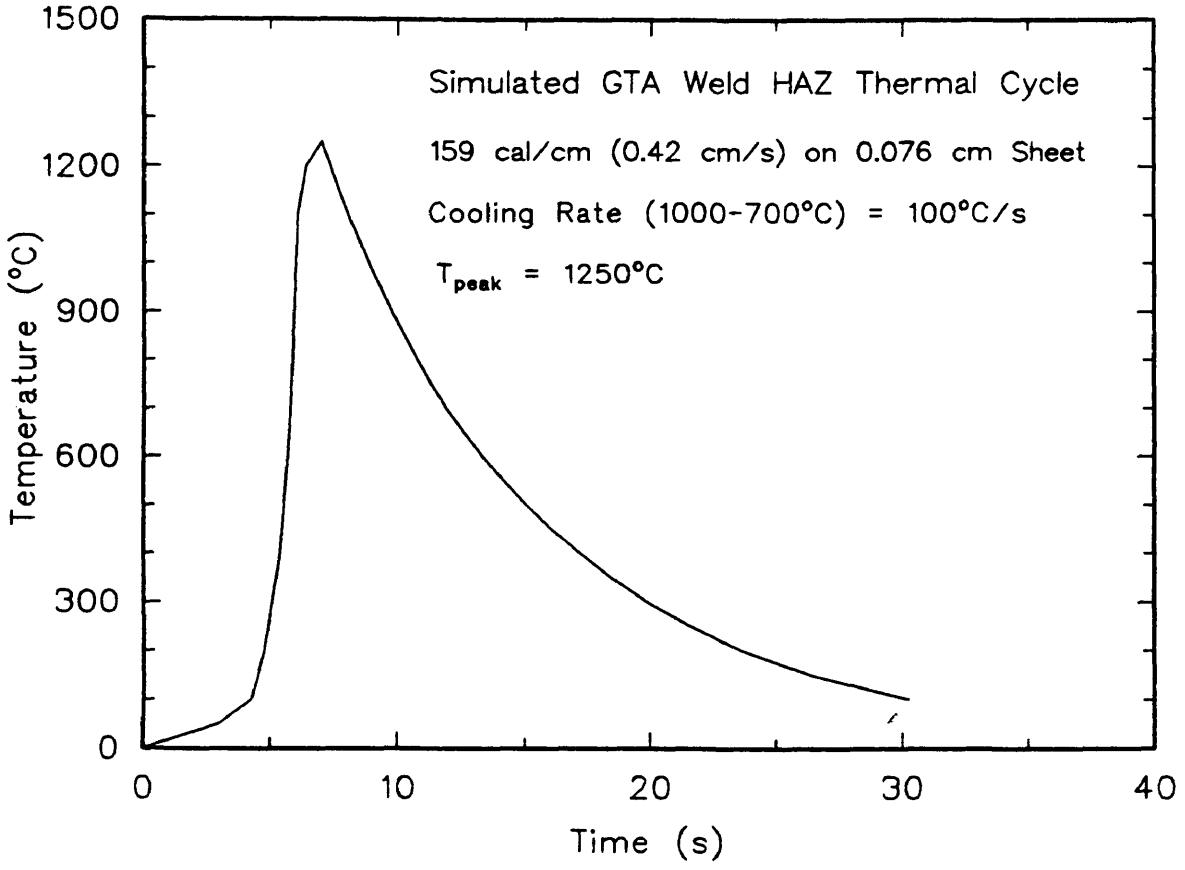

Figure A1 Simulated GTA weld HAZ thermal cycle for 159 cal/cm weld heat input.

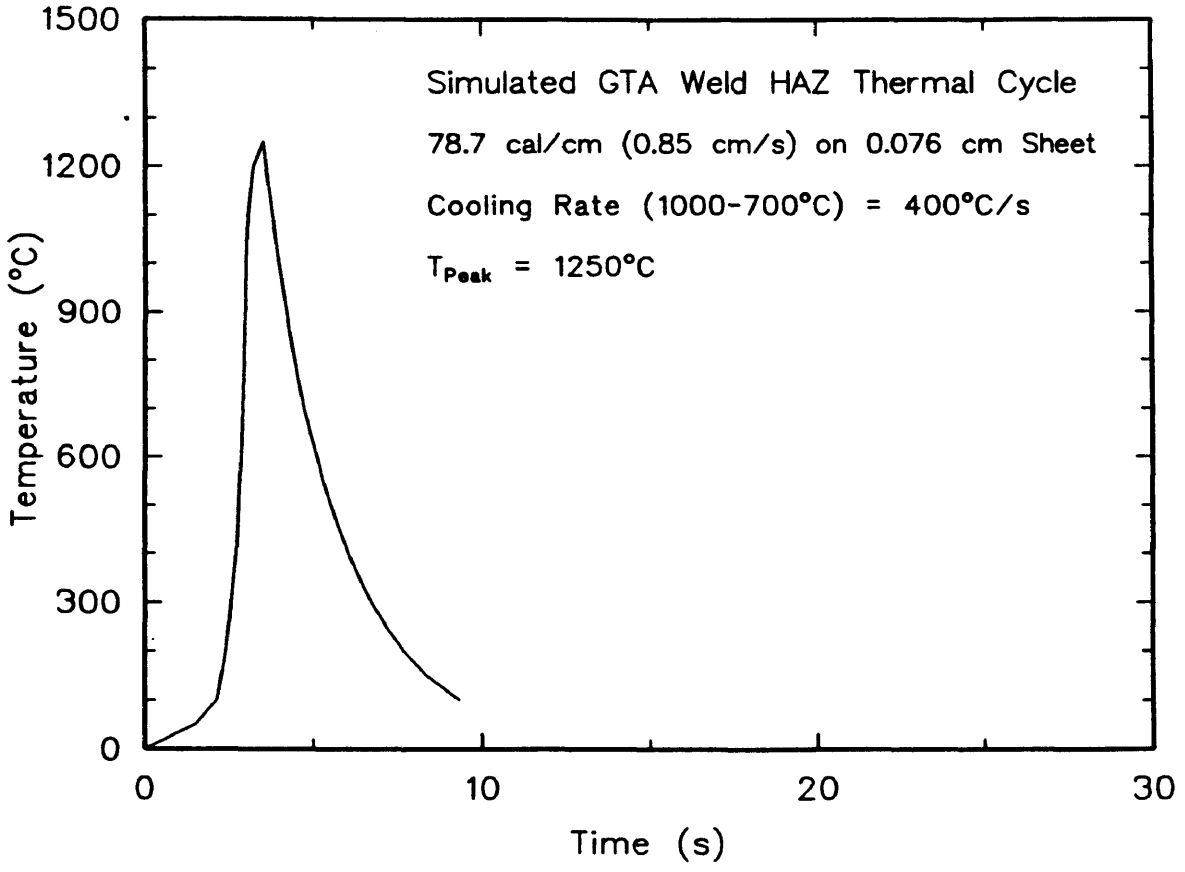

Figure A2 Simulated GTA weld HAZ thermal cycle for 78.7 cal/cm weld heat input.

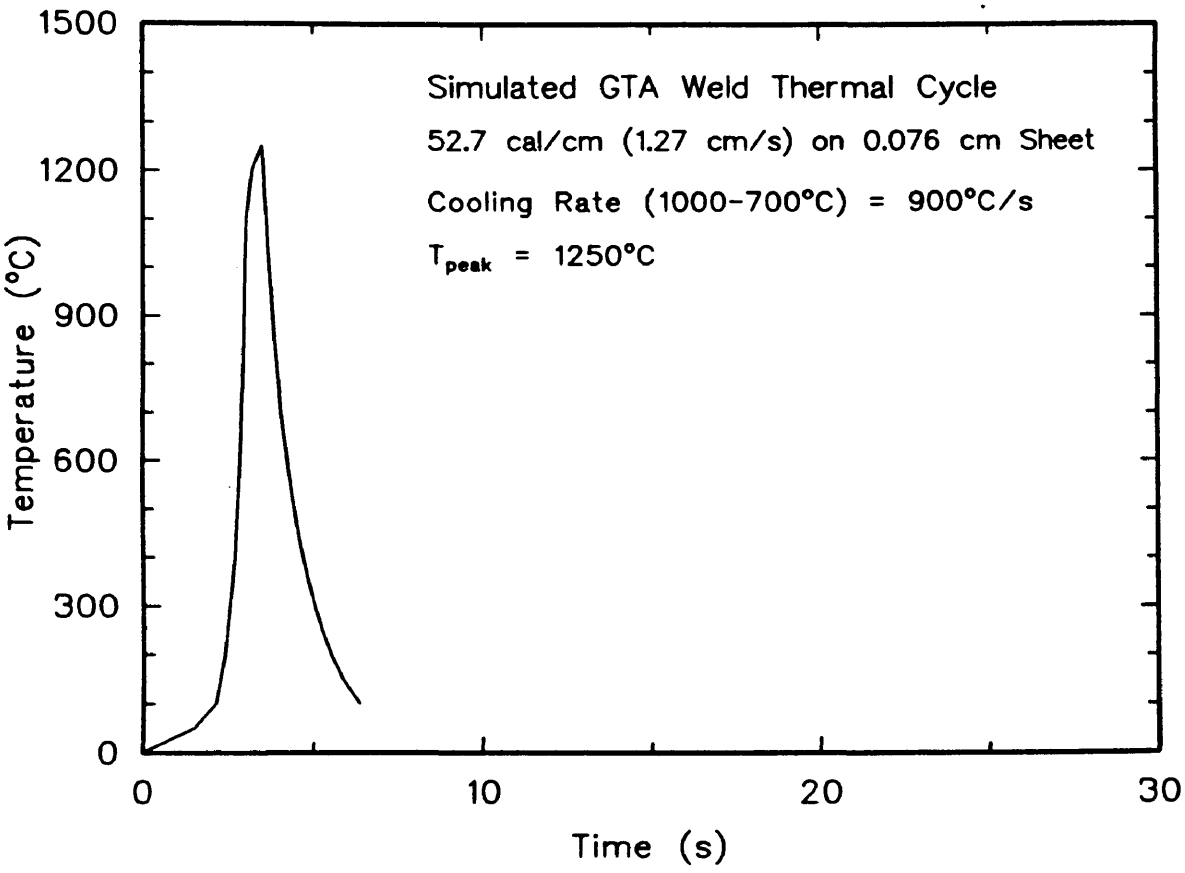

Figure A-3 Simulated GTA weld HAZ thermal cycle for 52.7 cal/cm weld heat input.